METALLOBIOCHEMISTRY OF RNA: MG(II) AND FE(II) IN DIVALENT BINDING SITES

A Dissertation
Presented to
The Academic Faculty

by

C. Denise Okafor

In Partial Fulfillment
of the Requirements for the Degree
Doctor of Philosophy in the
School of Chemistry and Biochemistry

Georgia Institute of Technology
AUGUST 2015

METALLOBIOCHEMISTRY OF RNA: MG(II) AND FE(II) IN DIVALENT BINDING SITES

Approved by:

Dr. Nicholas Hud, Advisor
School of Chemistry
Georgia Institute of Technology

Dr. Loren Williams, Co-Advisor
School of Chemistry
Georgia Institute of Technology

Dr. Wendy L. Kelly
School of Chemistry
Georgia Institute of Technology

Dr. Roger Wartell
School of Biology
Georgia Institute of Technology

Dr. Adegboyega K. Oyelere
School of Chemistry
Georgia Institute of Technology

Date Approved: June 23, 2015

‘..being confident of this, that he who began a good work in you will carry it on to completion...’

ACKNOWLEDGEMENTS

For the work presented in this thesis and my overall graduate school experience, I must acknowledge the contributions of many, beginning with my thesis advisers, Dr. Nicholas Hud and Dr. Loren Williams. I will be forever grateful for the opportunity of joining these research groups. I have gained much in the way of knowledge and skills, receiving support at every step that has positioned me for success in the pursuit of my professional goals.

From Dr. Hud, I have learned to lean more strongly on my own abilities and give myself the freedom to plunge into learning something new if it will push my work along, instead of needlessly waiting for help from someone else. I have also learned how to think about science critically and to navigate the delicate balance, that researchers face so often, between continuing to pursue an elusive experimental result, and deciding when to let it go, albeit reluctantly, to move forward in a different direction.

Dr. Williams deserves great credit for my persistence in graduate school. Thanks to the confidence that he had in me, I have a strong belief in my own ability to venture into new research areas and be successful. I have observed and learned the art of cautiously analyzing research data, and extracting the maximum possible amount of information that is available. These are skills and abilities that I consider to be invaluable.

I am extremely grateful for the support of my committee, Dr Yomi Oyelere, Dr. Wendy Kelly and Dr. Roger Wartell. I have received guidance and advice on experiments both in the lab and during committee meetings that have given me new perspectives on my work, and increased my understanding of different phenomena I have encountered. I

am especially thankful for the encouragement I have received over the years from Dr. Kelly, which has directly impacted not only my graduate school experience, but also my future career prospects.

I acknowledge a few people who have directly or indirectly played an important role in the work presented in this thesis. Dr. Anton Petrov served as an initial mentor to me, guiding me in all of the quantum mechanics work that is presented in this thesis. Dr. Chiaolong Hsiao guided me in a lot of my experimental work, and first showed me how to perform RNA experiments with iron. Jessica Bowman has patiently answered a lot of questions and taught me many things over the years as I have grown each year as an experimentalist. Eric O'Neill has been a well of information, an immense resource for troubleshooting, and supplier of an endless amount of RNA for experiments.

By working on different projects in highly collaborative environments, I have learned the value of actively sharing and benefitting from the collective knowledge and abilities of others in the research community. I could not have made as much progress as I did without the members of the Williams and Hud labs. There is no way to sufficiently acknowledge the contributions of these colleagues and friends, many of whom have also been co-authors in publications.

I am grateful to my Hud labmates, past and present, for help with research and instrumentation, companionship and support. Aaron Engelhart, Irena Mamajanov, Ragan Buckley, Brian Cafferty, Tim Lenz, Isaac Gallego, Ford Lannan, Brandon Laughlin, Chelsea Walker, Caterina Musetti, Christine He, Michael Chen, David Fialho, Gary Newnam, Suneesh Karunakara, Jaheda Khanam, Adriana Lozoya Colinas and Linda Nhon have been a joy to work with.

I am grateful to my Williams labmates for their generosity and friendship. I benefited greatly from their willingness to always look out for one another. Chiaolong Hsiao, Jessica Bowman, Eric O'Neill, Tim Lenz, Brande Jones, Dana Schneider, Paul Fang, Kathryn Lanier, Derrick Watkins, Shreyas Athavale, Caitlin Prickett, Poorna Roy, Burak Gulen, I-Chun Chou, Chad Bernier, Eric Anderson, Lizzette Gomez-Ramos, Nicholas Kovacs are all appreciated.

I have had the tremendous honor of working with many undergraduate students, mentoring them and in turn receiving valuable help with my research. I am grateful to Drew Vander Wood, Lance Jubic, Yinglin Li, Spencer Hoskyns, Amrita Banerjee, Emanuel Voikhansky and Hassan Ali.

Sue Winters ensured that many aspects of my graduate school experience ran smoothly, I am grateful for that. I am also grateful to Dr. Keith Oden, Dr. Christine Conwell, and Gary Longstreet for support, encouragement and camaraderie that I received at different points. I thank Megan Mann for years of graduate school friendship. I am grateful to Dr. Rigoberto Hernandez for teaching me most of what I know about coding and helping me gain a strong computational background.

I will forever be grateful for the support of my husband, Ikenna Okafor, which permeates every aspect of my life. My daughter, Chidera Christine, brings me joy and is a constant reminder to keep my life in perspective. My parents and sisters have been my biggest cheerleaders in this process. There are no words for how much their encouragement has meant to me. My friends from Mount Paran Church have been like family to me in Atlanta. They will always have a special place in my heart. Finally, I

acknowledge that I would **not** have made it this far without my faith. I am grateful to God.

TABLE OF CONTENTS

Page

LIST OF TABLES

Page

LIST OF FIGURES

Page

LIST OF SYMBOLS AND ABBREVIATIONS

ABTS	2,2'-azino-bis(3-ethylbenzothiazoline-6-sulphonic acid)
ADP	Adenosine diphosphate
a-rRNA	Ancestral ribosomal RNA
ATP	Adenosine triphosphate
BIF	Banded iron formations
BSSE	Basis set superposition error
CD	Circular dichroism
CE	Capillary electrophoresis
DAP	2,3-diaminophenazine
DCTA	Diaminocyclohexane tetraacetic acid
DFT	Density functional theory
DMSO	Dimethyl sulfoxide
DNA	Deoxyribonucleic acid
DTPA	Diethylenetriamine-*N,N,N',N',N''*-pentaacetic acid
EDTA	Ethylene-diamine tetraacetic acid

ESI	Electrospray ionization mass spectrometry
ES	Enzyme-substrate complex
$[E_T]$	Total enzyme concentration
$FADH_2$	Flavin adenine dinucleotide
GOE	Great oxidation event
HEPES	(4-(2-hydroxyethyl)-1-piperazineethanesulfonic acid)
HEDTA	N-(2-Hydroxyethyl)ethylenediamine-*N*,*N*',*N*'-triacetic acid
LSU	Large subunit
NADH	Nicotinamide adenine dinucleotide
NADPH	Nicotinamide adenine dinucleotide phosphate
NEDA	Natural energy decomposition analysis
NMR	Nuclear magnetic resonance
OPD	*o*-Phenylenediamine
PAGE	Polyacrylamide gel electrophoresis
PDB	Protein data bank
PTC	Peptidyl transferasecCenter
K_m	Michaelis-Menten constant

K_{cat}	Enzyme turnover number
QM	Quantum mechanics
RMSD	Root mean square deviation
RNA	Ribonucleic acid
rRNA	Ribosomal ribonucleic acid
[S]	Total substrate concentration
SELEX	Systematic evolution of ligands by exponential enrichment
SHAPE	Selective 2’-hydroxyl acylation analyzed by primer extension
STMV	Satellite tobacco mosaic virus
TMB	3,3',5,5'-Tetramethylbenzidine
TRIS	Tris(hydroxymethyl)aminomethane
tRNA	Transfer ribonucleic acid
tRNA-Phe	Phenyalanine-specific transfer ribonucleic acid
UV-Vis	Ultraviolet-visible spectroscopy

SUMMARY

Cations are essential for ribonucleic acids (RNA), as they neutralize the negatively charged phosphate backbone. Divalent metals play important roles in the folding and function of RNA. Magnesium ion (Mg^{2+}), in particular, has a special relationship with RNA, involved in tertiary interactions of many large RNAs, and necessary for ribozyme activity in several catalytic RNAs. Mg^{2+} chelates RNA ligands, mainly phosphate oxygen atoms, to form coordination complexes that stabilize tertiary structure in RNA.

My research has focused on studying RNA binding to divalent metal ions, Fe^{2+} and Mg^{2+}, characterizing the structural and functional properties of RNA interactions with these metals. This work has been motivated, in part, by the discovery that iron (Fe^{2+}) can serve as a substitute for Mg^{2+} for folding RNA and for ribozyme catalysis. Fe^{2+} was abundant on early earth, so it is plausible that RNA folding and function was mediated by Fe^{2+} instead of, or in combination with, Mg^{2+} in the anoxic atmosphere of early earth. We have investigated oxidoreductase catalytic activity observed in RNA when in combination with Fe^{2+}. This activity, only observed in the presence of Fe^{2+} and absence of Mg^{2+}appears to be a resurrection of ancient RNA capabilities that were extinguished upon the depletion of Fe^{2+} from the environment during the rise of oxygen after the great oxidation event.

Previous observations that Mg^{2+} and Fe^{2+} induce similar structures in RNA led to the hypothesis that the two ions could also interact at the same sites in RNA. We have set out to identify these binding sites in RNAs that have divalent metal-dependent folding,

using in-line cleavage of the phosphodiester backbone, as facilitated by the divalent metal ions. Metal ion-based cleavage is a method that has previously been applied to probe ion binding sites in RNA.

Quantum mechanics provides powerful computational tools to probe the energetics of cation association with nucleic acids. We use these tools to investigate Mg^{2+} chelation to phosphate oxygens. We explore conformational and energetic fingerprints of Mg^{2+} complexes, using energy decompositions to probe the specific forces (i.e. electrostatic vs. non-electrostatic forces) that contribute to the overall complex energies. For example, we show that the ability of Mg^{2+} to polarize coordinated ligands is a strong stabilizing factor in chelation complexes.

We have also investigated the influence of Mg^{2+} on RNA secondary structure and tertiary structure. RNA folding is hierarchical, collapsing from non-native structures with local single- and double-stranded regions into compact native structures. The initial conformations of RNA present often determine the folding pathway, and intermediates observed. We investigate the structure of RNA in low-salt conditions, and observe Mg^{2+} binding, accompanied by conformational changes at low (< 1 mM) concentrations. Using both A-form helical RNA duplexes and larger RNAs in low-salt, non-native states, we demonstrate subtle but clear conformational differences in the RNA depending on the identity and concentration of cations present in solution. These conformational differences appear to arise from variations in helical structures adopted in the presence of different cations, which has been previously observed for DNA duplexes. We show that these different starting conformations clearly affect the folding pathway. Therefore in addition to the important considerations for RNA-Mg^{2+} interactions in folded RNAs and

in ribozymes, we show that they should not be ignored in duplex or unfolded RNAs, as they affect RNA helical structure.

CHAPTER 1

INTRODUCTION

Ribonucleic acid, or RNA, is one of the three macromolecules, along with DNA and protein that are essential for life. Like DNA, RNA is a polymer of nucleotides, linked by phosphate groups which are negatively charged at physiological pH. RNA molecules typically form complicated tertiary structures, necessary for function. Positively charged species, such as inorganic cations and polyamines, are necessary for RNA compaction and folding. Cations screen the repulsions between phosphate groups on the RNA backbone, allowing them to be brought into close proximity during RNA folding. The interactions of these cations with RNA are subtle and polymorphic, and depend on the sequence and structure of the RNA, on the type of cation, and on other cations in the system (1).

RNA and cations

Cations interact with RNA in different environments along the RNA. These environments have often been divided into two: those of 'diffuse ion' interaction and those that exhibit 'chelated ion' interaction (2). Diffuse cations possess behavior that is determined by RNA electrostatic field. They largely remain hydrated, therefore having little to no direct nucleic acid contacts (Figure 1, left). This category of cations has been referred to as an 'ion atmosphere', with the concentration of cations in regions surrounding the RNA being proportional to the electrostatic potential in that region (3). Monovalent cations (such as Na^+ and K^+) generally fall into the category of diffuse binding.

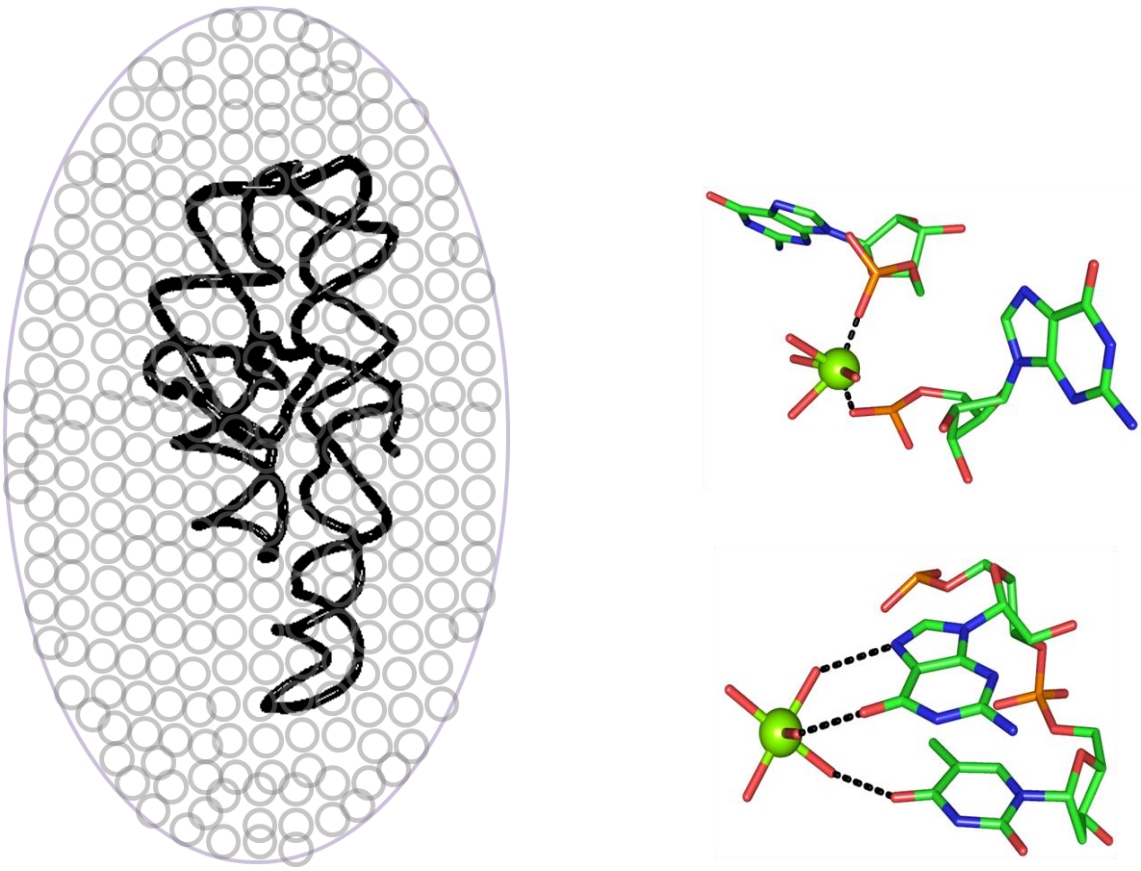

Figure 1. Potential ion environments in an RNA. Left, RNA (black) is surrounded by cations interacting loosely in an ion atmosphere. Right, cations interact with RNA specifically, either remaining undergoing partial dehydration (right, top) while chelated by phosphates (1st coordination), or remaining hydrated while interacting with RNA (right, bottom). Cations are shown as green spheres bound with waters of hydration shown in red in a stick representation. Dashed black lines represent coordination bonds between cation and RNA ligands.

Multivalent and divalent cations can both be present in the ion atmosphere. In contrast to cations in this atmosphere, a chelated ion binds directly to the nucleic acids in specific locations. This interaction requires a dehydration of the ion, or loss of one or more hydrating water molecules, for it to be chelated by RNA groups (Figure 1, right, top). This is referred to as first-shell coordination i.e. RNA ligands are in the first coordination shell of the cation. Chelated ions can also bind to RNA as fully hydrated ions (Figure 1, right, bottom). Chelated ions are less mobile than diffuse ions, and play

important roles in formation of RNA native tertiary structures. However, the electrostatic influence of diffuse ions largely stabilize the overall RNA structure (2).

This two-state categorization of RNA-cation interactions, while convenient for many applications, poses limitations on a deeper understanding of the subtleties of RNA-cation binding. Indeed, many cation interactions fall somewhere between the two classes. A new formalism partitions RNA-cation interactions into four classes: *free, condensed, glassy* and *chelated* (1).This classification illustrates a continuum of RNA cation interactions, ranging from diffuse interactions (free) to highly coordinated ions (chelated). *Condensed* ions are well-hydrated, possessing near bulk-like properties. *Glassy* ions possess first-shell interactions with RNA, causing them to be more restricted than condensed cations. *Chelated* ions are highly coordinated to RNA ligands, so they are more dehydrated than other cations. These cations largely determine the conformation of RNA. The largest class of cations is *free,* while the smallest class is *chelated*. The chelated ions possess the largest number of first-shell interactions, making them most important for stabilizing specific structural interactions. Condensed, glassy and chelated cation interactions are illustrated in Figure 2.

RNA and Mg^{2+}

Magnesium ions interact with RNA in both site specific, coordinated interactions and in diffuse binding. Early studies of RNA-cation interactions revealed that Mg^{2+} plays a special role in tRNA folding, (4-6) and that it can also participate directly in ribozyme activity by stabilizing transition states (7,8). These observations have motivated decades of work on ion-RNA interactions, with a special emphasis on Mg^{2+}.

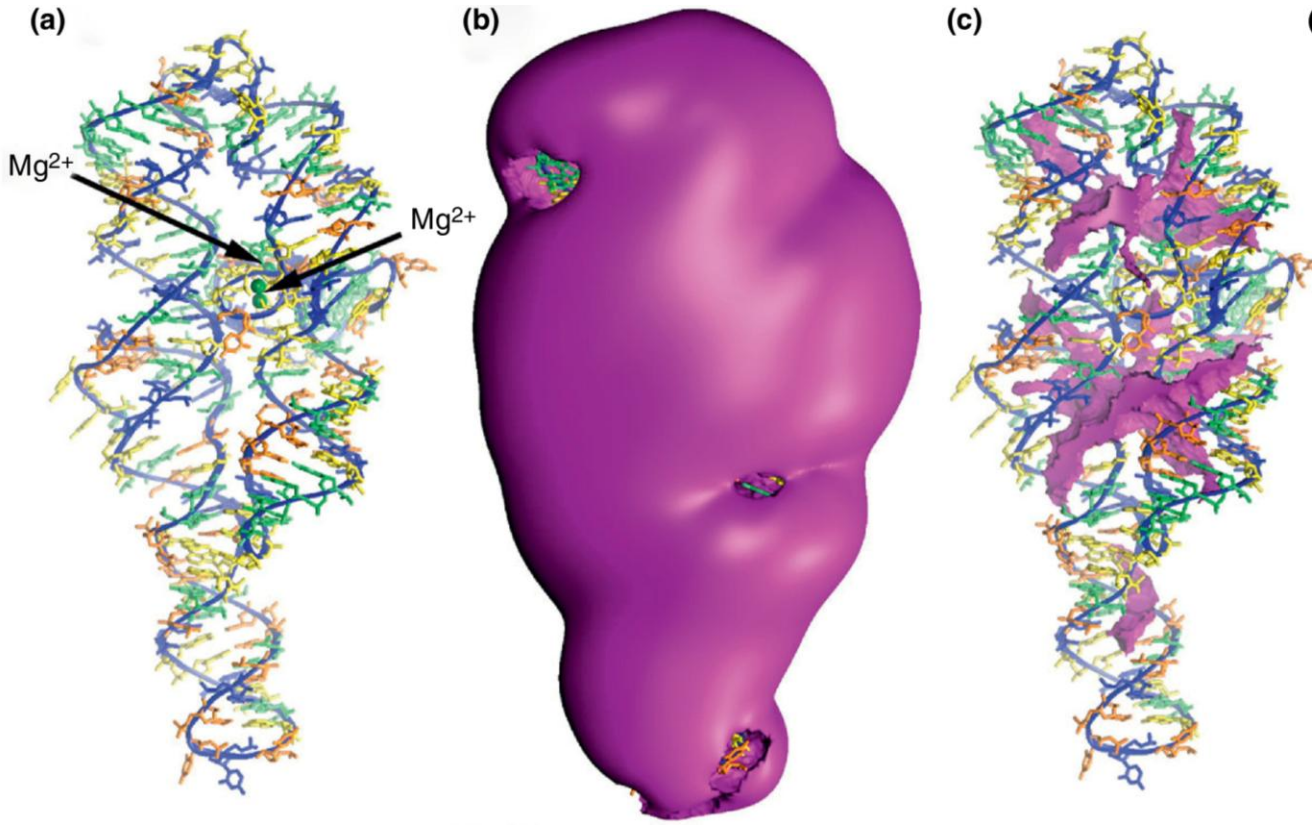

Figure 2. Condensed, glassy, and coordinated cations in the P4-P6 domain of the Tetrahymena Group 1 intron RNA [PDB 1HR2]. (A) Three condensed Mg^{2+} ions are indicated by green spheres. (B) The envelope containing condensed cations surrounding the P4–P6 RNA. (C) Regions of glassy cation localization within the grooves. Reprinted from (1) with permission.

Unique properties of Mg^{2+}

Since the beginning of life, Mg^{2+} has been closely associated with phosphates and phosphate esters (9,10). Mg^{2+} shares a special geometric, electrostatic, thermodynamic relationship with phosphates (10). Mg^{2+} ion, with a small radius (0.65 Å), possesses a high charge density and an octahedral coordination geometry (coordination number is 6). The preferred coordination ligands for Mg^{2+} are charged or neutral oxygens (Figure 3), and the hydration enthalpy for Mg^{2+} is high (-458 kcal/mol) (11-14). It is the dominant divalent cation in biology and is widely available in the biosphere, constituting 2% of the

earth's crust. In addition to being highly soluble near neutral pH, Mg^{2+} is inert to O_2, not changing its oxidation state readily. Therefore, Mg^{2+} is a unique partner for RNA.

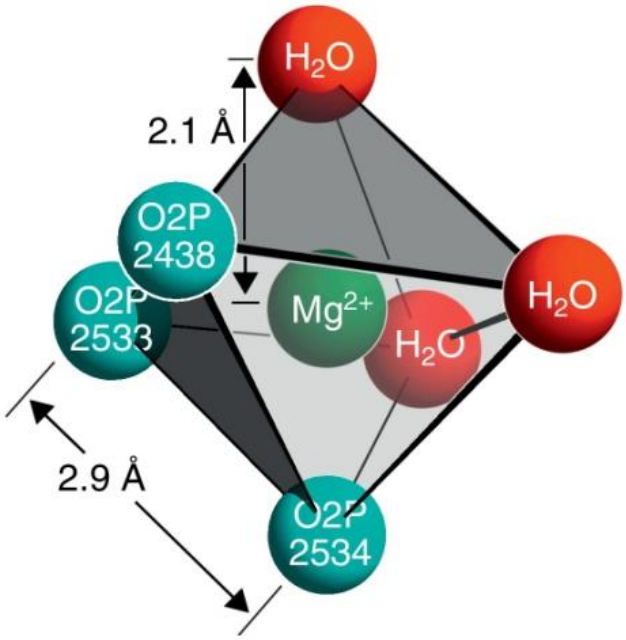

Figure 3. A Mg^{2+} ion chelated by RNA. This Mg^{2+} ion (green sphere) is octahedral, with three first shell phosphate oxygens of the rRNA (cyan) and three first shell water oxygens (red). Reprinted from (1) with permission.

Mg^{2+} can increase local rigidity of RNA by tightly packing functional groups in its first coordination shell. One of the hallmarks of Mg^{2+} complexes is ligand-ligand crowding, While Mg^{2+} prefers phosphate oxyanions, non-oxygen ligands are also observed to be coordinated to Mg^{2+} (15). Phosphate groups are more polarizable than water molecules, so when RNA phosphate oxygens enter the first shell of a Mg^{2+}, electron density is pulled into the Mg^{2+} and the phosphorus atom is activated to nucleophilic attack. Large globular RNAs are observed by X-ray diffraction to be associated with magnesium ions. These associated ions range throughout the four classes of RNA-cation interactions. For example, of 118 Mg^{2+} ions associated with the 23S rRNA in the large ribosomal subunit (LSU) of *Haloarcula marismortui* (16,17), 98 of

these have phosphate oxyanions (OP) in their first coordination shells. First coordination shell interactions are characterized by a Mg^{2+}-OP distance < 2.4 Å. Similarly, 26 out of 71 total magnesium ions associated with the P4-P6 domain of the *Tetrahymena* group 1 intron (15,18) contain first-shell interactions with phosphate oxyanions.

Magnesium binding motifs in RNA

Magnesium forms several, distinct motifs with RNA, arising from its coordination interactions with phosphate oxyanions. For example, Mg^{2+} forms mononuclear complexes with ADP and ATP, binding by bidentate and tridentate interactions (10). Figure 4 illustrates a mononuclear ADP-Mg^{2+} complex. Bidentate chelation complexes are six-membered rings with the atoms Mg^{2+}-O^1P-P-O-P-O^2P-Mg^{2+} (where O^1P and O^2P are oxygen atoms from adjacent phosphate groups, e.g. α and β, or β and γ, P represents phosphorus atoms and O represents the bridging oxygen atom) (10). Tridentate chelation complexes are bicyclic, with two six-membered rings. Mg^{2+} interactions with the phosphate oxygens of ATP/ADP are highly predictive of Mg-RNA coordination interactions. Similarly, distinct motifs are observed repeatedly in RNAs, suggesting that these complexes are important in RNA tertiary structure. These motifs are not supported in common elements of RNA secondary structure (e.g. A-form helices and loops), because the OP atoms are too far apart to enable multidentate chelation.

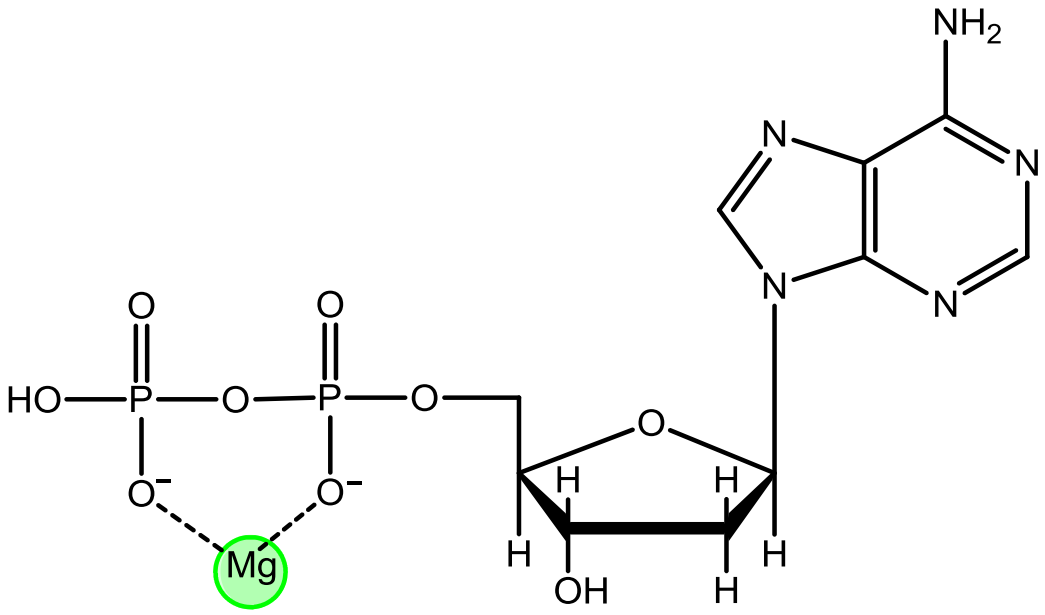

Figure 4. Mononuclear ADP-Mg(II) complex. Six-membered ring is formed by bidentate chelation of Mg(II). Dashed lines represent coordination bonds between magnesium and phosphate oxygen atoms (OP).

Bidentate clamp

A mononuclear RNA-Mg^{2+} complex is formed when OP atoms of adjacent residues chelate a common Mg^{2+}. This chelation forms a ten-membered ring containing the atoms Mg^{2+}-O^1P-P-O5'-C5'-C4'-C3'-O3'-P-O^2P-Mg^{2+} (Figure 5). This bidentate clamp is observed 25 times in the *H. marisortui* LSU (16), twice in the P4–P6 domain of the *Tetrahymena* group 1 intron (15,18), once in a self-splicing group II intron from *Oceanobacillus iheyensis* (PDB entry 3IGI) (19), and once in the L1 ligase (PDB entry 2OIU) (20).

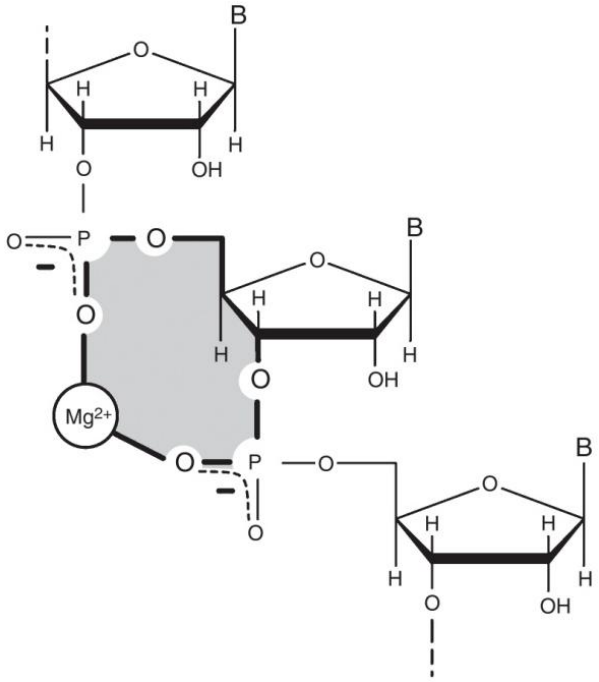

Figure 5. A schematic diagram of a bidentate RNA clamp of magnesium, formed when adjacent phosphate groups enter the first coordination shell of a common magnesium ion. A 10-membered ring (shaded) characterizes the Mg^{2+} clamp. Reprinted from (1) with permission.

Magnesium microcluster

A framework of dinuclear Mg^{2+}-RNA complexes was observed as flanking the peptidyl transferase center (PTC) in LSU ribosomal structures. The dinuclear Mg^{2+} complex is made up of two Mg^{2+} ions that are chelated by a common bridging phosphate in the form: $Mg^{2+}{}_a$-(O^1P-P-O^2P)–$Mg^{2+}{}_b$. The bridging phosphate is part of a 10-membered chelation ring in the form: $Mg^{2+}{}_a$ –(OP-P-O5'-C5'-C4'-C3'-O3'-P-OP)–$Mg^{2+}{}_b$. The two phosphate groups in this motif are contributed by adjacent residues along the RNA backbone (Figure 6).

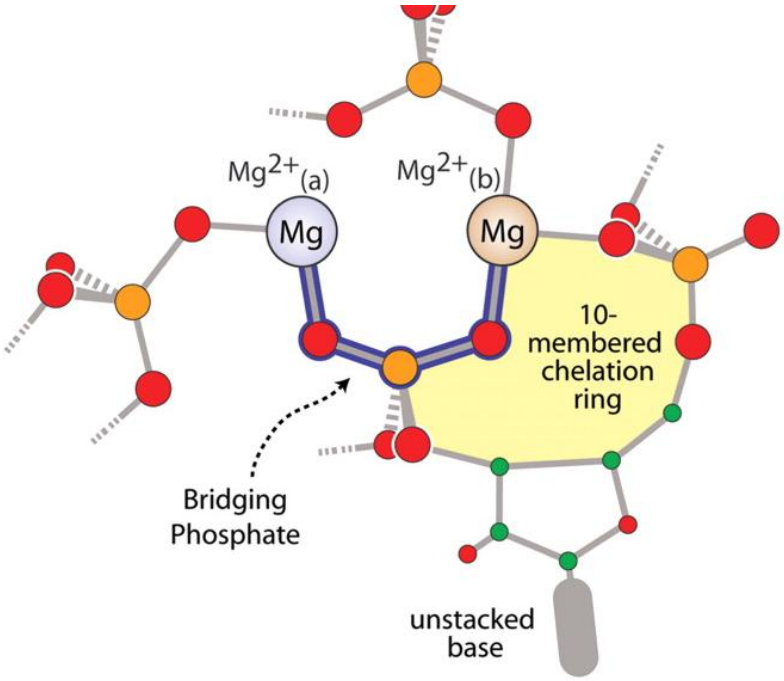

Figure 6. The Mg^{2+} microcluster motif. A schematic diagram illustrating the Mg^{2+}_a–(O^1P-P-O^2P)–Mg^{2+}_b bridge (outlined in blue), the 10-membered chelation ring (yellow), an unstacked base and the additional RNA phosphate groups that enter the Mg^{2+} first shell at variable positions. Reprinted from (21) with permission.

The Mg^{2+} ions in the microcluster are highly dehydrated, as they maintain their octahedral coordination by chelating RNA groups. Coordination in the microcluster results in Mg^{2+}-Mg^{2+} distances of 5.3-5.6 Å. Features in the microcluster are conserved, such as the conformation of the RNA and relative positions of the Mg^{2+} ions in the microcluster, which are constrained by Mg^{2+}_a–(O^1P-P-O^2P)–Mg^{2+}_b bridges. Indeed, a superimposition of the four microclusters present in the LSU gives a root mean square deviation (RMSD) of 0.59 Å. These microclusters provide the framework and supporting structure for the RNA that forms the PTC.

While the basic motif of the microclusters are the same, each microcluster has unique features, as they pose constraints on the surrounding RNA, allowing RNA phosphate groups that are not part of the 10-membered to enter the Mg^{2+} coordination

spheres at different positions. These residues become part of the microcluster. In addition to the 23S rRNA, a microcluster is observed in the 16S (22), and in the P4-P6 domain of the *Tetrahymena* group I intron ribozyme.

Comparison of Mg^{2+} to other biological cations

Compared to group I cations, Ca^{2+}, or polyamines, Mg^{2+} has a greater affinity for phosphate oxygens, binding to them with well-defined geometry and bringing them into its first shell into direct contact with each other. These first shell waters are polarized by Mg^{2+}, activating them for enzymatic mechanisms and molecular recognition (1). Quantum mechanics (QM) calculations were used to investigate bidentate magnesium clamps, specifically their energetic and conformational fingerprints(23). The results showed why magnesium ions can induce specific conformational states of RNA that are inaccessible with other biological cations.

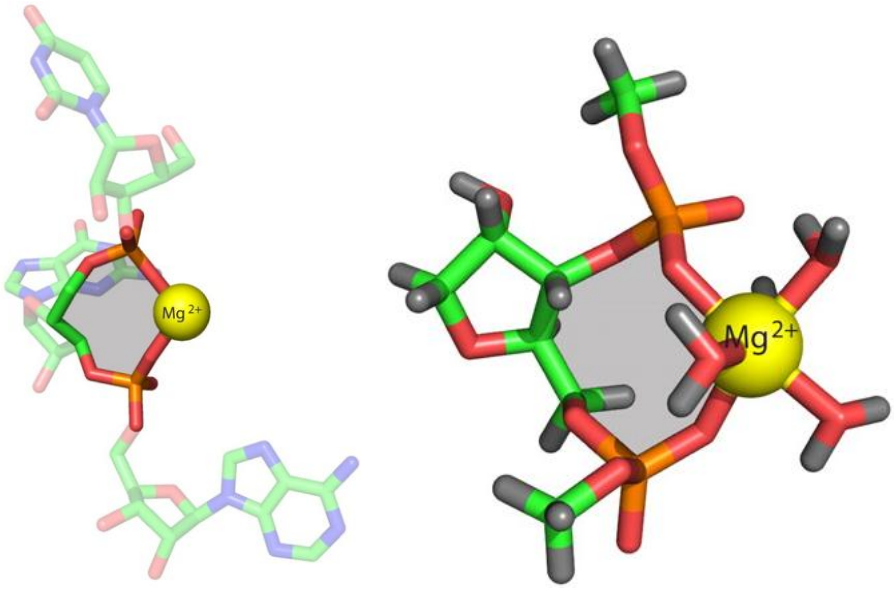

Figure 7. The RNA^{2-}–Mg^{2+}•$(H_2O)_4$ complex (right) extracted from the bidentate RNA clamp (left) used for QM calculations. The base is replaced by a hydrogen atom and the chain is terminated with methyl groups. Ten-membered rings are shaded grey. Reprinted from (23) with permission.

A prototypical bidentate RNA clamp of magnesium (Figure 5) extracted from the LSU of *H. marismortui* (PDB entry 1JJ2) was used to build a template clamp for QM calculations. Phosphates attached to the O3' and O5' atoms of a ribose were capped with methyl groups in lieu of the remainder of the RNA polymer (Figure 7). Both RNA and DNA clamps were constructed with magnesium, calcium and sodium, in an aqueous environment (with 2'OH group replaced by hydrogen in DNA clamps). Clamp geometries were cation dependent, taking into account differences in ionic radii.

Using the reaction:

$RNA^{2-} + Mg^{2+}(H_2O)_6 \rightarrow RNA^{2-}\text{-}Mg^{2+}(H_2O)_4$ complex + $2H_2O$,

geometries of complexes and all monomers were obtained and interaction energies calculated. The absolute value of the interaction energies for RNA with cations decreases in the series Mg^{2+}(-31.9 kcal/mol) > Ca^{2+}(-21.5 kcal/mol) >Na^{+}(-4.1 kcal/mol). Bidentate DNA clamps with magnesium were observed to be 10 kcal/mol less stable than RNA clamps. The additional stability in RNA clamps arose from a favorable through-space effect of the polar ribose 2'-OH group. The oxyanions contained within the magnesium first shell are closer together than those associated with the other cations. Average Mg-OP and Mg-O(w) coordination bond distances were 2.0 Å and 2.16 Å respectively, compared with 2.31 Å and 2.43 Å for Ca^{2+} and 2.44 Å and 2.59 Å for Na^{+}. These results were consistent with the smaller Mg^{2+} ionic radius (0.65 Å) compared to Ca^{2+} and Na^{+} (0.99 Å and 0.95 Å respectively).

RNA ring opening observed in the Na^{+} clamp indicated that favorable interactions of the oxyanions with the cations were not sufficient to overcome the repulsive interactions, a requirement for clamp formation. Non-electrostatic effects such as charge

transfer, polarization and exchange also played a significant role in stability of Mg^{2+} clamps. These non-electrostatic effects however are less pronounced for calcium due to its larger size, and for sodium due to its smaller charge. These features combined illustrate the unique features that enable Mg^{2+} to play a special role in RNA folding and function.

RNA world hypothesis

According to the central dogma of biology, hereditary information proceeds from DNA to protein through an RNA intermediate. A long-standing question has been: how did the complex machinery responsible for this information transfer arise? RNA is a molecule that can catalyze chemical reactions, similar to proteins, as well as store genetic information like DNA does (24,25). The RNA world hypothesis proposes that in primitive cells, RNA performed functions of both catalysis and information storage {Cech, 2012 #4987}. Later on in evolution, RNA was replaced by DNA and proteins as the genetic material and catalysts, respectively. While there are different theories on the pre-RNA world and what molecules and reactions might have facilitated the prebiotic synthesis of RNA, a defining feature of the RNA world hypothesis is that RNA and RNA enzymes (ribozymes) predate DNA and protein enzymes.

RNA and iron

Fe^{2+} on early earth

Life began on earth around 4 billion years ago (26,27). For about 1 to 1.5 billion years, life evolved on an anoxic earth that had abundant soluble Fe^{2+}. Upon the rise of photosynthetic bacteria, and the great oxidation event (GOE), soluble iron became

oxidized and was depleted from the biosphere, and was deposited into banded iron formations (BIF) (28). BIF iron is seen by isotopic variations to have been a participant in ancient biological processes (29). An RNA world would have flourished on this anoxic, Fe^{2+}-rich earth.

RNA-Fe^{2+} hypothesis

It is hypothesized (30) that RNA could have used Fe^{2+} as a biological cofactor while it was benign, before the rise of molecular oxygen in the atmosphere. Oxidized Fe^{2+} (Fe^{3+}) is damaging to RNA via the Fenton reaction. The conditions of early earth make it plausible that Fe^{2+}, either instead of or in combination with Mg^{2+}, was a possible partner of RNA in the biology of the pre-photosynthesis anoxic earth. Fe^{2+} would have been replaced by Mg^{2+} during the GOE, when it became damaging to RNA. The catalytic abilities of RNA could have been greater on the early earth than after the GOE. Understanding the influence of Fe^{2+} on RNA structure and function could provide important links between the geological record and the RNA world.

Fe^{2+} and Mg^{2+}

Fe^{2+} has an ionic radius of 0.72 Å, very close to that of Mg^{2+}. It also prefers octahedral coordination geometry, similar to Mg^{2+}. Fe^{2+} is widely used as a probe of nucleic acid and protein structure (31), via the Fenton reaction. In the Fenton reaction, Fe^{2+} is oxidized in the presence of ethylenediamine tetraacetic acid (EDTA), generating reactive hydroxyl radicals. •HO radicals attack the DNA/RNA, resulting in cleavage. Ascorbic acid is included in the reaction to reduce Fe^{3+} to regenerate Fe^{2+}. While this method has been applied widely to DNA structure probing, it has only been rarely used for RNA studies. Mg^{2+}, on the other hand, is redox inactive and unable to cleave RNA. In

the absence of oxygen, where the oxidation of Fe^{2+} to Fe^{3+} is inhibited, Mg^{2+} and Fe^{2+} could display similar properties with RNA.

Fe^{2+} as a substitute for Mg^{2+}

Computation and experiments were used to address the question of whether Fe^{2+} is able to substitute for Mg^{2+} in facilitating RNA folding and catalytic activity (30). This was done to test the hypothesis that Fe^{2+} could have been an RNA cofactor on early earth, being replaced by Mg^{2+} during the GOE.

Fe^{2+} facilitates RNA folding

Computational and experimental investigations were performed to study RNA folding with Fe^{2+} and compare it to that of Mg^{2+}.

Computational studies

QM calculations were employed to investigate RNA conformation and coordination geometry when Mg^{2+} is replaced by Fe^{2+} in a first-shell RNA metal complex. The RNA-Mg^{2+} bidentate clamp (Figure 5) was used for this study. Initial coordinates for the clamp were taken from the L1 ribozyme ligase (PDB 2OIU). Density functional theory (DFT) showed that upon replacement of the Mg^{2+} with Fe^{2+} in the clamp, conformations of the RNA-Fe^{2+} clamp and the RNA-Mg^{2+} clamp were nearly identical (Figure 8). The metal-oxygen distances and angles of both clamps were observed to be similar, and the coordination geometry is conserved between both clamps. Calculated interaction energies reveal a more favorable interaction for Fe^{2+} than for Mg^{2+} (1.3 kcal/mol). The extent of charge transfer from phosphate to metal was higher from Fe^{2+}, implying that Fe^{2+} is better than Mg^{2+} at activating the phosphorous atom in RNA

for nucleophilic attack. This increased activation might result from the accessibility of the d-orbitals of Fe^{2+}.

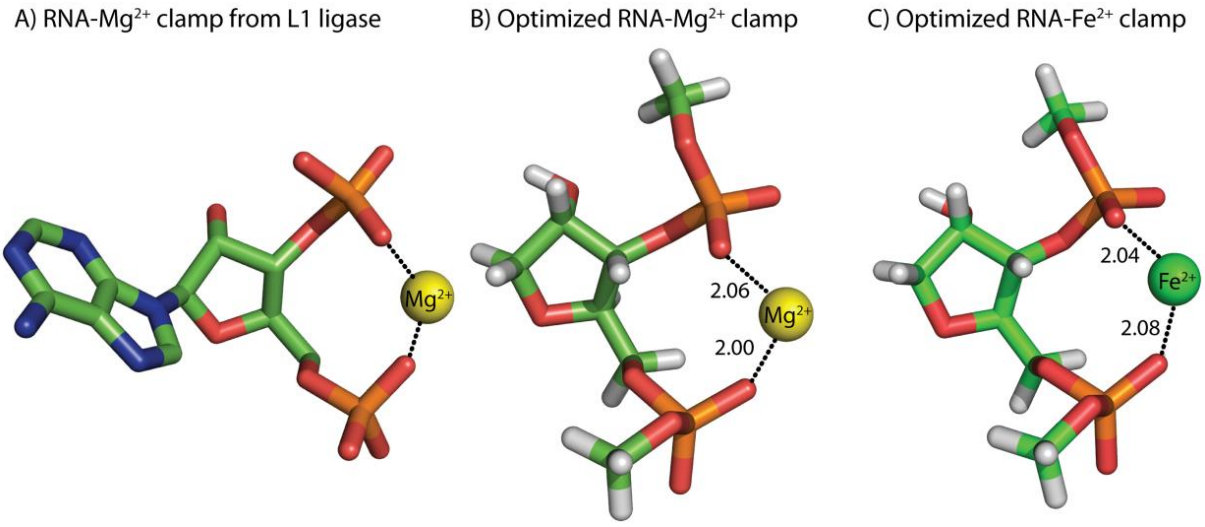

Figure 8. A) RNA-Mg^{2+} clamp from the L1 ribozyme ligase. B) RNA-Mg^{2+} clamp optimized by high level QM calculations. C) An optimized RNA-Fe^{2+} clamp. Both Mg^{2+} (yellow sphere) and Fe^{2+} (green sphere) are hexacoordinate. Water molecules are omitted from the images. Reprinted from (30) with permission.

Experimental studies

RNA footprinting in the presence of Mg^{2+} or Fe^{2+} was performed using the powerful technique, SHAPE; Selective 2'-hydroxyl acylation analyzed by primer extension. The method exploits the reactivity of the 2'-hydroxyl groups of RNA to electrophiles to form 2'-O ribose adduct. Reactivity of the 2'-OH groups vary with RNA conformational flexibility at each position, so that single stranded nucleotides are more reactive than double stranded nucleotides. Reverse transcription with fluorescently-labeled primers gives fragmented products that are truncated at locations which indicate the presence of 2'-O-ribose adducts. Resolution and visualization of the fragments using capillary electrophoresis (CE) allows the secondary structure of the RNA to be assayed.

The secondary structure of the *T. thermophila* Group I intron P4–P6 domain was assayed by SHAPE. In the presence of Na^+ only with no divalent metals, a reaction pattern consistent with the known secondary structure was observed (15). When Mg^{2+} was added, SHAPE reactivity changed to reflect specific Mg^{2+} binding, diffuse interactions, and Mg^{2+}-induced tertiary structure in P4-P6. The obtained pattern was consistent with previous SHAPE data for the same RNA (32). When Mg^{2+} was replaced by Fe^{2+} under anaerobic conditions, the SHAPE reactivity profile obtained was nearly identical to the Mg^{2+} profile nearly identical SHAPE reactivity profile was obtained(30). This result indicated that all Mg^{2+}-dependent interactions in P4-P6, including the tertiary interactions, were conserved and recapitulated by Fe^{2+}.

Fe^{2+} facilitates ribozyme catalysis

RNA function in the presence of Fe^{2+} was assayed by testing the catalytic activity of two ribozymes with Mg^{2+} or with Fe^{2+} in the absence of O_2. The L1 ribozyme ligase is a Mg^{2+}-dependent ribozyme (20) which catalyzes the formation of a phosphodiester linkage. The hammerhead ribozyme cleaves the RNA backbone via nucleophilic attack by a 2'-hydroxyl group on the 3'-phosphorous atom (33). At equimolar metal concentrations, the initial rate of ligation for L1 ligase was enhanced by 25-fold in the presence of Fe^{2+} (3.5×10^{-5} min^{-1}) compared to Mg^{2+} (1.4×10^{-6} min^{-1}). Hammerhead ribozyme cleavage was enhanced by 3-fold in the presence of Fe^{2+} (0.035 min^{-1}) over Mg^{2+} (0.011 min^{-1}) (30). These results suggest that Fe^{2+} is a superior substitute for Mg^{2+} in these catalytic roles.

Overview of Thesis

In this thesis, I describe a series of projects designed to increase our general knowledge and understanding of RNA and its interactions with metal ions. Cations affect the structural, functional and conformational properties of RNA. The special role that Mg^{2+} plays in RNA folding and function can be recapitulated by Fe^{2+}. In Chapters 2 and 3, I present our work showing that the substitution of Fe^{2+} for Mg^{2+} confers previously uncharacterized catalytic activity on RNAs. The nature of this activity is investigated. I discuss the implications of our observations for understanding possible functional roles for RNA on early earth. In Chapter 4, I explore the effect of ion-binding on the helical conformations of A-form RNA. I use Mg^{2+} as a model divalent cation and sodium as a model monovalent cation. This work reveals that different cations give distinct conformations when associated with A-form RNA. I also investigate the implication of these findings on RNA folding pathways and formation of native structure in larger RNAs. In Chapter 5, I demonstrate the utility of computational methods for increasing our understanding of Mg^{2+} chelation by RNA. QM provides insight into the energetics of formation of Mg^{2+}-coordination complexes in a model nucleic acid (ADP), and in a well-characterized, magnesium microcluster complex (Figure 6). QM is also applied to uncover an important role for Mg^{2+} in the interaction of ribosomal RNA and proteins. Finally, in Chapter 6, I use metal-ion cleavage as a structural probe of RNA, to investigate whether Mg^{2+} and Fe^{2+} interact at similar sites in RNA.

CHAPTER 2

ELECTON TRANSFER CATALYSIS BY RNA AND FE^{2+}

Introduction

Some of the data in this chapter is adapted from previously published work: Hsiao, C., Chou, I.-C., Okafor, C.D., Bowman, J.C., O'Neill, E.B., Athavale, S.S., Petrov, A.S., Hud, N.V., Wartell, R.M., Harvey, S.C. *et al.* (2013) Iron(II) plus RNA can catalyze electron transfer. *Nature Chemistry*, 5, 525-528. It is reproduced with permission. I contributed to this work by assisting with experimental design as well as performing electron transfer experiments including control experiments, and running polyacrylamide gels.

Electron transfer catalysis in protein and RNA enzymes

Electron transfer reactions are some of the most fundamental reactions in biological systems. Oxidation and reduction are catalyzed by enzymes (oxidoreductases) that often work in conjunction with organic cofactors such as nicotinamide adenine dinucleotide/nicotinamide adenine dinucleotide phosphate (NADH/NADPH), flavin adenine nucleotide ($FADH_2$) and heme. Oxidoreductases can also work in conjuction with metals. Cofactors and prosthetic groups are required because oxidation and reduction functions appear to be beyond the limits of the protein capabilities. Oxidoreductases are known to play important roles in metabolic processes, such as glycolysis and oxidative phosphorylation. Classes of oxidoreductases include dehydrogenases, peroxidases, reductases and oxygenases, among others.

Fe-enzymes

Metals play roles in enzymes as cofactors. While Fe^{2+} can be incorporated directly and utilized in enzymes, Fe^{2+} is more commonly observed in metalloenzymes as part of the heme prosthetic group (34). The heme molecule is a ubiquitous cofactor used by large families of proteins which perform different functions. Electron transfer is a common function for heme enzymes. Heme can shuttle electrons between proteins during mitochondrial respiration, and can also store O_2 (35). Peroxidases are a class of heme-containing enzyme (heme enzymes) that use H_2O_2 as an oxidizing agent. Peroxidases can catalyze 1-electron or 2-electron oxidations (36). Non-heme iron dependent enzymes are important for O_2 activation, and include mononuclear and binuclear iron enzymes. Mononuclear iron enzymes catalyze many processes including biosynthesis of hormones, RNA and DNA base repair, and biosynthesis of antibitotics (37,38). Binuclear iron enzymes contain di-iron centers. Ribonucleotide is an iron-dependent enzyme that catalyzes the formation of deoxyribonucleotides from ribonucleotides. It contains a di-iron center that generates and maintains a tyrosyl radical required for catalysis (39).

RNA catalysts of electron transfer

Sen and co-workers used *in vitro* selection (SELEX, (40)) to identify single-stranded DNA and RNA fragments that could bind heme with high affinity (36). This work was motivated by the desire to identify new catalytic properties for nucleic acids, which are limited by their lack of chemical functionalities, similar to those possessed by proteins. SELEX had previously allowed the identification of both DNA and RNA aptamers that bound porphyrins and catalyzed their metallation (41,42).

Using this method, RNA-hemin complexes were identified that could catalyze peroxidase reactions (43). The DNA version of the same RNA was equally active as a peroxidase. Both the DNA and RNA constructs were G-quadruplex forming sequences. Most optimal activity was observed in sequences that form parallel-stranded G-quadruplexes (36). Hemin (Fe^{3+} heme) by itself possessed low, intrinsic peroxidase activity, so the nucleic acid scaffold was important for peroxidase activity. In addition, the nucleic acid/hemin complexes were able to catalyze oxygen transfer reactions, such as the oxidation of heteroatom and the oxidation of an electron-rich alkene (44). Catalytic efficiency (k_{cat}/K_m) of the nucleic acid enzymes were comparable to those of protein hemoenzymes.

The discovery of heme-utilizing ribozymes is a nod to the RNA world hypothesis. Heme is proposed to be an ancient molecule and a player in the postulated RNA world (45). The ability of RNA-heme complexes to perform functions that are important in contemporary hemoproteins lends plausibility to heme's presence in the RNA world, and also poses a challenge: what other catalytic abilities of hemoproteins could be recapitulated by RNA-heme complexes?

Hypothesis

Previous work showed that under early earth conditions (i.e. in the presence of Fe^{2+} in an anoxic environment), Fe^{2+} is able to replace Mg^{2+} in mediating RNA folding and function (30). We hypothesize that Fe^{2+} was an RNA cofactor on early earth when iron was benign and abundant, and that reversing the putative metal substitution in an anoxic environment by removing Mg^{2+} and Fe^{2+} would confer previously uncharacterized ability onto RNA. Fe^{2+} is able to alter its oxidation state readily, and is known to be an

important component in many oxidoreductase enzymes. For this reason, we tested the ability of RNA and Fe^{2+} to catalyze electron transfer reactions.

RNAs investigated

P4-P6 domain of the *Tetrahymena* group I intron

P4-P6 is an independent domain of the *Tetrahymena* self-splicing intron that folds to its native structure even in isolation of the intron. P4-P6 is ~160 residues long and composed of coaxially stacked Watson-Crick duplexes, with interrupting junctions that contain non-Watson Crick base pairs (46,47). Extensive tertiary interactions between the stacked helices stabilize P4-P6. The crystal structure of P4-P6 (15) revealed Mg^{2+} binding sites in the metal ion core (Figure 9).

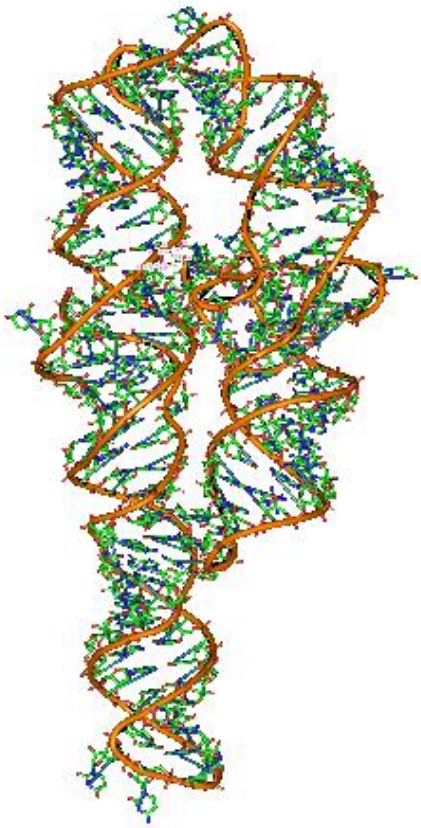

Figure 9. P4-P6 domain of *Tehtraymena* Group I intron (PDB 1GID)

Bacterial 23S rRNA

The 23S LSU rRNA of *Thermus thermophilus* contains about ~3000 residues (Figure 10). It is divided into seven domains. A central domain (Domain 0) forms the essential core of the 23S rRNA from which the other six domains are rooted. The rRNA is densely coordinated by Mg^{2+} ions which help to stabilize the secondary structure (48).

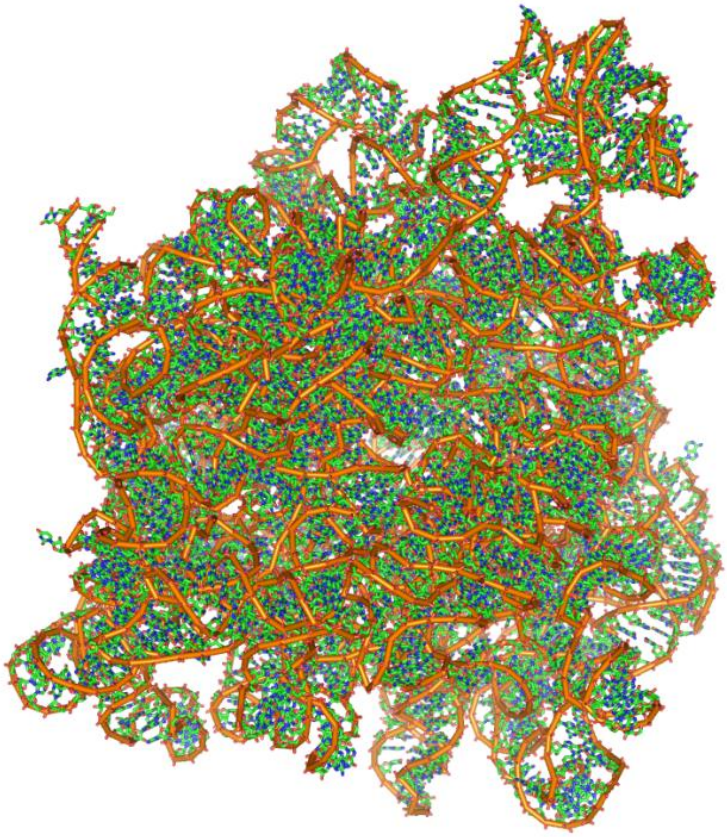

Figure 10. 23S ribosomal RNA of the *H. marismortui* LSU (PDB 1JJ2)

Model of ancestral ribosome (a-rRNA)

The a-rRNA is a molecular-level model of ancestral RNA that might have formed an ancestral PTC (a-PTC) (49). The a-PTC incorporates fragments of the 23S rRNA, fragments of ribosomal proteins and divalent cations. The ancestral rRNA fragments, taken from Domains II, IV and V, consist of rRNA that forms and surrounds the PTC

(Figure 11). These fragments were joined together, stitched by stem loops, to form a single RNA polymer that allowed the 3D structure of the PTC to be maintained, including Mg^{2+}-RNA interactions for tertiary structure formation.

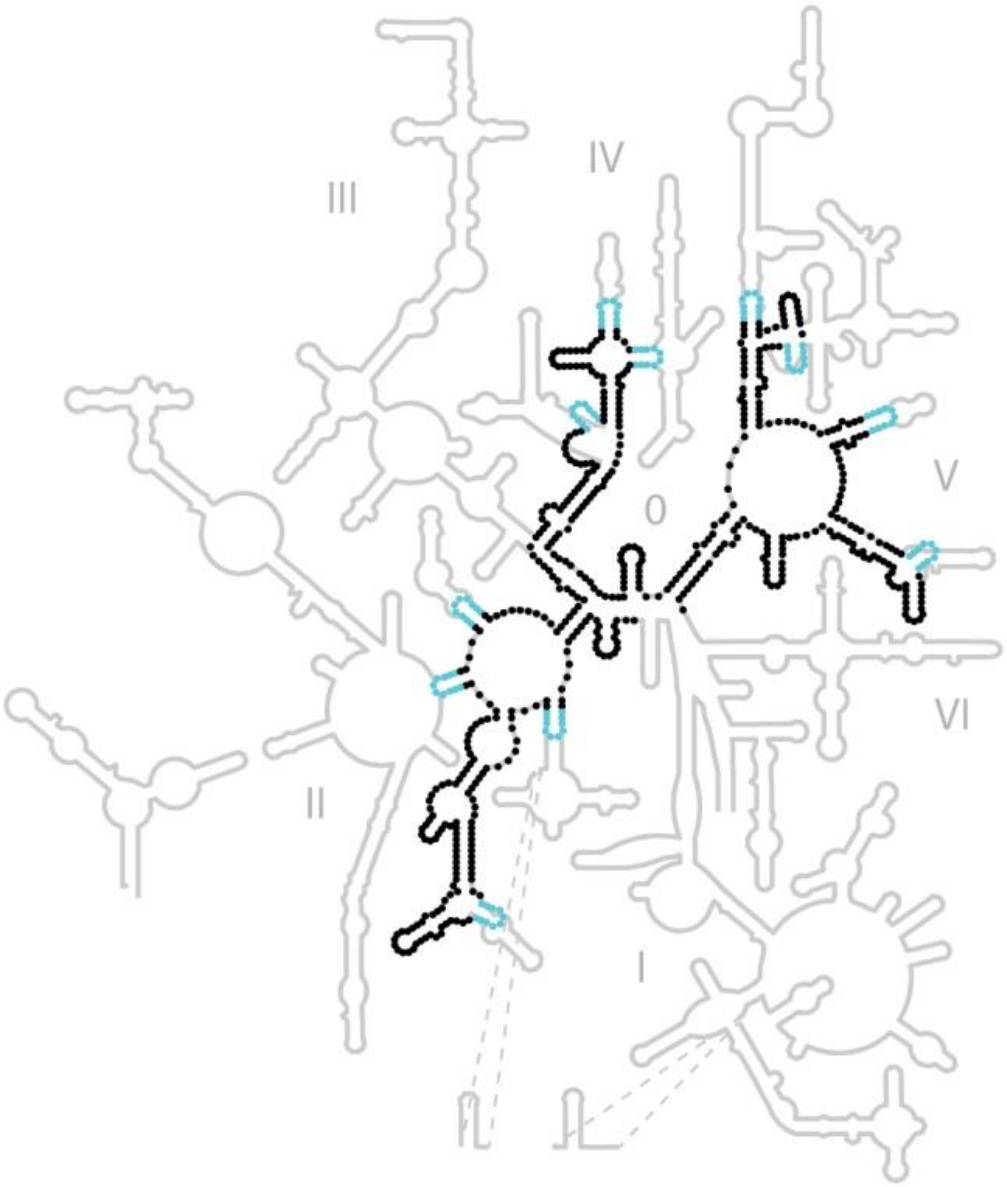

Figure 11. Secondary structure of the 23S rRNA and a-rRNA. The nucleotides of a-rRNA are indicated by black and blue dots, which are superimposed on the line representation of the 23S rRNA. The ancestral rRNA elements of a-RNA (black dots) are stitched together by stem loops (blue dots) to make a continuous strand. The RNA sequences used here are from the *T. thermophilus* 23S rRNA. Domain numbers are indicated.

Domain III of 23S rRNA

Domain III of the 23S rRNA is an independent domain that can fold to a near-native state in the absence of the rest of the LSU (50) (Figure 12). Magnesium is required for domain III to attain its native structure.

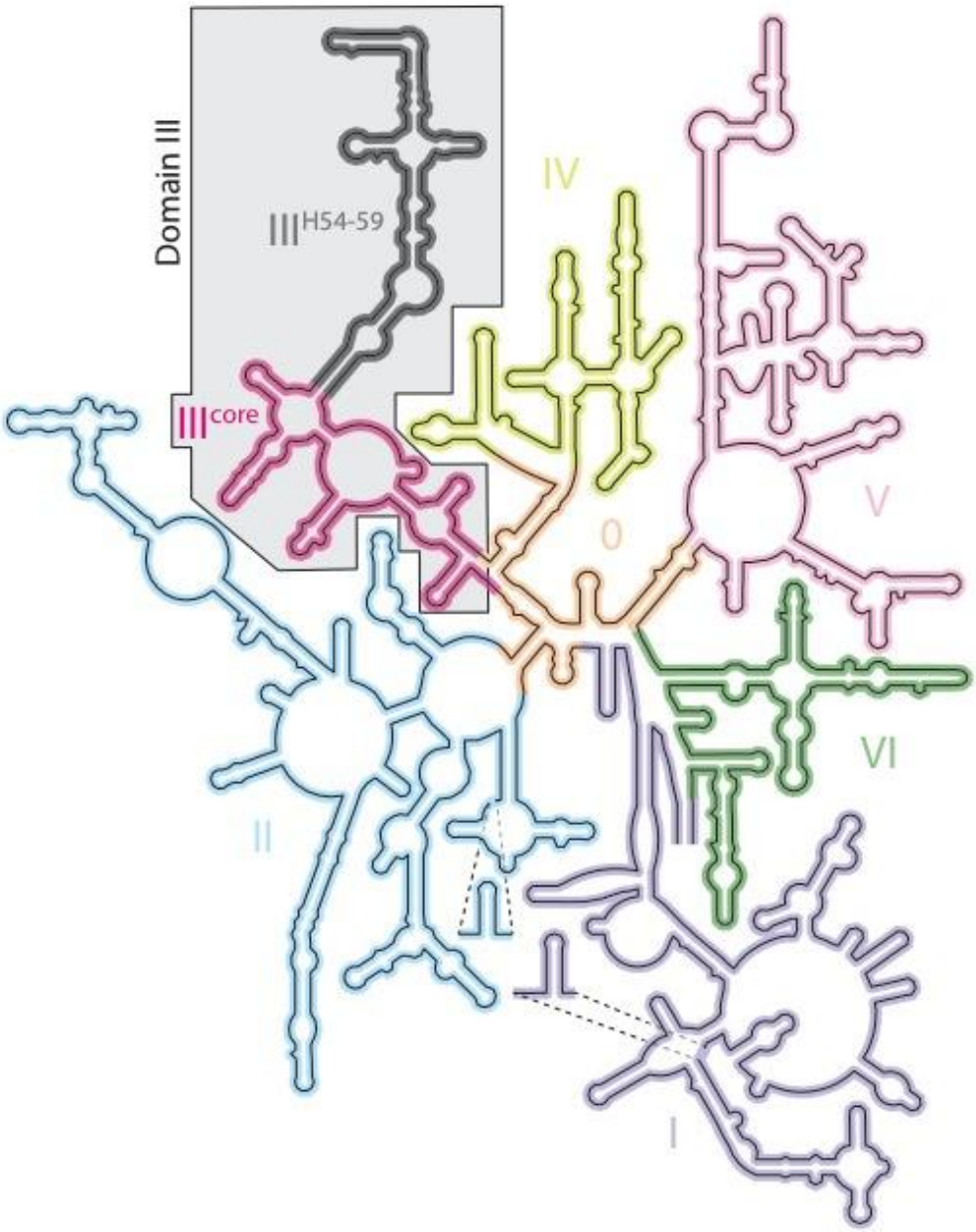

Figure 12. Domain III (shaded) and Domain III^{core} (magenta) are indicated on the secondary structure of the 23S rRNA of *T. thermophilus* as described (51). All other domains are distinguished by color. Reprinted from (52) with permission.

Domain III^{core} of 23S rRNA

Domain III^{core} of the 23S rRNA is a 199-nucleotide fragment of Domain III that folds to a near-native state (52)(Figure 12). It has self-contained networks of base-base tertiary and cation-mediated electrostatic interactions, responsible for its ability to fold autonomously into native-like structure.

Yeast tRNA-Phe

Saccharomyces cerevisiae tRNA-Phe has been used for extensive RNA-metal binding studies (Figure 13) (5) (53). Strong Mg^{2+} binding sites have been identified in yeast tRNA-Phe.

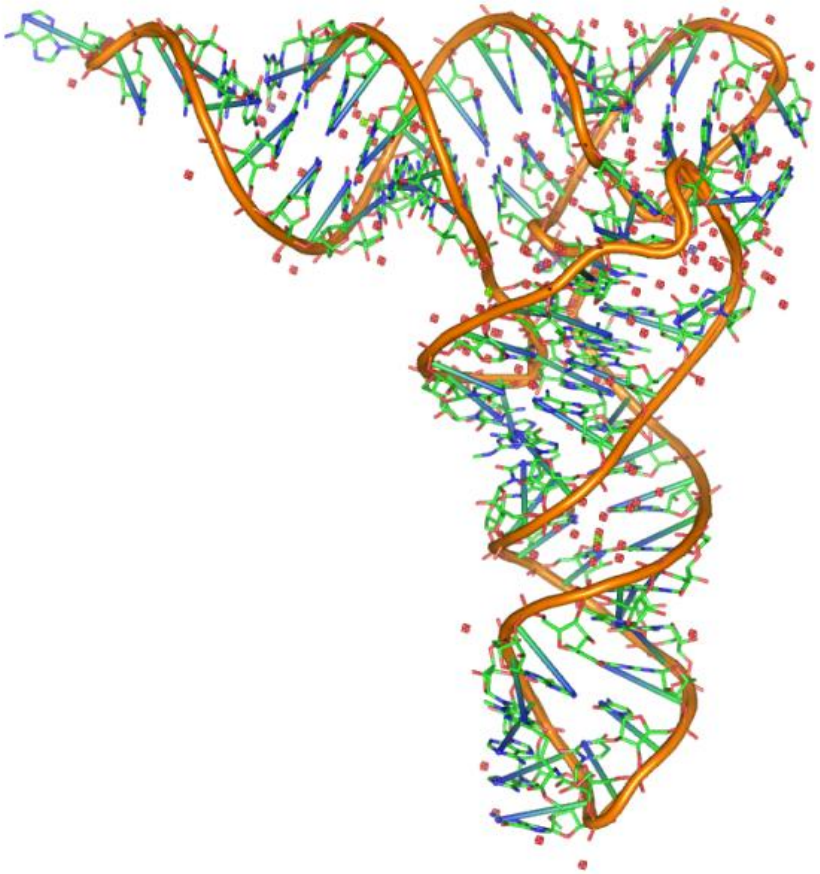

Figure 13. Yeast phenylalanine tRNA (PDB 1EHZ)

STMV genomic RNA

The RNA genome of the Satellite Tobacco Mosaic Virus (STMV) is 1058 nucleotides in length (Figure 14). SHAPE analysis on the STMV RNA revealed that Mg^{2+} has very little effect on the reactivity of the RNA, which could indicate the absence of Mg^{2+}-dependent folding or of Mg^{2+}-mediated tertiary interactions (54).

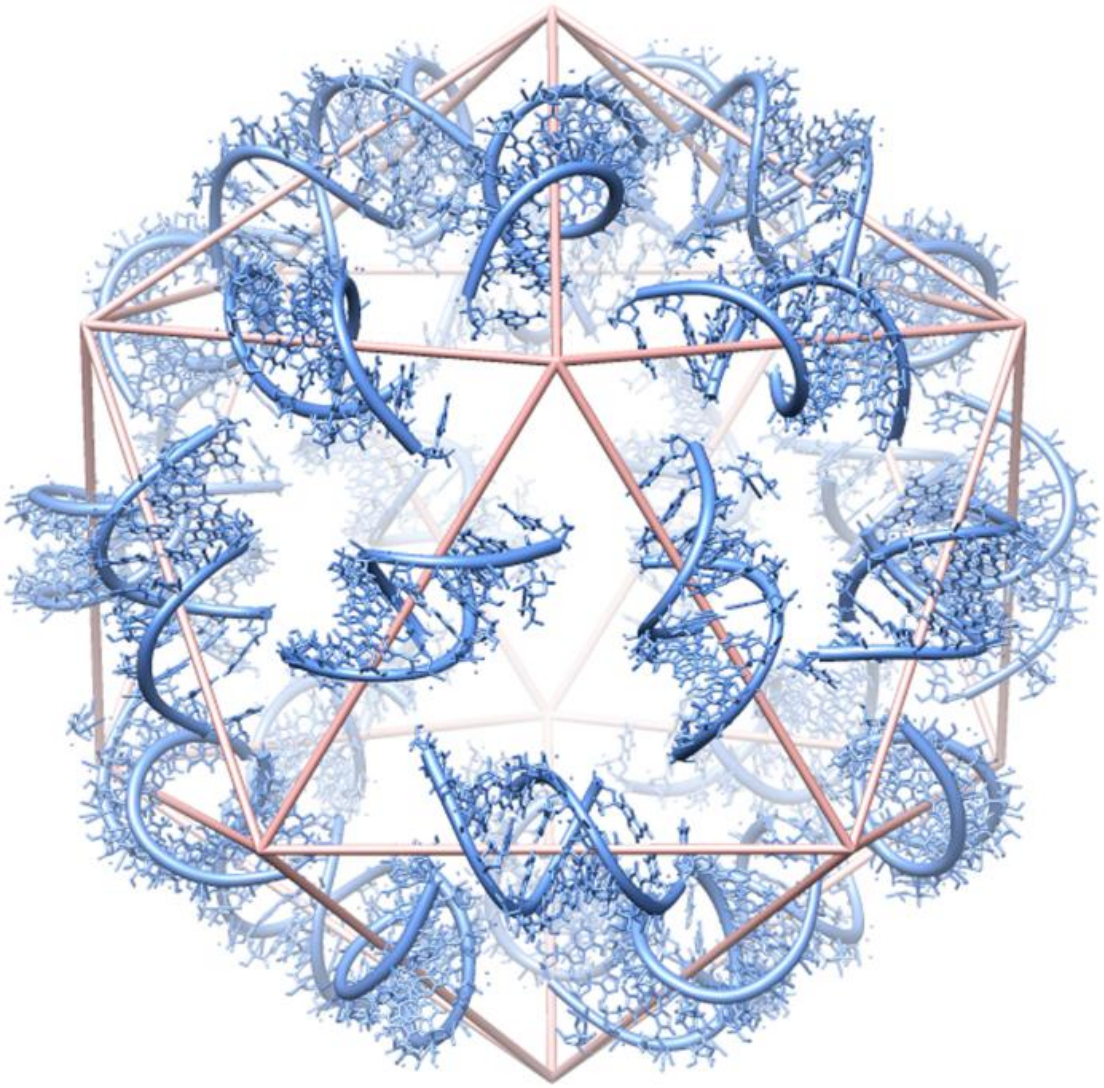

Figure 14. Distribution of double-helical RNA segments in the STMV virion. The crystal structure of STMV reveals 30 segments of double-helical RNA (blue). Each helix contains 9 base pairs, centered on a crystallographic two-fold axis. Reprinted from (50) with permission.

RNA duplex

A generic A-form RNA duplex was investigated to determine whether a regular array of phosphate groups and/or the structural features of an A-form RNA duplex are sufficient to catalyze electron transfer in combination with Fe^{2+}.

DNA duplex

Generic B-form DNA duplexes were investigated to determine whether a regular array of phosphate groups and/or the structure features of B-form RNA are sufficient to catalyze electron transfer in combination with Fe^{2+}.

Other molecules

In addition to the molecules above, a single-stranded RNA (5'-GCACU-3') was tested to probe whether a short, unstructured RNA possessed the ability to catalyze electron transfer. ATP was tested also, to see determine whether closely-spaced phosphate groups are able to perform catalysis.

The peroxidase assay

Peroxidases are enzymes that largely catalyze the reactions of the following form:

$$ROOR' + \text{electron donor } (2\ e^-) + 2H^+ \rightarrow ROH + R'OH$$

Most peroxidases use H_2O_2 as the oxidizing agent along with a colorimetric (or fluorimetric) reducing substrate to monitor peroxidase catalytic activity. Reducing substrates typically react with H_2O_2 with 1:1 stoichiometry to yield products that can be conveniently detected by spectroscopic methods.

Several substrates have been successfully used in the peroxidase assay.

2-methoxyaniline, also known as *o*-anisidine or 3,3'-dimethoxybenzidine (Figure 15), is a urinary bladder carcinogen that can be oxidized by peroxidases to a diimine (λ_{max} = 450 nm) and subsequently hydrolyzes to a quinone imine (λ_{max} = 500 nm) (55).

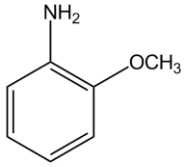

Figure 15.2-Methoxyaniline (*o*-anisidine).

3,5,3',5'-Tetramethylbenzidine (TMB) is a substrate that was identified as a less-hazardous replacement for benzidine, a carcinogenic. Peroxidase catalyzes both one and two-electron oxidations of TMB, giving a blue (one-electron, λ_{max} = 370,652 nm) and yellow (two-electron, λ_{max} = 450 nm) product (Figure 16). Two chemically distinct one-electron products of TMB are envisaged to exist in equilibrium (56).

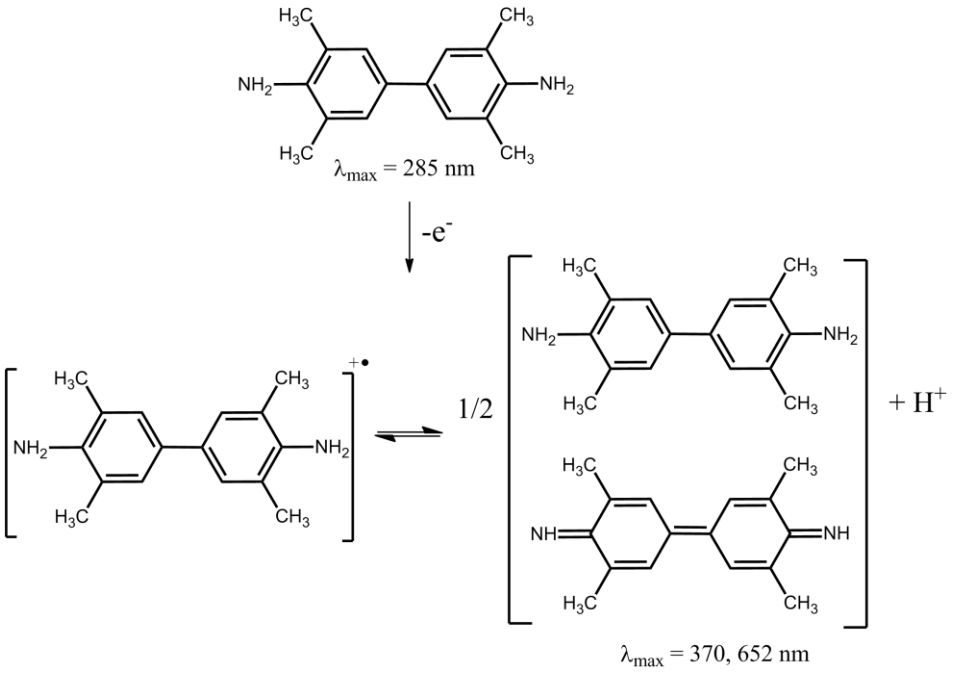

Figure 16.3,3',5,5'-Tetramethylbenzidine and the semiquinone-imine radical cation formed from oxidation. Adapted from (56).

o-Phenylenediamine is oxidized to 2,3-diaminophenazine/DAP (λ_{max} = 450 nm) by peroxidase enzymes (Figure 17). While DAP is the main product, other different products can be produced by the enzymatic reaction. Other factors make OPD a complex substrate for the peroxidase reaction, including the fact that that DAP can be obtained nonenzymatically without the aid of a peroxidase (57). For this reason, special care and conditions are required to suppress intermediates and other reaction products, as well as minimize nonenzymatic product formation.

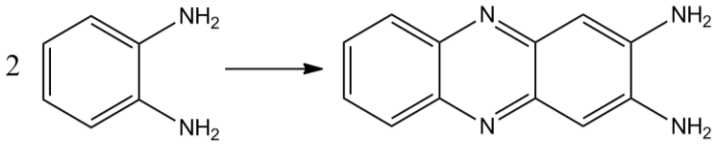

Figure 17.*o*-Phenylenediamine and 2,3-diaminophenazine oxidation product.

2,2′-Azino-*bis*(3-ethylbenzothiazoline-6-sulfonate) (ABTS), a dye, is oxidized by peroxidase to the radical cation $ABTS^{+\bullet}$ (λ_{max}=414 nm) (58). In the presence of excess H_2O_2, peroxidase-catalyzed oxidation of ABTS can lead to the formation of $ABTS^{2+}$(59) and decomposition products. This decomposition is avoided by using at most 0.5 equivalents of H_2O_2 for each equivalent of ABTS (Figure 18).

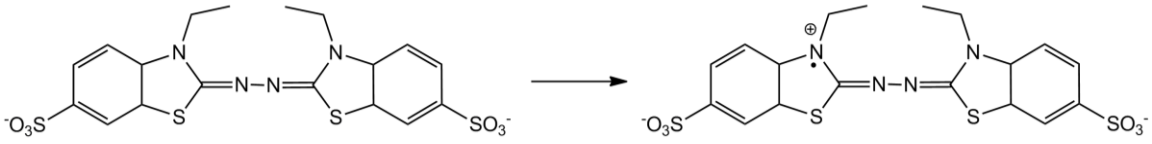

Figure 18.ABTS substrate and radical cation product, $ABTS^{+\bullet}$.

Experimental Methods

Materials

Nuclease free water (IDT) was used in all experiments involving RNA. The phenylalanine-specific tRNA from brewer's yeast [CAS#: 63231-63-0] was obtained from Sigma-Aldrich. Substrates used in the peroxidase reaction were 3,3',5,5'-tetramethylbenzidine (Sigma-Aldrich) and hydrogen peroxide (30%, Fisher Scientific). HEPES-TRIS stock buffer solutions were prepared by mixing solutions of HEPES free acid and TRIS free base in H_2O to achieve pH 7.2. Fe^{2+} solutions were prepared using $FeSO_4 \bullet 7H_2O$ (J.T. Baker).

RNA synthesis and purification

The gene for the Del C209 mutant of the P4-P6 domain of the *T. thermophila* Group I intron (18) was synthesized by recursive PCR (60). This P4-P6 mutant was used in all experiments reported. The 23S rRNA, 23S rRNA Domain III and Domain III^{core} genes were synthesized as described (50). The STMV genome was synthesized commercially (MWG Operon). All genes were confirmed by sequencing. All of the large RNAs used here (except the tRNA) were produced by *in vitro* transcription (MegaScript T7 Kit, Ambion), minimizing the possibility of contamination by protein-based electron transfer enzymes. RNAs were then precipitated in ethanol/ammonium acetate and lyophilized to powder prior to re-suspension. *In vitro* produced RNAs were further purified with an RNA Clean and Concentrator^{TM}-25 Kit (Zymo Research). RNA purity and integrity were assayed by denaturing gel electrophoresis, which indicates that the RNAs are not significantly degraded on the timescale of the electron transfer reactions. Nucleic acid concentrations were determined by absorbance at 260 nm, measured with a

Thermo Scientific NanoDrop. Mg^{2+} was removed from RNA solutions by heating with divalent cation chelation beads (Hampton Research). Mg^{2+} removal was confirmed as described (30),(61). Excess salts and other impurities in the purchased tRNA were removed with the Zymo RNA Clean and Concentrator Kit. This purification gives an overall 75% recovery yield.

Reaction conditions

All reactions were performed in an anaerobic environment to mimic the anoxic environment of early earth. Anaerobic environment was either created by positive pressure of argon or inside an anaerobic chamber.

Argon positive pressure

Solutions were deoxygenated by capping with a septum and sparging with argon. Reaction samples were also capped and sparged with argon prior to data collection. All reagents were introduced into the capped tubes via a syringe under positive argon pressure.

Anaerobic chamber (early earth simulator)

Reactions were performed within a Coy anaerobic chamber in an atmosphere of 95% argon and 5% hydrogen.

Sample Preparation

For all RNA/Fe^{2+} reactions, 3,3',5,5'-tetramethylbenzidine (TMB, Sigma-Aldrich) stock solutions were prepared in DMSO. Hydrogen peroxide (30%, Fisher Scientific) stock solutions were prepared in H_2O. HEPES-TRIS stock buffer solutions were prepared by mixing solutions of HEPES free acid and TRIS free base in H_2O to

achieve pH 7.2. Reactions were prepared by mixing the nucleic acid, TMB, and hydrogen peroxide with HEPES-TRIS buffer, pH 7.2, in a spectrophotometer cell. No reaction is observed in the sample mixture at pH 7.2. To initiate the reaction, the pH was adjusted by the addition of deoxygenated H_2SO_4(aq). The final reaction conditions, unless otherwise specified, were: TMB, 500 μM; hydrogen peroxide, 50 μM; HEPES-TRIS, 20 mM, room temperature. The nucleic acid concentrations were as follows: P4-P6 and STMV genome RNAs, 0.5 μM; 23S rRNA, 0.03 μM, ATP (Sigma-Aldrich), 80 μM; double-stranded DNA (IDT), 1.0 μM of each strand; 5-mer single stranded RNA (5'-GCACU-3', Dharmacon), 16 μM; yeast phenylalanine-tRNA, 1 μM.

Argon positive pressure

Deoxygenated Fe^{2+} solutions were prepared by dissolving a known mass of the $FeSO_4$•7 H_2O salt in H_2O, in a capped tube with a septum, and sparging with argon for two hours. H_2O was deoxygenated by capping a tube with a septum and sparging with argon for two hours. The absorbance cell was continuously capped by a septum, and reagents were introduced via a syringe under positive argon pressure. Reactions were deoxygenated by sparging with argon for 5 minutes prior to addition of deoxygenated Fe^{2+} solution and another 5 minutes of sparging with argon. The pH was adjusted to 6.5 by the addition of deoxygenated H_2SO_4(aq). The final concentration of Fe^{2+} was 6.0 μM.

Anaerobic chamber

Fe^{2+} solutions were prepared by dissolving a known mass of $FeSO_4$•7H_2O salt in degassed H_2O inside the Coy chamber. RNA samples were lyophilized in buffer, transferred to the Coy chamber as powders, resuspended in degassed H_2O inside the chamber. Fe^{2+} was added to RNA solutions and incubated for 5 minutes. TMB and H_2O_2

were then added and allowed to incubate for an additional 5 minutes. To initiate a reaction, the pH was adjusted to 6.1 by the addition of deoxygenated H_2SO_4(aq). The final concentration of Fe^{2+} was 30 μM.

RNA Stability Studies

RNA stability in Fe^{2+}/ H_2O_2 solutions under anoxic and oxic conditions was monitored as a function of time by denaturing gel electrophoresis. P4-P6 domain RNA and hydrogen peroxide in HEPES-TRIS buffer, pH 7.2, in 1.5 mL eppendorf tubes capped with septa. "Anoxic" mixtures were sparged with argon, and "oxic" mixtures were sparged with air. Deoxygenated Fe^{2+}(aq) was added to solutions while maintaining positive pressure of argon or air. As in the peroxidase reaction, the pH was dropped to 6.5 by the addition of a calibrated volume of deoxygenated H_2SO_4(aq). RNA degradation at different time points were quenched using the chelating beads. RNA stability in Fe^{2+}/H_2O_2 solutions under anoxic conditions, where [Fe^{2+}] is varied, was also monitored by denaturing gel electrophoresis. RNA reaction mixtures were prepared as described above, but with variable [Fe^{2+}], and capped with septa. These RNA degradation reactions were incubated for 15 minutes, followed by quenching with chelating beads.

Experimental Techniques

UV-Vis spectroscopy

Absorbance was recorded with a single-beam USB2000+UV-VIS, Ocean Optics spectrophotometer. The absorbance of the reaction buffer was recorded and subtracted. Data were acquired and analyzed with Logger Pro 3 (Vernier Software Technology).

Gel electrophoresis

Polyacrylamide gel electrophoresis (PAGE) is used to check the integrity of the RNA. 6%, 8M urea denaturing gels are stained with ethidium bromide to visualize bands.

Results

Electron transfer activity in RNAs

Absorbance at 652 nm was monitored in the electron transfer assay. An increase in absorbance was indicative of electron transfer catalysis. Catalysis of electron transfer was observed for a subset of the RNAs tested. The catalytic RNAs were the 23S rRNA, P4-P6 domain RNA, Domain III RNA, Domain III^{core} RNA, yeast tRNA-Phe and a-rRNA (Figures 19, 20). Non-catalytic nucleic acids were STMV, the RNA and DNA duplexes and ATP. No catalysis observed in the absence of Fe^{2+} (i.e. by RNA only) or the absence of nucleic acids (i.e. by Fe^{2+} only).

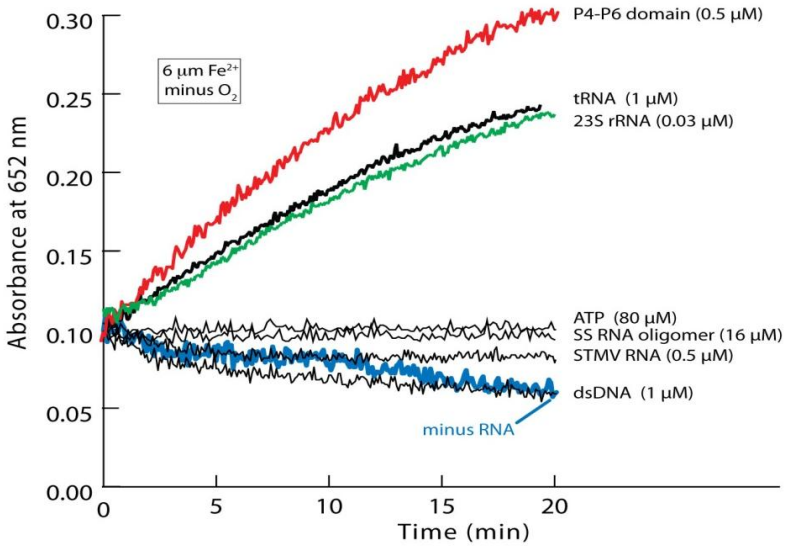

Figure 19. Some RNAs in combination with Fe^{2+} catalyze single-electron transfer. 23S rRNA, P4–P6 RNA and yeast tRNAphe do catalyze single electron transfer. ATP, SS RNA oligomer, STMV and ds DNA do not catalyze electron transfer. Experiments are performed under positive pressure of argon with 6 μM Fe^{2+}. Concentrations (in strands) of all nucleic acids are indicated.

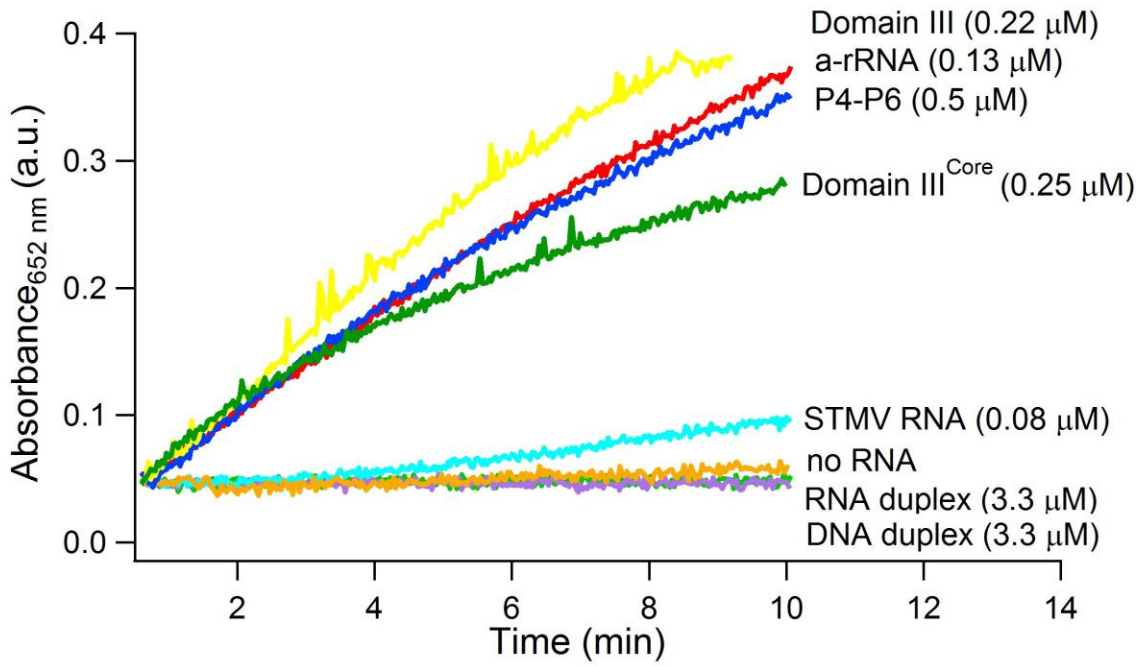

Figure 20. Some RNAs in combination with Fe^{2+} catalyze single-electron transfer. Domain III, Domain III^{core}, a-rRNA and P4-P6 RNA do catalyze single electron transfer. Inefficient catalysis is observed with STMV, and no electron transfer catalysis is observed with the RNA duplex, DNA duplex or in the absence of nucleic acids. Experiments are performed in the anaerobic chamber with 30 μM Fe^{2+}.

Effect of ribonuclease A (RNase A) on electron transfer catalysis

P4-P6 domain RNA samples were incubated with RNase A for 10 minutes to cleave the RNA backbone. RNase-digested samples were combined with Fe^{2+} and the peroxidase reagents and assayed for electron transfer activity. RNase A digestion of RNA prevents electron-transfer catalysis (Figure 21).

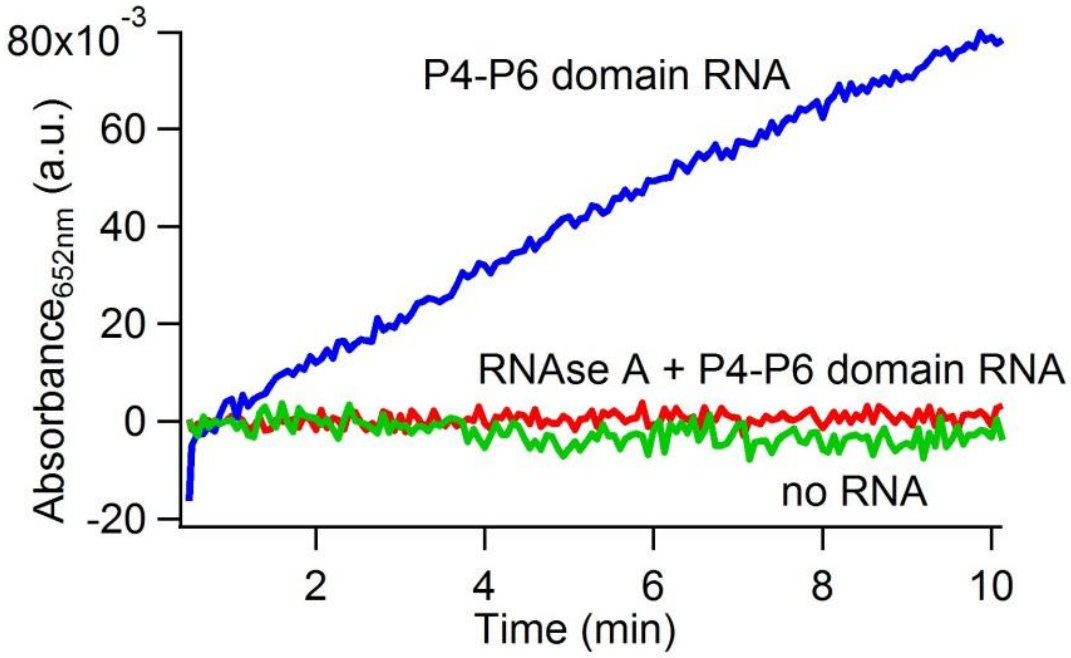

Figure 21. RNase A digestion of RNA prevents electron-transfer catalysis.

Effect of prior degradation on electron transfer catalysis

RNA samples were degraded by heat prior to use in the electron transfer assay. P4-P6 domain RNA was incubated at 80 °C in water for 0, 30, 60, 120 or 240 min. The RNA slowly degrades under these conditions. Densitometry of the stained bands on the gel indicates that the heat-induced RNA degradation is 90% complete after 4 hours (Figure 22A). Separately, P4-P6 domain RNA in water was partially degraded by the same process, for the same time increments. The partially degraded RNA from each degradation time point was assayed for electron transfer catalysis. Other experimental parameters were held constant. The reaction conditions and methods of data acquisition and analysis were the same as for the experiments described above. The rate of electron transfer is seen to decrease linearly with the extent of heat-induced RNA degradation (Figure 22B).

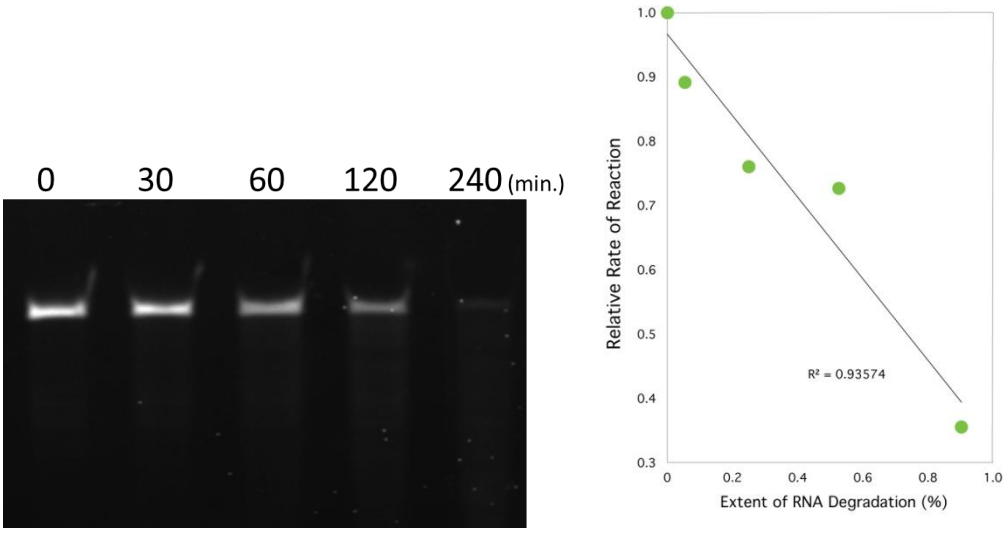

Figure 22. RNA degradation by heat. (A) The *T. thermophila* Group I intron P4-P6 domain RNA is degraded by incubation at 80 °C in water for varying lengths of time. (B) RNA samples that were degraded by heat before the RNA/Fe^{2+} electron-transfer reactions show attenuated catalysis.

Effect of Fe^{2+} incubation time on electron transfer

The incubation time of RNA with Fe^{2+} before the addition of substrates in the electron transfer assay as varied to investigate its effect on electron transfer catalysis by P4-P6 RNA. No significant variation in initial rate of electron transfer catalysis is seen in the data when the incubation time is varied (Figure 23).

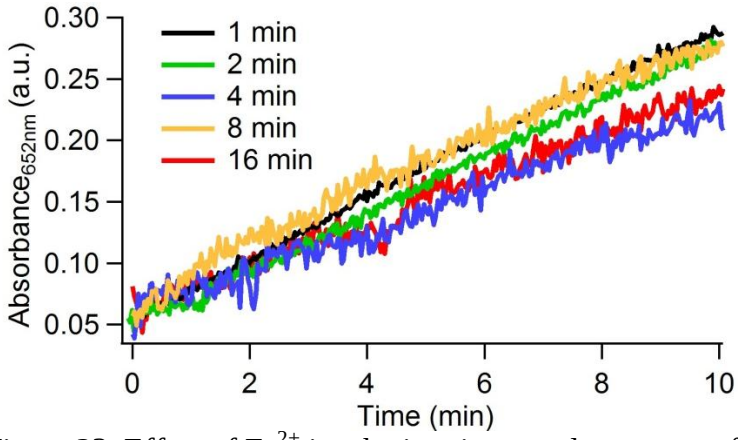

Figure 23. Effect of Fe^{2+} incubation time on electron transfer catalysis. No significant variation in the initial rate is observed when RNA incubation time with Fe^{2+} is varied.

Stability of RNA in the presence of H_2O_2 and Fe^{2+}

When Fe^{2+} is oxidized in the presence of H_2O_2, hydroxyl radicals are created that can cleave the RNA. Control experiments were performed to ensure that anaerobic conditions created in the laboratory were sufficient to maintain Fe^{2+} in the reduced form and prevent degradation of the RNA.

Time-dependent stability of RNA in Fe^{2+}/ H_2O_2

RNA stability in Fe^{2+}/ H_2O_2 solutions under anoxic and oxic conditions was monitored as a function of time by denaturing gel electrophoresis. The RNA in the anoxic solutions remains essentially intact at 60 minutes (Figure 24A) The RNA in the oxic solution is almost fully degraded at 60 minutes (Figure 24B). This experiment indicates that under the reaction conditions of electron transfer, (20 minutes, 6 μM Fe^{2+}, 50 μM, H_2O_2, anoxic), the positive argon pressure was sufficient to prevent the RNA from degradation. When an anaerobic chamber is used with different conditions (20 minutes, 30 μM Fe^{2+}, 50 μM, H_2O_2, anoxic) a-rRNA does not degrade over a period of 4 hours (Figure 25).

Effect of [Fe^{2+}] on RNA stability

RNA stability in Fe^{2+}/H_2O_2 solutions under anoxic conditions, where [Fe^{2+}] is varied, was monitored by denaturing gel electrophoresis (Figure 26). These results confirm that under the reactions conditions of electron transfer (20 minutes, 6 μM Fe^{2+}, 50 μM H_2O_2, anoxic), the positive argon pressure was sufficient to prevent the RNA from degradation. Similar results are observed when a-rRNA is incubated with varying [Fe^{2+}] in the anaerobic chamber (Figure 27).

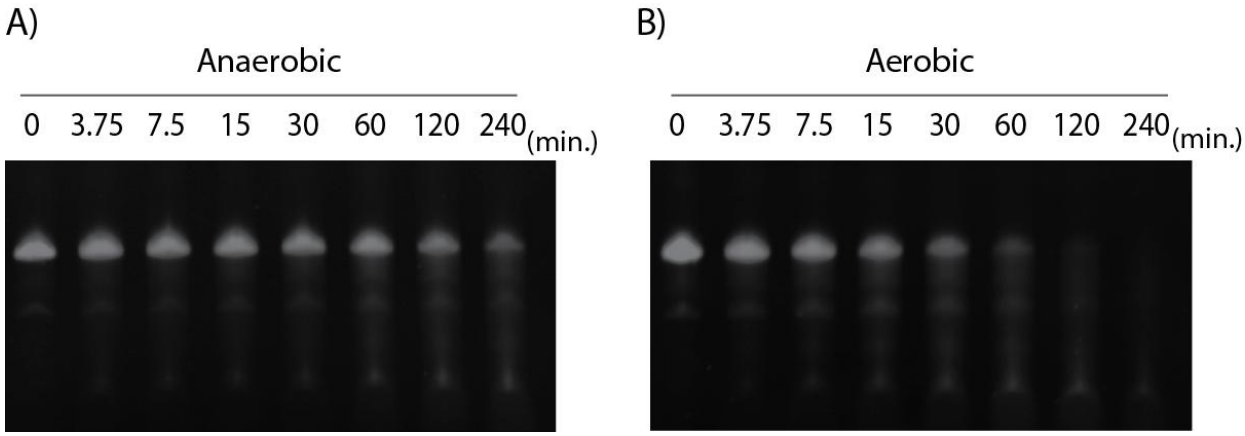

Figure 24. The stability of P4-P6 domain RNA in the presence of Fe^{2+}/H_2O_2 under (A) anoxic conditions, and (B) oxic conditions.

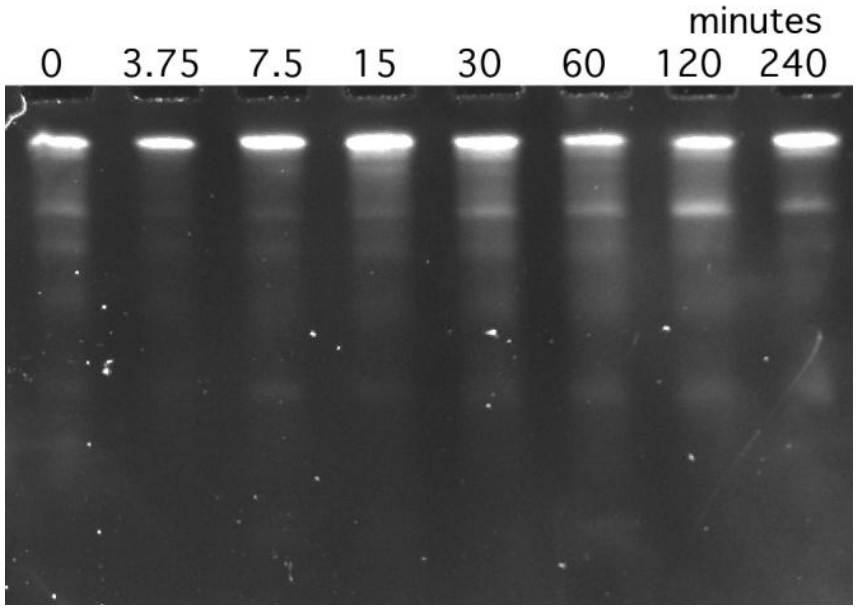

Figure 25. The stability of P4-P6 domain RNA in the anaerobic chamber.

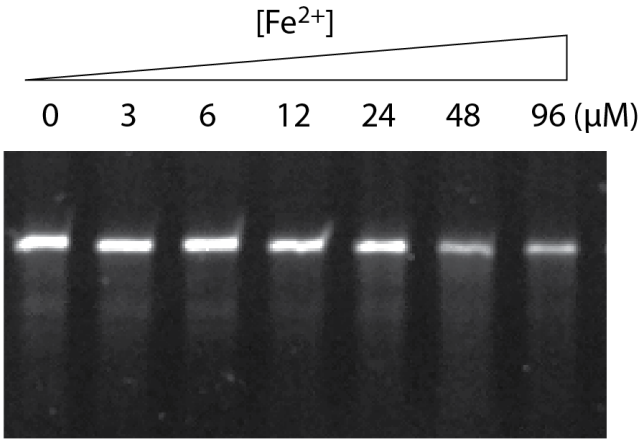

Figure 26. The stability of P4-P6 domain RNA with variable [Fe^{2+}] under anoxic conditions in the presence of H_2O_2.

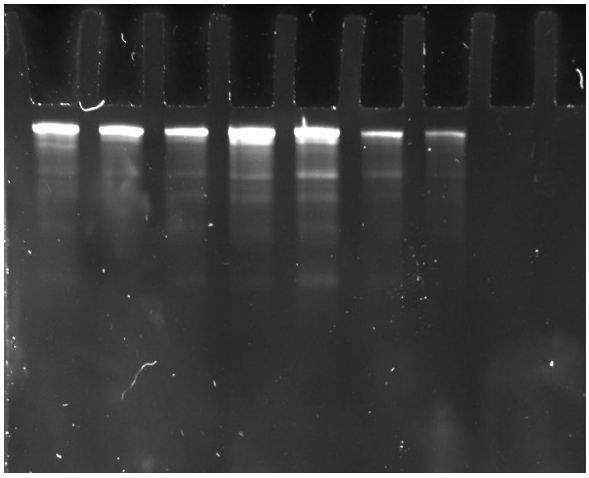

Figure 27. The stability of P4-P6 domain RNA in the anaerobic chamber with variable [Fe^{2+}].

Effect of RNA concentration on catalysis of electron transfer

The RNA/Fe^{2+} electron transfer rate increases with [RNA] (Figure 28). Reaction mixtures with P4-P6 domain RNA were prepared as described above (6 μM Fe^{2+}, 50 μM H_2O_2, 500 μM TMB under anoxic conditions) except that [RNA] was varied. The initial reaction rate (slope) was determined by linear fitting to the first three minutes of smoothed data. The rate of electron transfer increases with [RNA] while all other

components are held fixed. Beyond 0.8 μM (RNA strand) the reaction rate plateaus (not shown), presumably because Fe^{2+} becomes limiting.

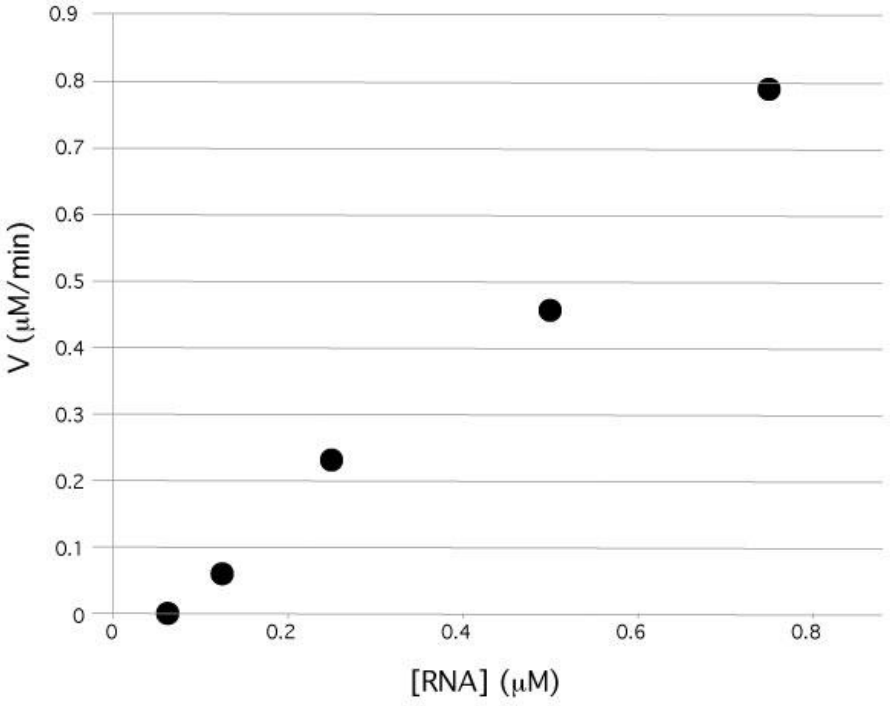

Figure 28. The effect of RNA concentration on the rate of electron transfer catalyzed by P4-P6 domain RNA. RNA concentration is in units of strands.

Effect of EDTA on catalysis of electron transfer

To determine if Fe^{2+} chelation by a simple chelator is sufficient for catalysis, we investigated a series of EDTA concentrations (3, 6, 12 μM EDTA). We do not observe catalysis with any of them (Figure 30A). We also observed that EDTA inhibits electron transfer catalysis by P4-P6 domain RNA (Figure 29).

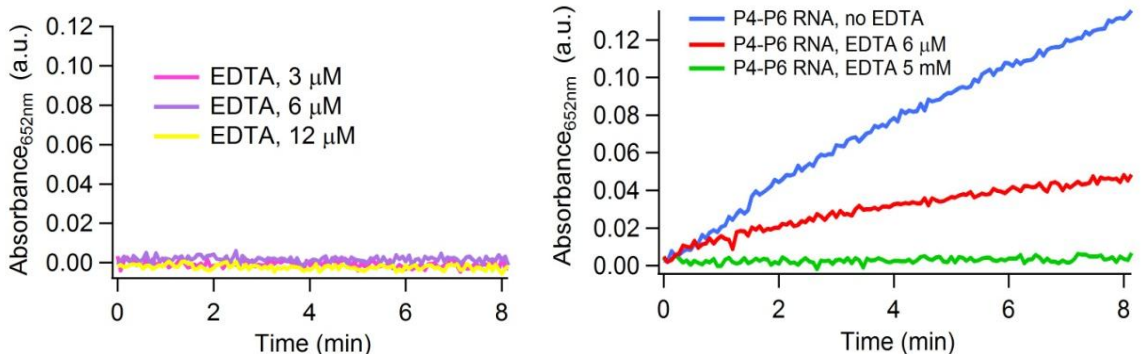

Figure 29. Effect of EDTA in electron transfer catalysis. All samples are incubated with 6 μM Fe^{2+}. A) EDTA alone is not sufficient for catalysis. B) EDTA inhibits electron transfer catalysis.

Discussion

RNA coordination of divalent metals

Differential catalysis of single-electron transfer by various RNAs was observed. This, along with the inability of Fe^{2+} alone to catalyze electron transfer, supports a model in which catalysis is mediated by well-defined three-dimensional RNA structure. We also observed that all catalytic RNAs possessed a common feature of being able to coordinate divalent cations. A subset of associated cations are chelated by multidentate chelation in the 23S rRNA(17,21). The P4-P6 domain RNA also has similarly coordinated cations. tRNA interacts strongly with divalent cations (6,62,63). In contrast, nucleotides, small ssRNA, B-DNA, A-RNA duplexes and STMV genomic RNA lack the potential to form well defined, Mg^{2+}-mediated three dimensional structures. These molecules are all less efficient in electron-transfer catalysis.

Structures of RNA-Fe^{2+} catalytic complexes

Electron transfer experiments were performed in 20 mM TRIS-HEPES buffer and 6 μM divalent, low-salt conditions that are not sufficient to fully fold the RNAs to their

native states. RNAs will fold to the same state with either Mg^{2+} or Fe^{2+} in the presence of sufficient divalent. Therefore the structures of RNA-Fe^{2+} complexes that yield catalysis still need to be characterized. A-form regions of RNAs can provide specific binding sites for Mg^{2+}(64,65).

Intrinsic redox catalytic activity in RNA

Previously, Suga and co-workers used *in vitro* selection to obtain redox-active RNA (66). This observed activity requires the presence of a heme cofactor. Work by Sen and Poon has produced RNAs which can enhance the redox activity of porphyrins (67). Our work shows that some of the most abundant and evolutionarily conserved RNAs have an intrinsic redox functionality that is simply activated by interaction with Fe^{2+}. These findings are fundamentally different than previous redox-active RNAs because they do not require non-metal cofactors. These results indicate that there are more potential functions for RNA sequences, that is, that RNA sequence space is more densely populated with function than previously expected.

Concluding Remarks

Electron transfer catalysis is important in metabolic activity. Our results suggest that RNA may have possessed the ability to catalyze electron transfer, an ability which was attenuated in RNA by photosynthesis and the rise of oxygen. This newly observed catalytic function in RNA, under early earth conditions, presents an expansion of the apparent catalytic power of RNA. This adds a new dimension to the RNA world hypothesis, suggesting that sophisticated biochemical transformations were possible in an RNA world. Further investigation of RNAs under early earth conditions may uncover

even more previously unknown RNA catalytic potential. We believe that RNA function, in analogy with protein function, can be fully understood only in the context of association with a range of possible metals. The RNA-Fe^{2+} to RNA-Mg^{2+} hypothesis is in close analogy with known metal substitutions in metalloproteins (68-73). For example, an ancestral ribonucleotide reductase (RNR) spawned di-iron, di-manganese and iron-manganese RNRs (74).

CHAPTER THREE

KINETICS AND MECHANISM OF ELECTRON TRANSFER ACTIVITY OF RNA AND FE^{2+}

Introduction

Some of the data in this chapter is adapted from previously published work: Hsiao, C., Chou, I.-C., Okafor, C.D., Bowman, J.C., O'Neill, E.B., Athavale, S.S., Petrov, A.S., Hud, N.V., Wartell, R.M., Harvey, S.C. *et al.* (2013) Iron(II) plus RNA can catalyze electron transfer. *Nature Chemistry*, 5, 525-528. It is reproduced with permission. I contributed to this work by assisting with experimental design as well as performing Michaelis-Menten experiments, competition experiments, and ribozyme-ion activity experiments.

RNA-Fe^{2+} electron transfer ribozymes were further investigated to investigate various properties of their catalysis. The Michaelis-Menten formalism was used to compare their similarity to protein enzymes. A previously described method (75) was used to identify the number of cations required to facilitate RNA catalysis. Competition assays were used to understand the effect of RNA metal-binding properties on catalysis.

Michaelis-Menten kinetic model

According to the Michaelis-Menten kinetic model of enzymatic reactions, the rates of enzymatic reactions increase linearly with the increase of substrate of concentration, up to a certain substrate concentration where the enzyme is saturated. Beyond this point, increase in substrate concentration does not cause an increase in initial

rate. The Michaelis-Menten equation describes how the initial rate of enzymatic catalysis, v_o, depends on substrate concentration [S].

$$v_o = \frac{V_{max}[S]}{K_M + [S]}$$

The Michaelis constant, K_M, is equal to the substrate concentration when the rate is half of the maximum velocity, V_{max}. K_M provides a measure of the substrate affinity for the enzyme, i.e. a pseudo dissociation constant for ES, the enzyme substrate complex. The k_{cat}, the turnover number, is calculated by dividing V_{max} by $[E_t]$. k_{cat} provides a measure of the conversion of substrate to product. k_{cat}/K_M yields a parameter that is representative of the catalytic efficiency of any enzyme. This assay provides a convenient way to measure the efficiency of an enzyme.

Ribozyme-ion requirements

A series of hammerhead ribozymes that cleave RNA upon binding to divalent metal cations were isolated (75). The relationship between the ribozyme activity and the metal ion concentration was obtained from a plot of log rate of RNA cleavage versus log [cation]. The value of the slope was interpreted as being equal to the number of rate-limiting metal binding sites that must be occupied for activation of the ribozyme. This characterization provides structural information about the catalytically-active RNA-metal complex.

Experimental Methods

Materials

Nuclease free water (IDT) was used in all experiments involving RNA. NaCl was obtained from VWR. $MnSO_4$ was obtained from Fisher Scientific. All other substrates were obtained from sources previously described (Chapter 2).

RNA synthesis and purification

P4-P6 domain RNA, the 23S rRNA, 23S rRNA Domain III and Domain III^{core} , a-rRNA and STMV genome RNA were synthesized and purified as previously described. The yeast phenylalanine tRNA obtained and purified as previously described.

Reaction conditions

All reactions were performed in an anaerobic environment to mimic the anoxic environment of early earth. Anaerobic environment was either created by positive pressure of argon or inside an anaerobic chamber, as previously described.

Sample Preparation

For all RNA/Fe^{2+} reactions, 3,3',5,5'-tetramethylbenzidine, hydrogen peroxide and HEPES-TRIS stock solutions were prepared as previously described.

Michaelis-Menten kinetic experiments

P4-P6 domain RNA, 23S rRNA and a-rRNA were used in Michaelis-Menten experiments. The *in vitro* transcript of 23S rRNA or P4-P6 Domain RNA, after heat treatment with divalent cation chelation beads, was dissolved in deoxygenated H_2O and mixed with deoxygenated Fe^{2+}(aq). A mixture of TMB/ H_2O_2 in HEPES-TRIS buffer pH

7.2, in a 10 mm rectangular absorbance cell was capped by a septum and deoxygenated for 5 min. Deoxygenated RNA/Fe^{2+} solution was added into the deoxygenated TMB/ H_2O_2. To initiate the reaction, the pH was dropped to 6.5 by the addition of deoxygenated H_2SO_4(aq). The final concentrations were 0.03 μM 23S rRNA or 0.5 μM P6-P6 Domain RNA (strand); 6 μM Fe^{2+}; 500 μM TMB; 20 mM HEPES-TRIS; variable (0-100 μM) H_2O_2.

a-rRNA Michaelis-Menten experiments were performed inside the anaerobic chamber. a-rRNA samples were lyophilized in buffer, transferred to the Coy chamber as powders, resuspended in degassed H_2O inside the chamber. Fe^{2+} was added to RNA solutions and incubated for 5 minutes. TMB and H_2O_2 were then added and the mixture was allowed to incubate for an additional 5 minutes. To initiate a reaction, the pH was adjusted to 6.1 by the addition of deoxygenated H_2SO_4 (aq). The final concentrations were 0.13 μM a-rRNA (strand); 30 μM Fe^{2+}; 500 μM TMB; 20 mM HEPES-TRIS and 0-100 μM H_2O_2.

Ribozyme-ion dependence experiments

P4-P6 domain RNA, TMB and H_2O_2 were dissolved in water and deoxygenated by sparging with argon for 5 minutes prior to addition of deoxygenated Fe^{2+} solution and another 5 minutes of sparging with argon. To initiate the reaction, the pH was adjusted to 6.5 by the addition of deoxygenated H_2SO_4(aq). [Fe^{2+}] was varied.

Competition experiments

P4-P6 domain RNA, TMB and H_2O_2 were dissolved in water. $MgCl_2$, $MnCl_2$ or NaCl was added to the reaction mixture, which was capped by a septum in an absorbance cell and deoxygenated for 5 min by sparging with argon. Deoxygenated RNA/Fe^{2+}

solution was added into the deoxygenated TMB/H_2O_2, followed by another 5 min of sparging. To initiate the reaction, the pH was dropped to 6.5 by the addition of deoxygenated H_2SO_4 (aq). The final concentrations of Mn^{2+}, Mg^{2+} or Na^{+} were varied, ranging from 0 to 80 mM.

Results

Michaelis-Menten kinetics characterization of RNA-Fe^{2+} electron transfer

For some of the RNAs that displayed activity, the catalytic nature of the electron transfer reactions was supported by standard enzyme assays. For 23S rRNA, P4-P6 domain RNA and a-rRNA, the electron transfer reaction was observed to saturate with increasing substrate concentration, rather than increase monotonically.

P4-P6 domain RNA

Kinetic parameters for single-electron transfer catalyzed by P4-P6 domain RNA with Fe^{2+} were determined by fitting data to a Michaelis-Menten model (Figure 30). Nonlinear regression analysis of the experimental data on a Lineweaver-Burke plot shows that k_{cat} = 2.2 x 10^{-2} s^{-1}, K_m = 4.15 x 10^{-6} M and k_{cat}/K_m = 5.3 x $10^3 M^{-1}s^{-1}$.

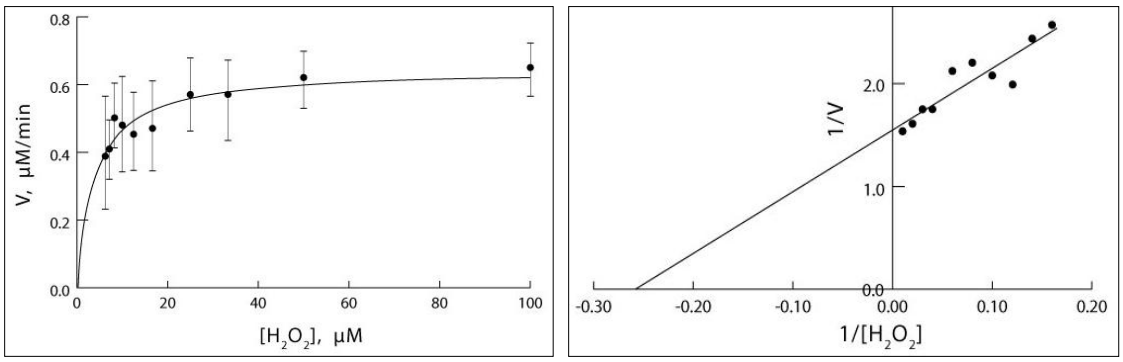

Figure 30. Kinetics of the electron-transfer reaction catalyzed by the P4–P6 domain of the *T. thermophila* Group 1 intron can be fit to the Michaelis–Menten model. Michaelis-Menten fit of the data (left) and Lineweaver-Burke plots (right) are shown.

23S rRNA

Kinetic parameters for single-electron transfer catalyzed by 23S rRNA were determined as follows: k_{cat} = 1.28 s^{-1}, K_m = 1.75 x 10^{-5} M and k_{cat}/K_m = 7.3 x10^4 $M^{-1}s^{-1}$ (Figure 31).

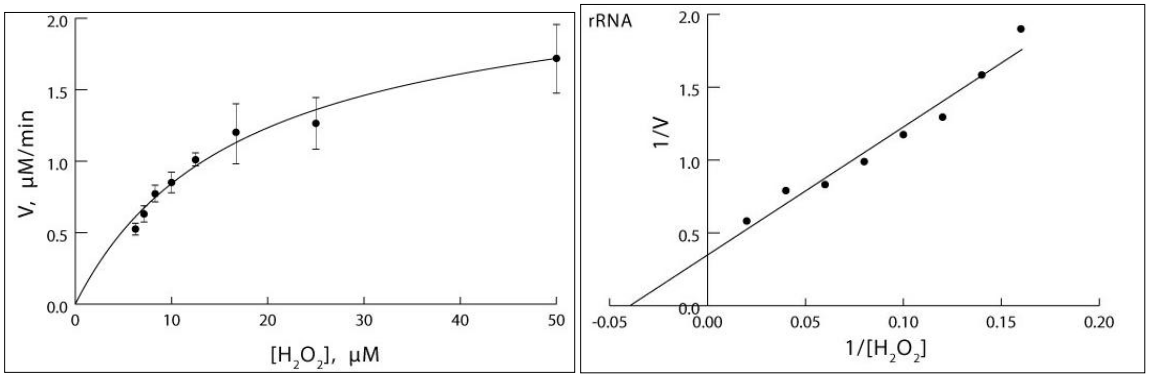

Figure 31. Kinetics of the electron-transfer reaction catalyzed by the 23S rRNA can be fit to the Michaelis–Menten model. Michaelis-Menten fit of the data (left) and Lineweaver-Burke plots (right) are shown.

a-rRNA

Kinetic parameters for a-rRNA were determined as follows: k_{cat} = 0.14 s^{-1} and K_m = 9.6 x 10^{-6} M, with k_{cat}/K_m =1.4 x 10^4 $M^{-1}s^{-1}$ (Figure 32).

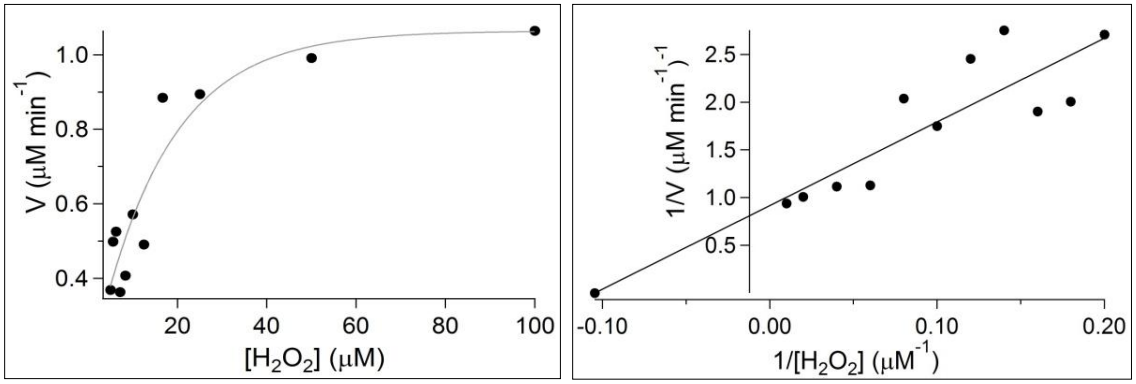

Figure 32.Kinetics of the electron-transfer reaction catalyzed by a-rRNA can be fit to the Michaelis–Menten model. Michaelis-Menten fit of the data (left) and Lineweaver-Burke plots (right) are shown.

Ribozyme-ion dependence

The concentration of Fe^{2+} in the electron transfer was varied in the electron transfer assay to obtain the ion dependence of catalytic activity. Initial rates of catalysis were plotted as a function of [Fe^{2+}]. A slope of one was obtained in the log-log graph (Figure 33).

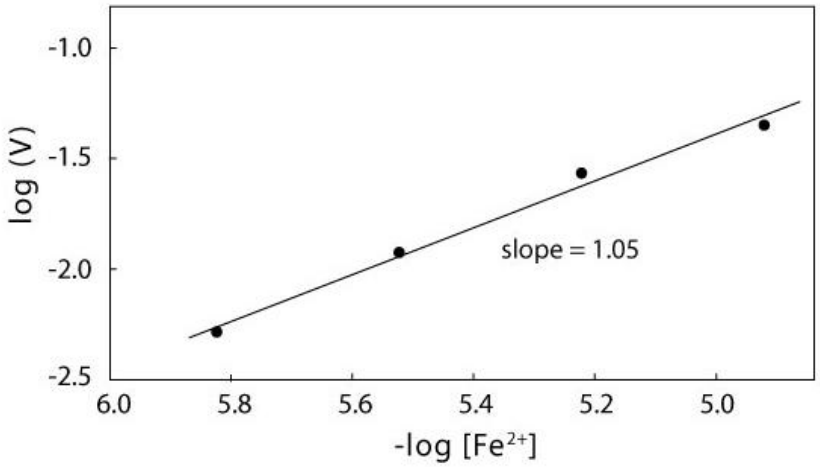

Figure 33. The Fe^{2+}-dependence of the reaction rates catalyzed by P4–P6 domain RNA.

Effect of Mg^{2+} and Mn^{2+} on catalysis of electron transfer

Divalent metal cations Mg^{2+} and Mn^{2+} were added to the P4-P6 domain RNA-catalyzed electron-transfer reactions to investigate the effect of the presence of competing divalent cations (Figure 34). At low concentrations equivalent to iron concentrations, a small inhibitory effect on electron transfer catalysis is observed, with a larger effect observed with Mn^{2+}. As the concentration of Mg^{2+} is increased, more inhibition of catalysis is observed (Figure 35).

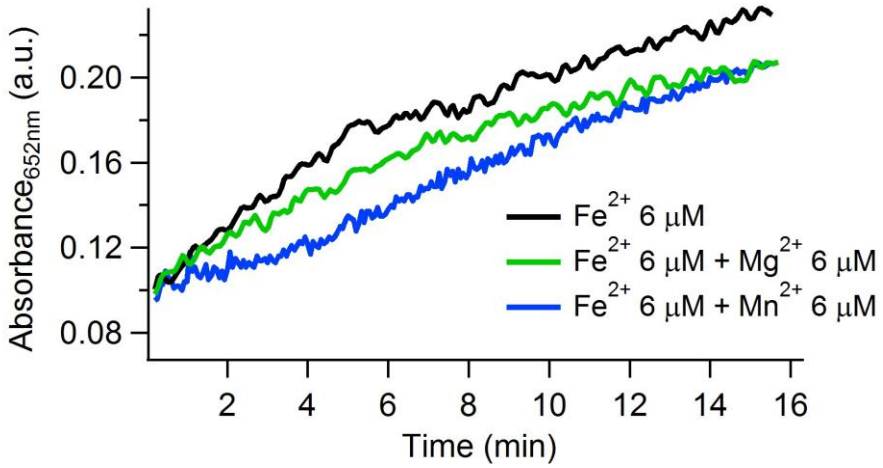

Figure 34. The effect of Mn^{2+} and Mg^{2+} on electron transfer.

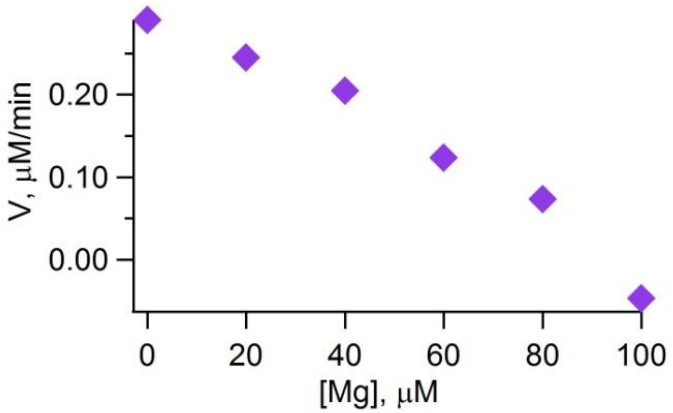

Figure 35. Effect of [Mg^{2+}] on the rate of electron transfer by the P4-P6 domain RNA.

Effect of sodium on catalysis of electron transfer

The effect of sodium on the rate of electron transfer was examined. Under normal reaction conditions (i.e. H_2O_2, 50 μM; TMB, 500 μM; Fe^{2+}, 6 μM, pH 6.5), high concentrations of Na^+ inhibited the reaction (Figure 36).

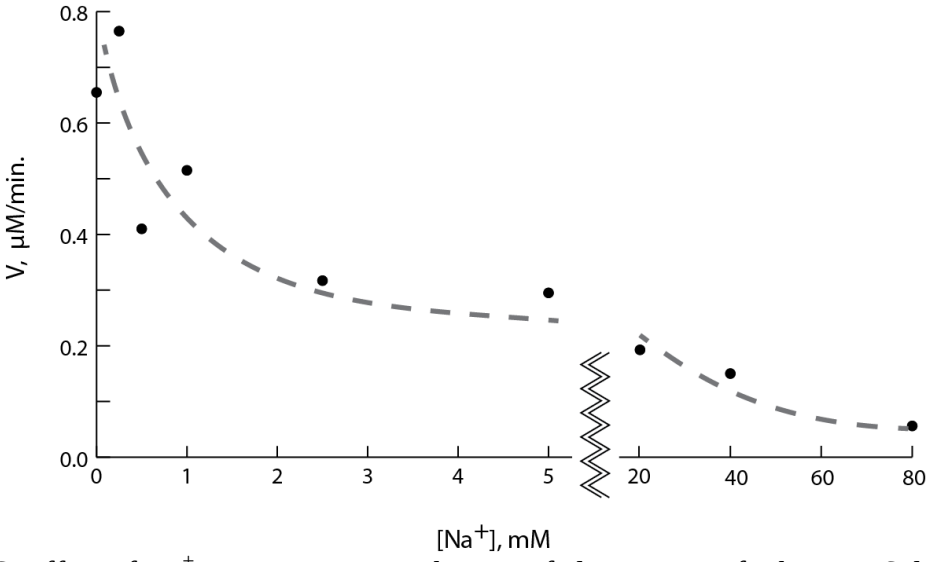

Figure 36. Effect of Na^+ concentration on the rate of electron transfer by P4-P6 domain RNA.

Electron transfer with other reducing substates

The one-electron oxidation of *o*-phenylenediamine (OPD) to 2,3-diaminophenazine (DAP) (Figure 18) by P4-P6-Fe^{2+} was tested, to investigate the ability of RNA and Fe^{2+} to utilize substrates other than TMB. We observe similar catalysis with OPD as previously observed with TMB, dependent on the presence of Fe^{2+} (Figure 37A). Varying the concentration of OPD reveals enzymatic behavior consistent with Michaelis-Menten kinetics, as the rate of catalysis appears to saturate with increasing [OPD] (Figure 37B).

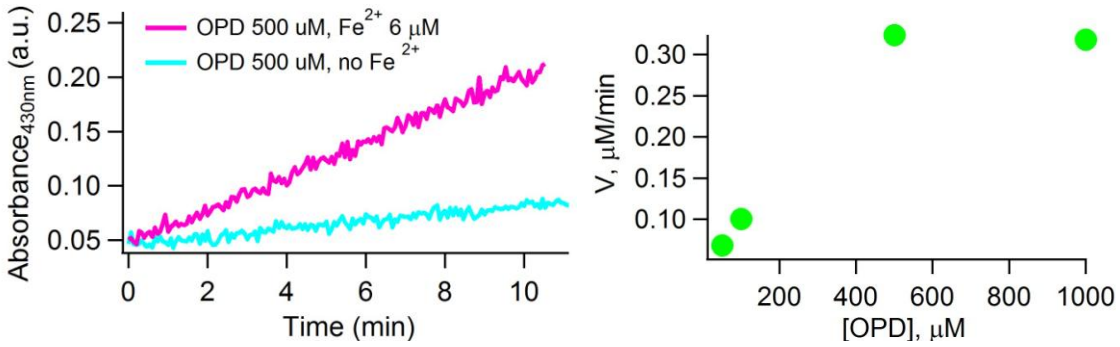

Figure 37. Electron transfer catalysis of OPD to DAP. A) Reaction occurs in the presence of Fe^{2+}. B) Rate of catalysis saturates with increasing OPD concentration.

Discussion

Catalytic competence of electron-transfer ribozymes

We found that three of the RNAs tested (P4-P6 domain RNA, 23S rRNA and a-rRNA) adhered to Michaelis-Menten kinetics, with initial rate increasing linearly with substrate concentration, subsequently saturating. We observed that the order of catalytic efficiency (measured by k_{cat}/K_m) in the three RNAs is 23S rRNA > a-rRNA ≥ P4-P6. Observed K_ms for the three RNAs were within an order of magnitude of each other, being higher in a-rRNA and P4-P6 than 23S rRNA. While an order of magnitude difference in K_m value is not considered by some to be significant for protein enzymes, it is typically considered significant for (less active) ribozymes. K_m reports on the affinity of the enzyme for the substrate, so our data could indicate that substrate binding is slightly less favored in the large 23S rRNA, compared to the smaller P4-P6 and a-rRNA.

The major contributor to the difference in catalytic efficiency arises from the k_{cat}, which is 3-4 times higher in 23S rRNA than in P4-P6 domain RNA and a-rRNA. The higher k_{cat} in 23S rRNA indicates that it converts more substrate to product, compared to the other RNAs. We believe that the ability of the RNA to chelate divalent metals is

important for catalysis. Our observation of higher efficiency with the 23S rRNA is consistent with this idea, as the 23S rRNA has several more chelated Mg^{2+} ions (~41) than possessed by P4-P6 or a-rRNA.

We have reported enzyme efficiencies using RNA concentration in units of strands of RNA present ($[RNA]_{strand}$). Alternatively, concentrations could be reported on a nucleotide basis ($[RNA]_{nucleotide}$), which is calculated by multiplying $[RNA]_{strand}$ by the number of nucleotides in the RNA molecule. While the $[RNA]_{strand}$ are different for the three RNAs in our experiments (a-rRNA, 0.13 μM, P4-P6 RNA 0.5 μM, 23S rRNA 0.03 μM), $[RNA]_{nucleotide}$ is approximately equal for all three (a-rRNA, 80 μM, P4-P6 RNA 80 μM, 23S rRNA 87 μM). The appropriate choice of concentration units, strand or nucleotide, is dependent on whether the Fe^{2+} binds at a few highly specific sites, or less specifically to many sites on the RNAs. Regardless, 23S rRNA is the most efficient catalyst per strand and per nucleotide.

Some of the RNAs tested that exhibited electron transfer activity did not adhere to Michaelis-Menten kinetics. These include tRNA, Domain III RNA and Domain III^{core} RNA. Increasing the concentrations of these RNAs did not lead to a consistent increase in the initial catalysis rate, or an eventual saturation. More work needs to be done to determine the nature of Fe^{2+}-binding that is responsible for enabling catalysis.

Ion-dependence of electron transfer catalysis

Using an approach employed previously by Breaker and co-workers (75), we were able to determine the number of cations required for catalysis. If a linear relationship is observed in the log rate versus log[cation] for ribozyme activity, the slope could be interpreted as the number of cations required by the ribozyme for catalysis. With

this method, we observe a slope of 1 in P4-P6. In other words, there is a 10-fold increase in the activity of the P4-P6-Fe^{2+} ribozyme for every 10-fold increase in the Fe^{2+} concentration. Although more complex models cannot be excluded, these observations are consistent with a mechanism in which occupancy of a single Fe^{2+} confers catalytic activity to P4-P6 RNA. Future work will determine whether the same finding will apply to other catalytic RNAs.

Monovalent and divalent competition with Fe^{2+} for electron transfer activity

Na^{+}, in high concentrations, inhibits electron transfer activity. RNA does not bind sodium specifically, and sodium does not bind RNA strongly in divalent-specific binding sites. Therefore this appears to be an electrostatic effect, where high sodium keeps Fe^{2+} from binding to the RNA, inhibiting the formation of the redox-active RNA-Fe^{2+} complex. Divalent metals are observed to compete more effectively with Fe^{2+} for binding to the RNA. This is consistent with the idea that RNA has divalent metal binding pockets that strongly bind Mg^{2+} or Fe^{2+}, or other divalents such as Mn^{2+}.

True enzymatic nature of a model of the ancestral ribosome

The ancestral core of the ribosome, modeled here by a-rRNA, is considered to be one of the most ancient RNA structures remaining in extant biology. Results obtained here suggest that an ancient RNA, which presumably hails from the RNA world, is an efficient oxidoreductase ribozyme under ancient earth conditions. By contrast, in the presence of Fe^{2+} and O_2, the RNA is very quickly cleaved by Fenton chemistry. In the absence of Fe^{2+}, RNA lacks oxidoreductase function. The work here suggests that the catalytic function of the ancestral core may have been more polymorphic than previously understood. Catalysis of redox chemistry seems probable on the ancient earth.

Concluding Remarks

While some light has been shed on the nature of electron transfer catalysis by RNA, there are still some questions that need to be addressed. The observation that some RNAs adhere to Michaelis-Menten kinetics, while others do not, might indicate a key structural difference in RNA, or a difference in ion-binding. Kinetic parameters confirm that the observed RNA catalysis is effective. However, if the RNA is not saturated with Fe^{2+} under the conditions of our kinetics experiments, the obtained data might underestimate the true k_{cat}.

It would be advantageous to explore the ribozyme-ion dependence of additional RNAs, by checking for a linear relationship between the rate of catalysis and iron concentration. These experiments might reveal additional features of RNA responsible for catalytic activity and Michaelis-Menten kinetics. For example, a correlation between the number of Mg^{2+} coordination sites in the RNA and the number of ions required for catalytic activity for the RNA would indicate that specific Mg^{2+} binding sites are important for this catalysis. The lack of such a correlation would support a model where Fe^{2+} binds less specifically to the RNA.

The observation of true enzymatic behavior in a-rRNA, a model of ancient RNA, demonstrates the importance of investigating ancient models under appropriate conditions, i.e. early earth conditions with no oxygen and Fe^{2+}. We observe that divalent metals other than Fe^{2+} attenuate the observed catalysis. Mg^{2+} is not able to facilitate electron transfer with RNA (61) because it is in a fixed oxidation state. Mn^{2+} is also unable to facilitate electron transfer with catalysis. This result further illustrates the idea

that RNA function, both in early earth and extant conditions, can be fully understood only in the context of association with a range of possible metals.

CHAPTER FOUR

MAGNESIUM BINDING SITES IN A-FORM RNA

Introduction

Magnesium binding to A-form RNA

Magnesium binds RNA at specific coordination sites, or in non-specific binding pockets. The most studied RNA-bound Mg^{2+} ions are the ions responsible for tertiary folding, which bind in sites where phosphates are clustered (64). However, the electrostatic nature of the major groove of A-form RNA helices make them an attractive target for cation binding (Figure 38). The two anti-parallel ribose-phosphate backbones run close to each other and form a narrow entrance into the deep major grove. Calculations showed that the electrostatic potential in the deep major groove is the most negative of the RNA duplex charge distribution (76).

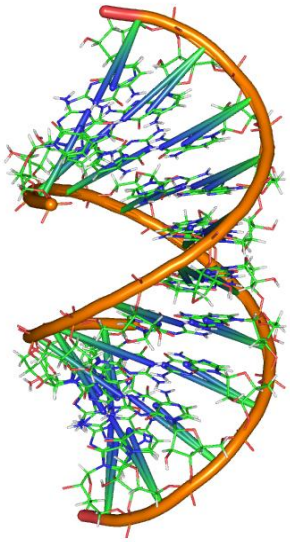

Figure 38. A-form structure of nucleic acids. A-form duplexes have a deep major groove (PDB 1QC0).

A crystallographic study used A-DNA to approximate A-form RNA, and observed characteristic binding modes of hexahydrated magnesium ($[Mg(H_2O)_6]^{2+}$) (64). These studies were consistent with earlier solution studies with NMR that used $[Co(NH_3)_6]^{3+}$ as a model of $[Mg(H_2O)_6]^{2+}$, and observed similar binding sites (77). An observed binding mode showed the ion bound in the deep major grove of a GpN step, contacting the O6/N7 sites of guanine bases via hydrogen bonds (64)(Figure 39). This preference for the Hoogsteen sites of G residues has been observed elsewhere (65). Another binding mode observed was the ion bound to the phosphates, bridging across the outer mouth of the narrow major groove (64).

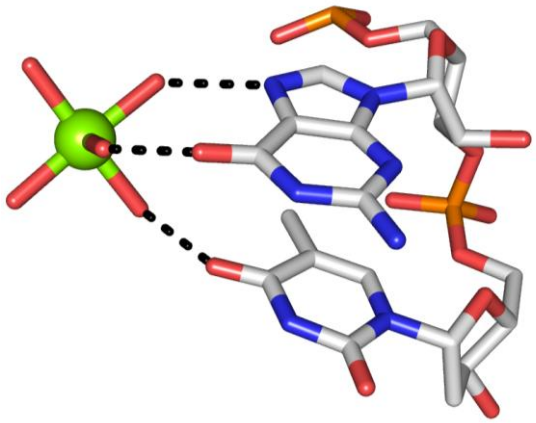

Figure 39. Detailed view of the detailed interactions between $[Mg(H_2O)_6]^{2+}$ ions and A-form nucleic acids (64). G forms two hydrogen bonds with $[Mg(H_2O)_6]^{2+}$ and O6/N7. PDB 1DNO.

P4-P6 folding with Mg^{2+} and/or Na^{+}

P4-P6 domain RNA has been widely studied as a model RNA for folding of other large RNA domains. P4-P6 is a domain of the *Tetrahymena* intron, that folds before the rest of the ribozyme (46). As an independently folding domain, it folds to the same native structure in the intron as it does when separate. A cluster of bound divalent metals within P4-P6 organize a three-helix junction that drives the folding of the RNA (and ultimately

the entire ribozyme) (15). P4-P6 folds to its native form with the addition of Mg^{2+}. However, RNA compaction studies on P4-P6 showed that P4-P6 also proceeds through a monovalent dependent equilibrium folding pathway. P4-P6 is in an extended conformation in low salt conditions, with double helical elements splayed away from one another (78) (Figure 40A). Upon increasing the concentration of Na^{+} (~100 mM), repulsive interactions between phosphates are screened allowing a structural relaxation of P4-P6 (Figure 40B). The addition of higher Na^{+} (~1 M) allows for the formation of long-range tertiary contacts, leading to even further compaction (Figure 40C). Experiments with mutants showed that only a tetraloop/tetraloop receptor long-range contact can form in the presence of high sodium concentration. Tertiary contacts mediated by coordination sites in the A-rich bulge of P4-P6 can only form in the presence of Mg^{2+} (Figure 40D). These and other studies illustrate that both monovalents and divalents play an important role in RNA native folding.

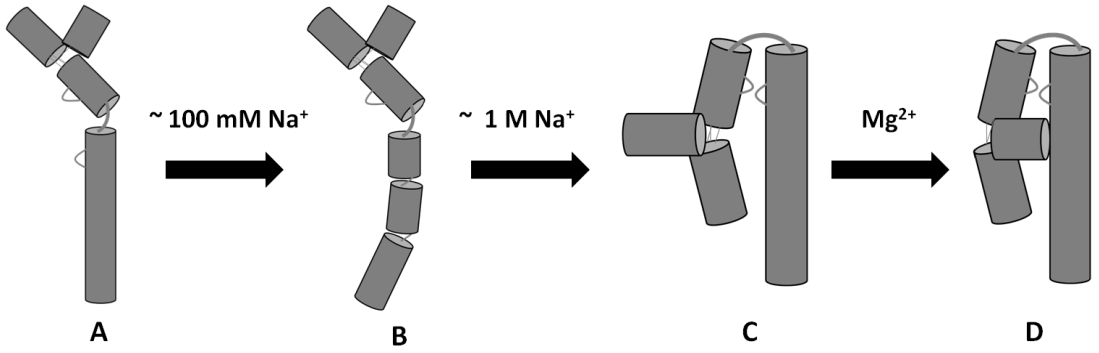

Figure 40. Folding pathway for P4-P6, modified and adapted from (78).

P4-P6 A186U mutant

The A186U mutation of P4-P6 was shown to disrupt tertiary folding of the RNA. Located in the A-rich bulge which is important for the metal ion core of P4-P6, A186 directly coordinates magnesium ions to mediate tertiary folding of P4-P6 to its native

structure (Figure 41)(47). A186 is also involved in hydrogen bonds with three different nucleotides in the When the A is mutated to a U, P4-P6 domain RNA does not fold even at high concentrations of Mg^{2+} (15). This mutant however has a similar extended form to wild type P4-P6 in low salt in the absence of Mg^{2+} and does not change the predicted secondary structure (79,80). Therefore this mutant has been widely used as an unfolding control to study Mg^{2+}-mediated folding of P4-P6 RNA (81-84).

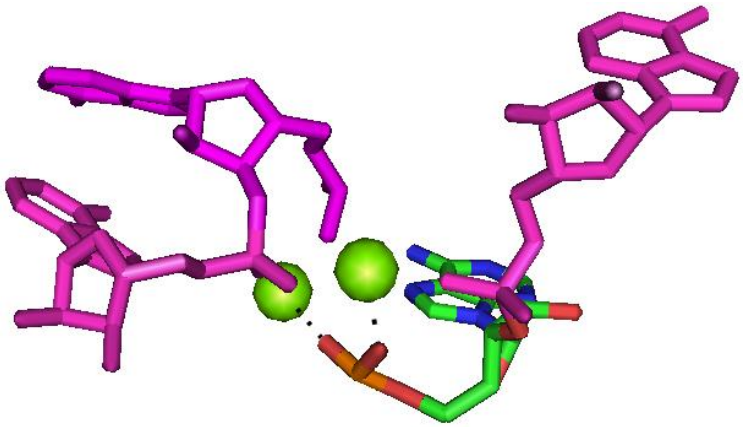

Figure 41. A186 residue (in color) of P4-P6 coordinates two Mg^{2+} ions responsible for P4-P6 tertiary structure (PDB 1GID).

Divalent metal chelators

Divalent metal chelators are molecules that bind divalent cations with high affinity, scavenging them from solution. Chelators were employed in this study to ensure that RNA samples were divalent cation-free, and for estimating the binding affinity of RNA for divalent metals. Four chelators are used in this study: ethylene-diamine tetraacetic acid (EDTA), diaminocyclohexane tetraacetic (DCTA), diethylenetriamine-*N,N,N',N',N*''-pentaacetic acid (DTPA) and *N*-(2-hydroxyethyl)ethylenediamine-*N,N',N'*-triacetic acid (HEDTA) (Figures 42-45). Of these, EDTA is the most common, often used in biological assays and seen as a component in buffers. The chelators used

here have been employed in many studies such as in spectrophotometric determination of metal concentrations (85), kinetic studies of isotopic exchange reactions between ions and their chelates (86), and in general for solution studies of rare earth metals (87,88).

EDTA

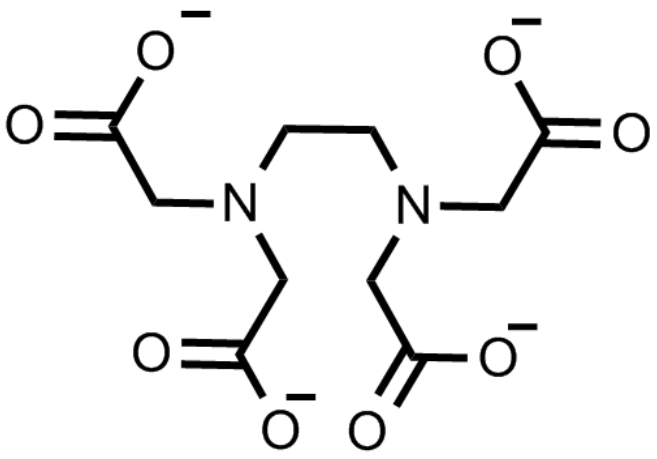

Figure 42. Ethylenediaminetetraacetic acid.

DCTA

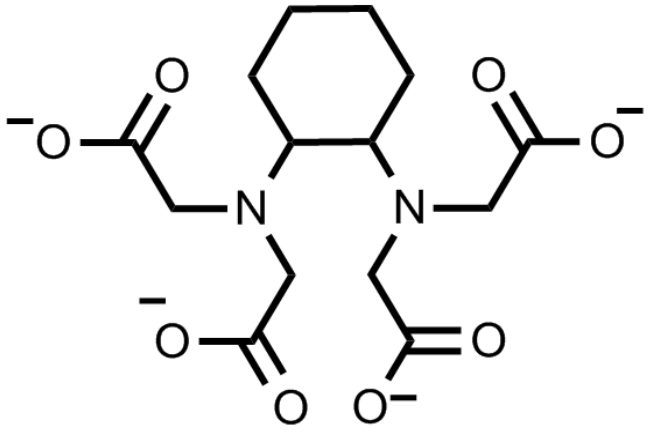

Figure 43. Diaminocyclohexane tetraacetic acid.

DTPA

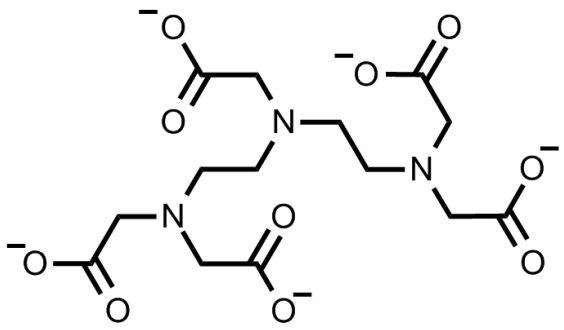

Figure 44. Diethylenetriamine- *N*, *N*, *N*’, *N*’, *N*’’-pentaacetic acid.

HEDTA

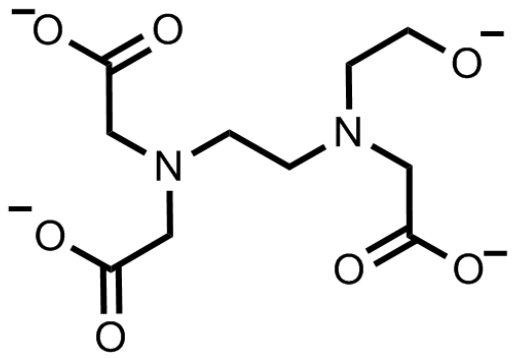

Figure 45. *N*-(2-Hydroxyethyl)ethylenediamine-*N*, *N*’, *N*’-triacetic acid.

Experimental Methods

Materials

Nuclease free water (IDT) was used in all experiments involving RNA. Sodium cacodylate buffer stock solution was prepared by dissolving sodium cacodylate (Sigma-Aldrich) in H_2O and titrating with HCl to pH 6.8. EDTA stock solution was prepared by

dissolving Na_2EDTA (J.T. Baker) in water and titrating with NaOH to pH 7. DCTA (Sigma-Aldrich, CAS# 13291-61-7), DTPA (Sigma-Aldirch, CAS# 67-43-6) and HEDTA (Sigma-Aldrich, CAS# 139-89-9) stock solutions were prepared similar to EDTA. $MgCl_2$ stock solution was prepared by dissolving magnesium chloride (Fisher, CAS# 7791-18-6) in H_2O. NaCl stock solution was prepared by dissolving sodium chloride salt (VWR) in H_2O.

RNA Synthesis and Purification

The gene for the Del C209 variant (18) and the A186U mutant (47) of the P4-P6 domain of the *T. thermophila* Group I intron was synthesized by recursive PCR (60). All genes were confirmed by sequencing. RNAs were synthesized by in vitro transcription (HiScribe T7 High Yield RNA Synthesis Kit, New England Biolabs). Plasmid template was removed by DNase digestion (TurboDNase, Ambion). DNase treated transcription reactions were directly precipitated by the addition of a one-tenth volume of 5 M ammonium acetate, pH 5.2, followed by 2.5 volumes of absolute ethanol. Pelleted precipitates were washed three times by vortexing in 80% ethanol in water, dried *in vacuo* and re-suspended in water. Aliquots (1 mL) of RNA (≤ 1 mg/mL in 10 mM TRIS, pH 8.0, containing 2 mM EDTA) were heated to 65 °C for 5 min, quick cooled on ice and applied to a G-25 size exclusion column (Illustra NAP-10, GE Healthcare Life Sciences) following the manufacturer's instructions. Elution was with water. RNA purity and integrity were assayed by visual inspection of the banding pattern resolved in gel after denaturing gel electrophoresis (SequaGel UreaGel System, National Diagnostics). Nucleic acid concentrations were determined by absorbance at 260 nm (Thermo

NanoDrop). Nuclease free water (HyPure Molecular Biology Grade Water, HyClone) was used in all experiments involving RNA. RNA duplex oligomers (5'-GGUGAGGCGGUG-3', 5'-GUUGAGUGAGUG-3' and 5'-CGCGUAUACGCG-3') were obtained from Dharmacon, Inc, purified by standard desalting.

Experimental Conditions

All experiments were performed in 5 mM sodium cacodylate buffer, pH 6.8 and at 20 °C (unless otherwise specified). RNA concentration was 176 μM (nucleotide) in all experiments, unless otherwise specified.

Experimental Techniques

Circular Dichroism (CD)

Circular Dichroism (CD) spectroscopy measures the difference in the absorption of right- and left-circularly polarized light. Chiral molecules, including biological macromolecules such as nucleic acids and proteins, exhibit CD signals. As such, CD spectroscopy is commonly employed in the study of these molecules. While it cannot provide atomic-level information on the large, complex macromolecules, it is useful for studying conformational features of the molecule overall.

Here, CD is used to monitor RNA conformation as metals or chelator molecules are added to the RNA sample. All CD experiments are performed on a Jasco J-710 CD spectrometer. The wavelength range 350 – 220 nm was scanned at a speed of 50 nm/min (4 scans averaged) or 100 nm/min (6 scans averaged). Experiments were performed at 20 °C

ESI mass spectrometry

Electrospray ionization (ESI) mass spectrometry is a powerful technique for molecules of various sizes and polarities in a biological sample. Mass spectrometry was performed on an Agilent 6130 series Quadrupole LC/MS system.

^{1}H NMR

Nuclear magnetic resonance (NMR) spectroscopy was used to identify and quantify the chelator-bound divalent cations. ^{1}H NMR was performed on a Bruker DRX-500 with 1024 scans.

Mathematical Modeling

The mathematical modeling software Mathematica (Wolfram) was used to create a Monte Carlo-based simulation to fit titration data from CD experiments. RNA-cation binding events were modeled using two-K_a models. A system of simultaneous equations was generated and solved numerically to obtain the [RNA-Mg^{2+}] (i.e. total concentration of cation-bound RNA). Estimates of binding constants ($K_{Mg\text{-}RNA}$, $K_{Mg\text{-}EDTA}$ etc) were used to generate titration curves. Monte Carlo methods were employed to obtain the binding constants that gave the best fit of the binding model to the experimental data. The Monte Carlo process was iterated until the RMSD of observed-to-calculated converged to a minimum. The final parameters were not dependent on the initial parameters of the fit.

Results

CD titrations with P4-P6

Magnesium and chelator titrations

To observe magnesium-induced structural transitions in P4-P6 RNA as monitored by CD, the RNA was first titrated with divalent metal chelators to ensure that no trace divalent metals were present in the RNA sample. The RNA and buffer concentrations were rigorously held fixed during the titration, so that all changes in CD signal could be attributed to addition of the chelator.

The CD spectrum of P4-P6 RNA shows a peak at 267 nm, typical of RNA structures. Titration of EDTA into the purified P4-P6 RNA sample caused small but systematic and reproducible changes in CD spectra (Figure 46, top row, left). Most apparent is the decreased intensity of the peak at 267 nm. The effect of adding EDTA wanes as EDTA concentration approaches 300 μM. After this concentration is reached,

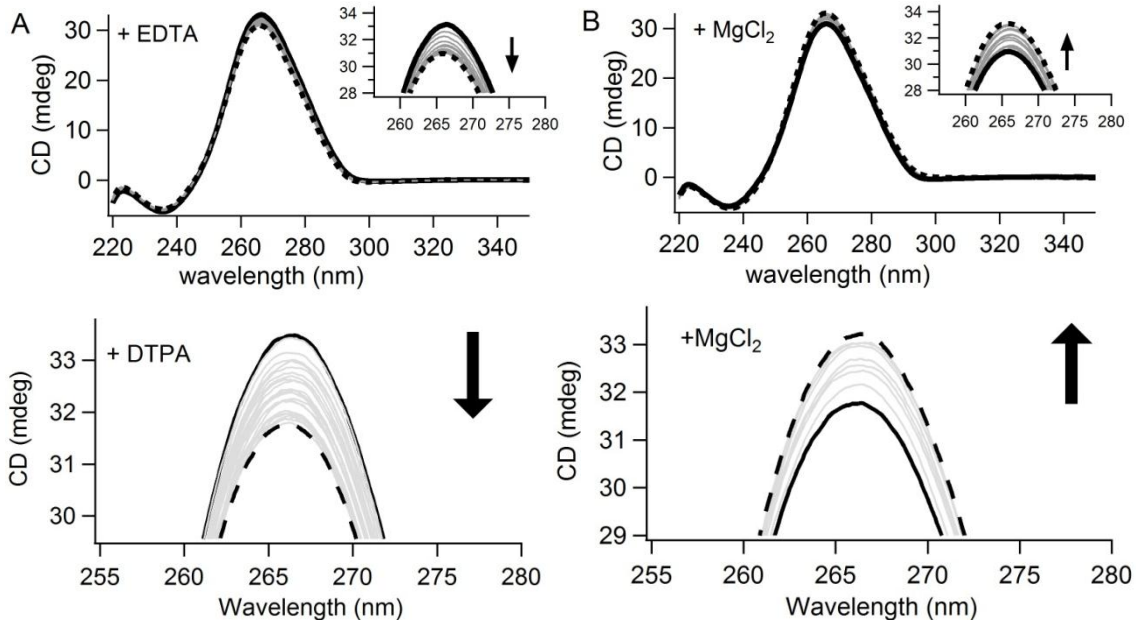

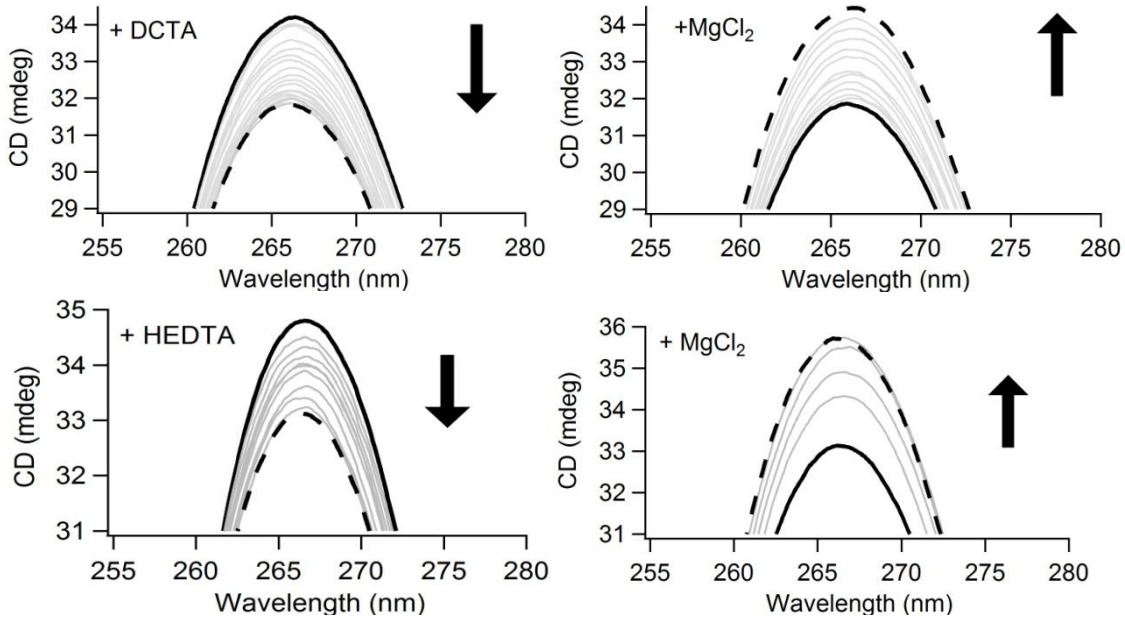

Figure 46. Chelator and $MgCl_2$ titrations into P4-P6 domain RNA. Top row: CD spectra over the course of EDTA titration from 0 to 600 μM (left), followed by titration of up to 600 μM $MgCl_2$ into the same sample (right). 2nd row: CD spectra of DTPA titration from 0 to 1200 μM (left), followed by titration of up to 800 μM $MgCl_2$ into the same sample (right). 3rd row: CD spectra of DCTA titration from 0 to 200 μM (left), followed by titration of up to 300 μM $MgCl_2$ into the same sample (right). Bottom row: CD spectra of HEDTA titration from 0 to 3000 μM (left), followed by titration of up to 1000 μM $MgCl_2$ into the same sample (right).

titration of $MgCl_2$ into the same RNA-EDTA sample reverses the observed changes in the CD spectrum (Figure 46, top row, right). The same result was observed when P4-P6 was titrated with other chelators DTPA, DCTA and HEDTA (Figure 46).

Difference spectra (i.e. subtraction of all spectra from the spectrum of the starting sample) revealed that as chelator was added, a negative peak at 270 nm was forming (Figure 47A). The same result was observed when P4-P6 was titrated with other chelators DTPA, DCTA and HEDTA (Figure 47). Difference spectra revealed that when $MgCl_2$ is titrated into the samples, a peak grows at 267 nm with a shoulder at 290 nm.

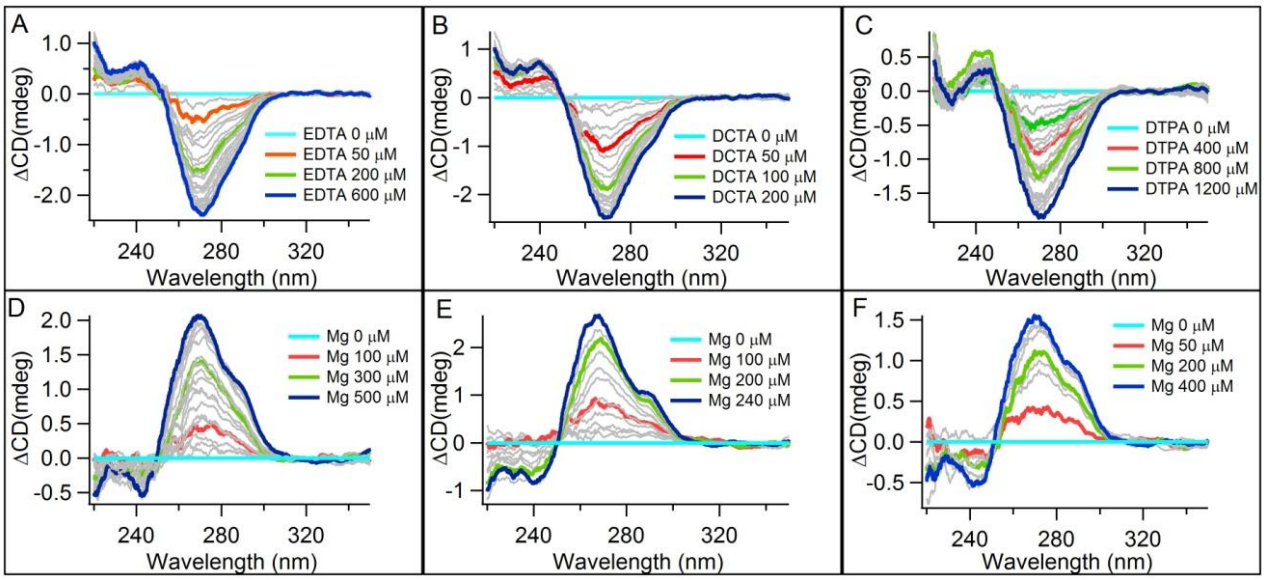

Figure 47. Difference spectra of chelator and $MgCl_2$ titrations from Figure 46. (A) & (D) EDTA and $MgCl_2$ titrations, (B) & (E), DCTA and $MgCl_2$ titrations, (C) & (F) DTPA and $MgCl_2$ titrations. HEDTA not shown.

With the addition of higher concentrations of Mg^{2+}, a transition is observed as the peak at 267 nm shifts to 258 nm and continues to grow. This peak appears to correspond to Mg^{2+}-induced tertiary folding of P4-P6 domain RNA (Figure 48).

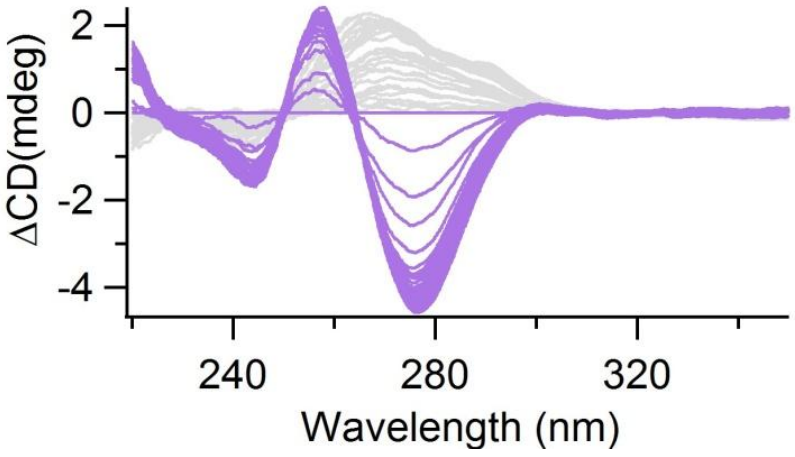

Figure 48. Multiple transitions observed as $MgCl_2$ is titrated into P4-P6 domain RNA. Grey spectra are 0 to 650 μM $MgCl_2$, purple spectra are 650 μM to 10 mM $MgCl_2$.

Comparison of chelators

Quantitative differences in the effects of chelators correlate well with the known differences in the affinities of the chelators for divalent cations. For DCTA, the strongest of the three chelators, < 200 μM of chelator was sufficient to achieve maximal change in CD signal. In contrast, > 1200 μM of DTPA, the weakest of the three chelators, is needed to achieve maximal change in CD signal (Figure 49).

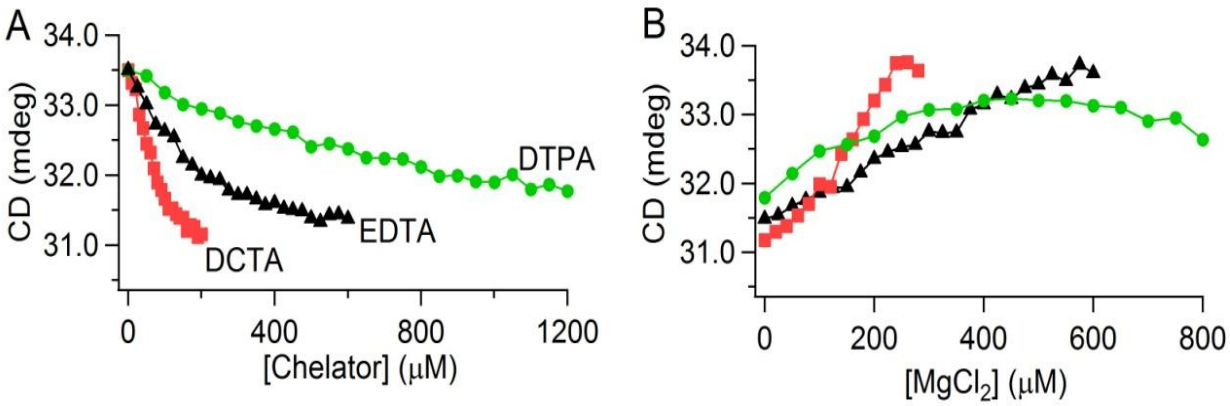

Figure 49. Plots of CD signal intensity at 266 nm for P4-P6 RNA versus (A) chelator concentration and (B) $MgCl_2$ concentration. The samples used for the $MgCl_2$ titrations in (B) are the samples from the final chelator titration points shown in (A).

P4-P6 titrations with sodium

NaCl was titrated into P4-P6 domain RNA, following the addition of 600 μM EDTA. Four structural signatures with subtle differences between them are observed in the difference spectra (Figure 50, top). The initial state of P4-P6 domain RNA persists to 1 mM sodium (Figure 50, bottom). The second regime (Figure 50, orange traces) show a positive peak at 262 nm with negative peaks at 285 nm and 229 nm. The third regime

(grey traces) show a transition from the peak at 262 nm to 258 nm, and negative peaks move to 278 nm and 233 nm respectively. The last regime (blue peaks) displays a peak at 260 nm with a negative peak at 235 nm.

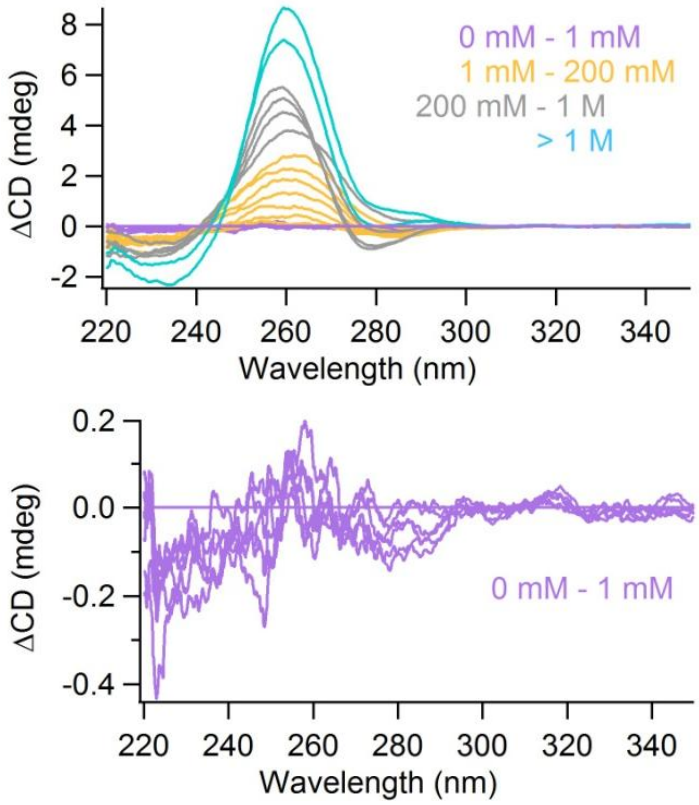

Figure 50. Difference spectra of NaCl titration into P4-P6. (A) Four structural CD signatures are observed as 0 to 1 M NaCl is added. (B) The first structural CD signature is expanded, showing that there is little structural variation in P4-P6 between 0 and 1 mM NaCl.

CD titration of P4-P6 from extended to native structure

As NaCl is added to P4-P6 RNA, the RNA becomes increasingly folded (Figure 40). CD signatures of the different states sampled are shown above (Figure 50). To investigate the effect of starting structure on the Mg^{2+}-folding pathway, three pathways were explored using three different starting conformations of P4-P6: I) The unfolded,

Na^+-helical form of P4-P6 in low-salt; II) an electrostatically-relaxed conformation of P4-P6, induced by the addition of 100 mM NaCl; and III) a compact P4-P6 conformation, induced by the addition of 2M NaCl. Mg^{2+} was added to fold all three structures to the native state, as conformational changes were monitored by CD. The observed structural changes for the three folding pathways are summarized in Table 1. Increase in peaks at 270 and 290 nm correspond to a conversion from Na^+-helical to Mg^{2+}-helical form of P4-P6. Peaks shift to different wavelengths (from 270 to 258 nm, and 290 to 297 nm) corresponds to P4-P6 conformational change from extended to compact form. Finally, increase in peaks at 258 and 297 nm, and decrease in peaks at 277 nm and 244 nm correspond to formation of P4-P6 native structure.

Table 1.3 Mg^{2+}-folding pathways of P4-P6 observed by CD. Observed CD signals for each pathway are indicated. Up arrows indicate increase in the peak, down arrows indicate decrease in peak, left arrows indicate peak transition between wavelengths, × indicates signal not observed and ✓ indicates observed signal for the RNA sample

	Na-helical to Mg-helical form	RNA compaction	Native structure formation
CD signal change	270 nm ↑ 290 nm ↑	270 → 258 nm 290 → 297 nm	258 nm, 297 nm ↑ 277 nm, 244 nm ↓
Low Na^+ form	✓	✓	✓
100 mM Na^+ form	×	✓	✓
2M Na^+ form	×	×	✓
A186U mutant	✓	×	×

Unfolded, Na^+-helical P4-P6 folded with Mg^{2+}

Upon adding Mg^{2+} to the unfolded, Na^+-helical P4-P6 in 5 mM sodium cacodylate buffer, we first observe the formation of the Mg^{2+}-helix, evidenced by a peak at 270 nm and shoulder at 290 nm. This conformational change is followed by a transition between

350 μM and 750 μM Mg^{2+} where the peak at 270 nm shifts to 258 nm and the shoulder at 290 shifts to 297 nm. Higher concentrations of Mg^{2+} lead to an increase of both peaks at 258 nm and 297 nm, along with a decrease in peaks at 277 nm and 244 nm (Figure 51). This structural change corresponds to native structure formation.

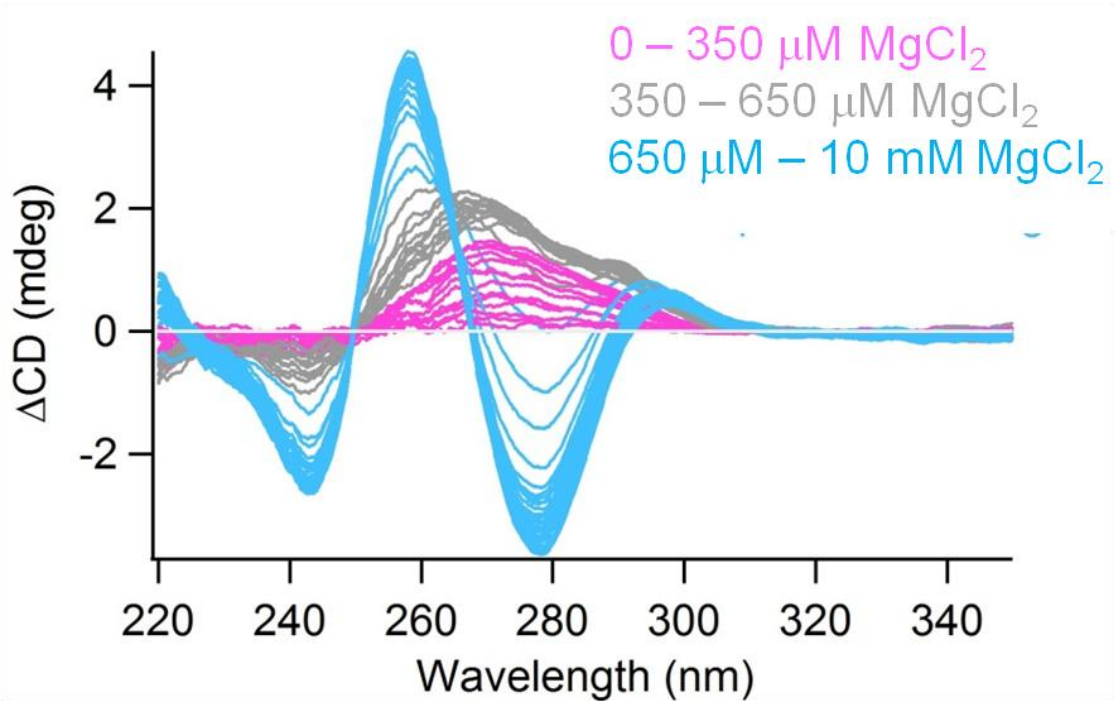

Figure 51. Mg^{2+} folding pathway of P4-P6, starting with unfolded, Na^{+}-helical conformation.

P4-P6 with 100 mM NaCl, folded with Mg^{2+}

The intermediate structure of P4-P6 in P4-P6 is electrostatically relaxed, as reported (78), and shown in Figure 40. Our CD data agrees with previous reports, as we observe a transition consistent with a collapse of extended P4-P6 RNA (Table 1). We then observe peak changes corresponding to native structure formation (Figure 52).

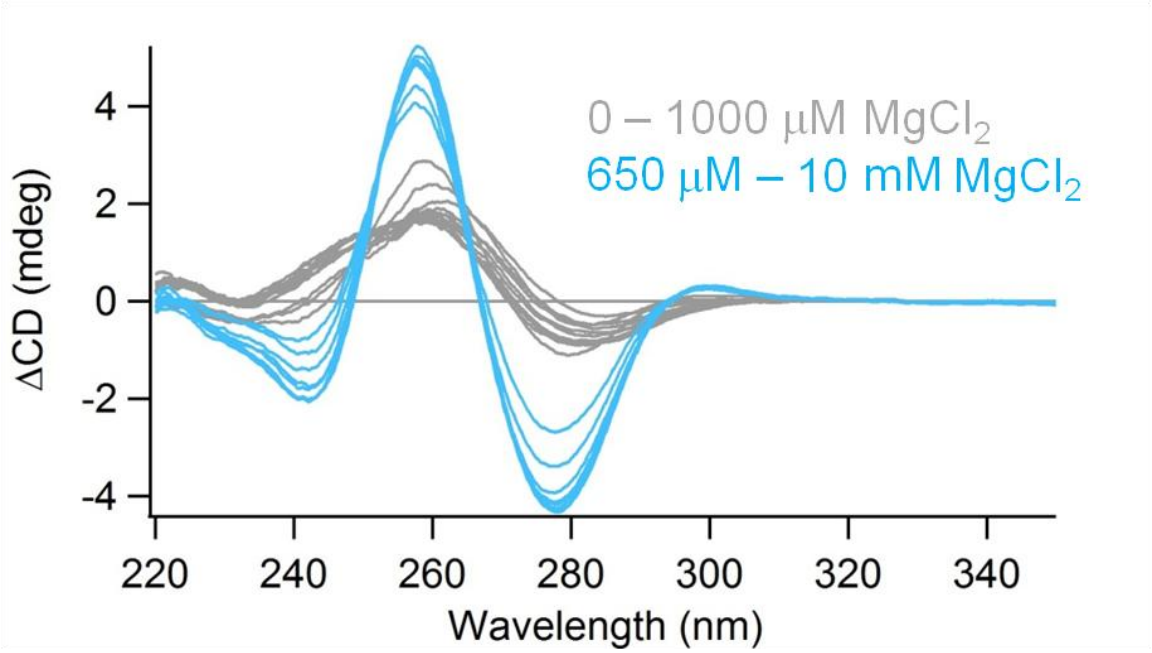

Figure 52. Mg^{2+} folding pathway of P4-P6, starting with electrostatically relaxed conformation in 100 mM NaCl.

P4-P6 with 2M NaCl, folded with Mg^{2+}

In 2M NaCl, P4-P6 is compact with tertiary interactions formed except for the Mg^{2+}-coordination interaction. The changes we observe upon Mg^{2+} titration correspond to formation of the P4-P6 native structure (Table 1). 2M NaCl conditions are have typically been used in RNA folding experiments to saturate the ion atmosphere with monovalent ions, so that specific binding effects of divalent cations can be isolated. Our CD data is consistent with previous data showing that under these high salt conditions, P4-P6 undergoes only one transition to the native state (Figure 53).

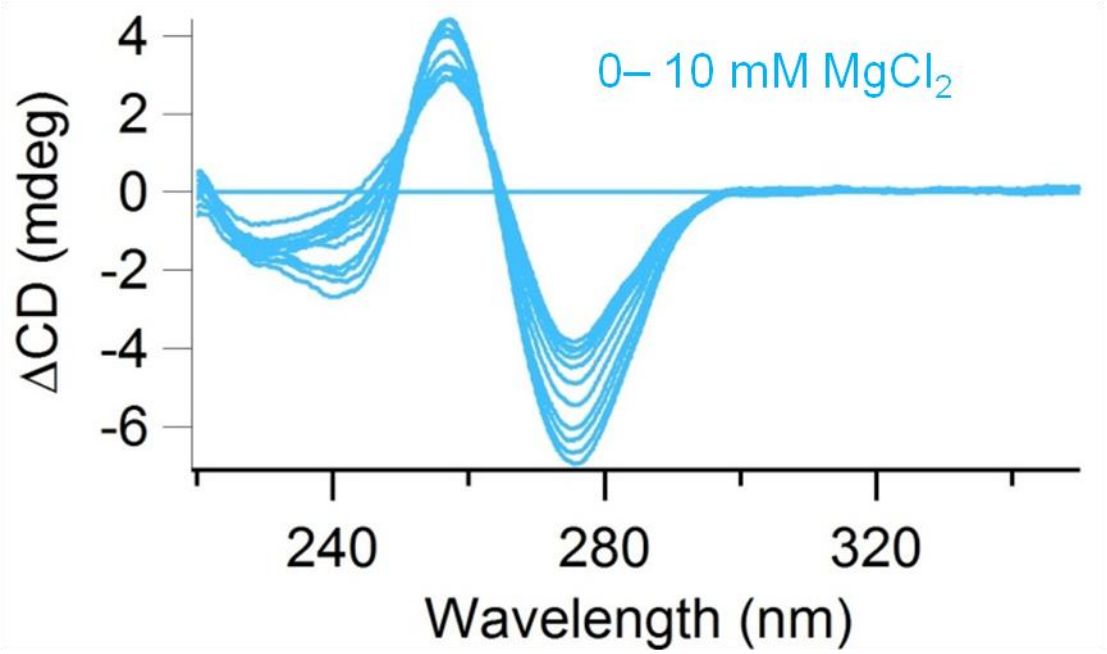

Figure 53. Mg^{2+} folding pathway of P4-P6, starting with compact P4-P6 conformation in 2M NaCl.

CD titrations of A186U P4-P6 mutant

Mg^{2+} is titrated into A186U P4-P6 mutant RNA. The peak at 267 nm with the shoulder at 290 nm is observed, consistent with Mg^{2+} binding to unfolded P4-P6 RNA (Figure 54). This peak saturates at 1200 μM $MgCl_2$, with further addition of $MgCl_2$ producing no change in the spectrum. No further transitions corresponding to Mg^{2+}-induced tertiary folding are observed. A small (~2 nm) shift to the right of the peak at 268 nm may correspond to an electrostatically driven, non-specific collapse of P4-P6 A816U that involves no tertiary contacts (82).

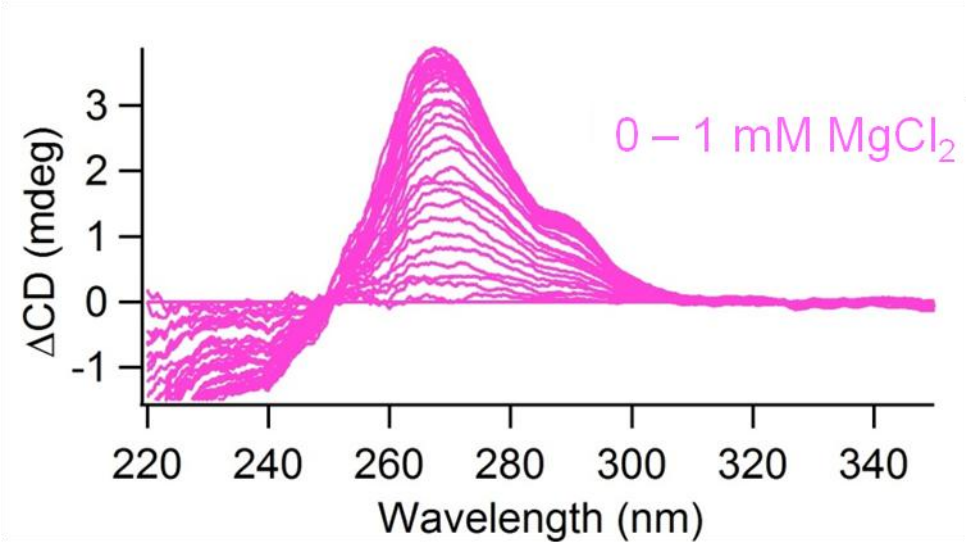

Figure 54. Mg^{2+} folding pathway of A186U P4-P6 mutant.

CD titrations with A-form RNA duplexes

Experiments were performed with three generic RNA duplexes to monitor structural changes induced by ion-binding to A-form RNA helices.

Magnesium and sodium titrations

In a background of 5 mM sodium cacodylate buffer, Mg^{2+} and Na^{+} were titrated separately into samples of the RNA duplexes. With all titrations, RNA and buffer concentrations were held rigorously fixed, so that all changes in CD signal can be attributed to addition of the metal ion salt. As [Mg^{2+}] and [Na^{+}] were increased respectively, changes were observed in the CD spectra. Difference spectra reveal increases and decreases at specific wavelengths (Figure 55). Table 2 summarizes the observed changes for the three duplexes. It is observed that A-form duplex RNA is in different conformational states depending on the concentration cations in the sample. It was also observed that there is a difference between the Mg^{2+} and Na^{+} forms of an A-

form duplex, and also, ion effects on A-form RNA are sequence specific, with different effects observed for different sequences.

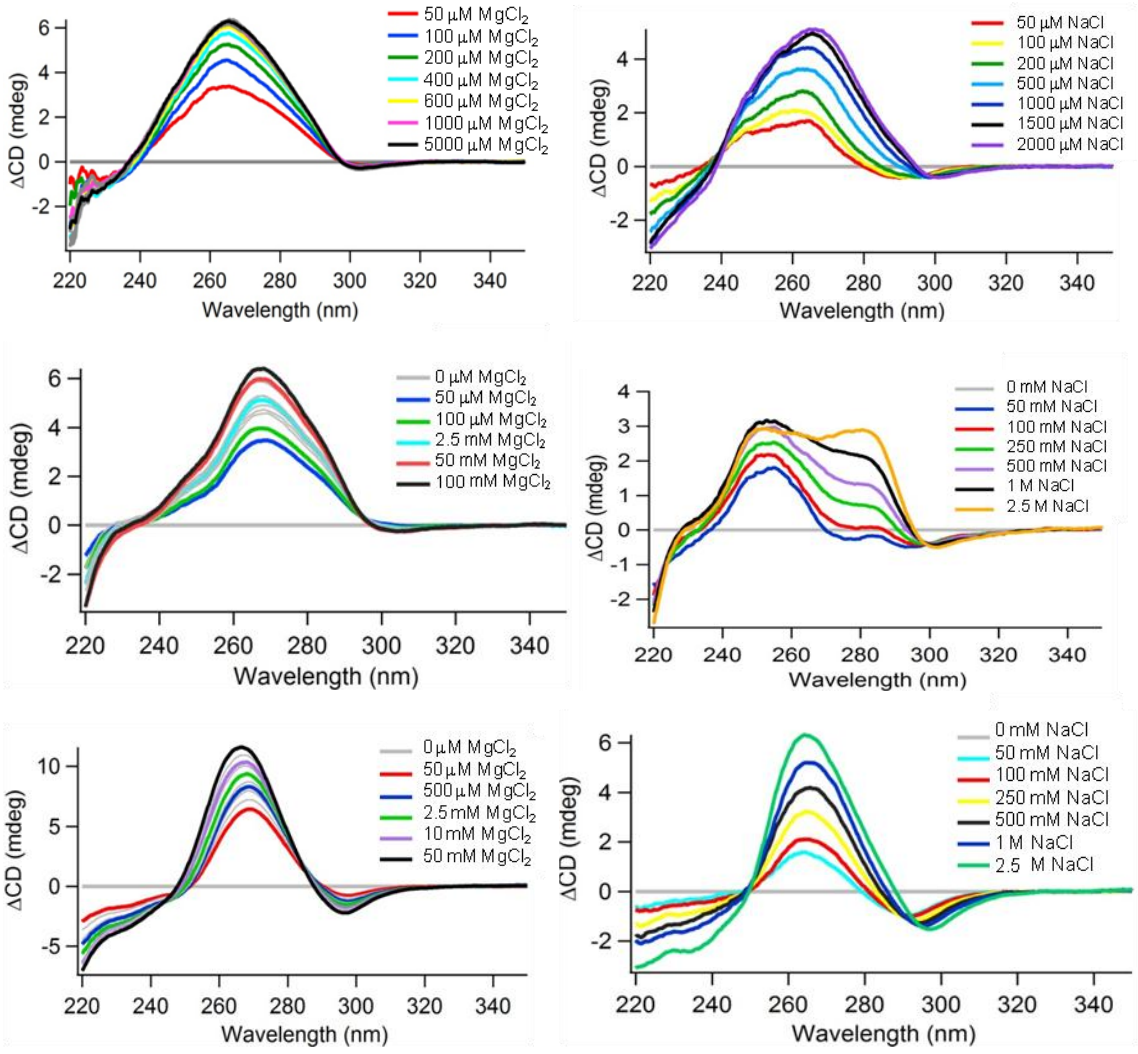

Figure 55. $MgCl_2$ and NaCl titrations of A-form RNA duplexes. Top row: D1 Duplex, 5'-GGUGAGGCGGUG-3'. Middle row: D2 Duplex, 5'-GUUGAGUGAGUG-3'. Bottom row: D3 Duplex, 5'-CGCGUAUACGCG-3'.

Table 2. Observed CD characteristics for $MgCl_2$ and NaCl titrations into RNA duplexes. * indicates shoulder peak.

		Mg titration		Na titration	
		Positive peaks	Negative Peaks	Positive peaks	Negative Peaks
D1	5’-GGUGAGGCGGUG-3’	265 nm		265, 247*	
D2	5’-GUUGAGUGAGUG-3’	268 nm		253, 284	
D2	5’-CGCGUAUACGCG-3'	268 nm	296 nm	265 nm	291-297 nm

A CD melting experiment was performed on duplex D1 with 250 mM NaCl added to the RNA sample, in the background of 5 mM sodium cacodylate buffer. Difference spectra of the cooling experiment from 95° C (Figure 56, red trace) to 5 °C (blue trace) were obtained. Increases in the magnitude of a peak at 265 nm and shoulder at 247 nm were observed, as the temperature was lowered from 95°C to 5 °C. These are the same peak changes that were seen as sodium was continually added to D1 (Table 2). Therefore the melting experiment suggests that the observed changes in CD signal upon NaCl titrations are consistent with an increase in the double-stranded form of D1, i.e. an increase in stability.

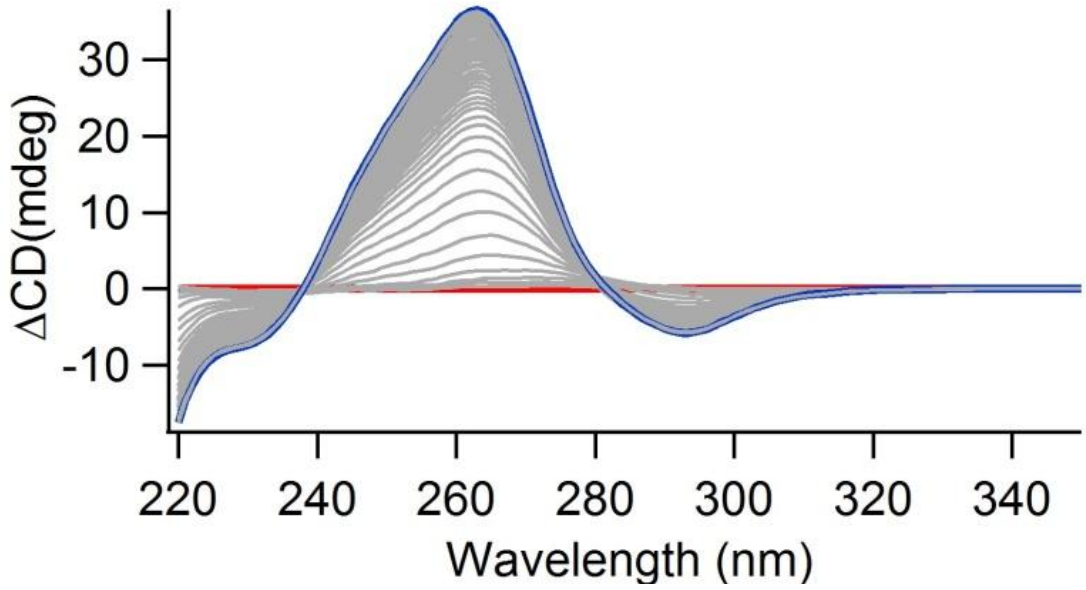

Figure 56. CD melt of duplex D1. Cooling experiment goes from 95 °C (red line) to 5 °C (blue line).

We can observe a transition between both forms of the RNA duplex as we titrate NaCl into an A-form RNA sample (D2) that contains 5 mM Mg^{2+}. The difference spectrum of the Mg^{2+} sample shows the peak at 265 nm, corresponding to the Mg^{2+} form of D2 (Figure 57). As NaCl and DCTA chelator are added, the transition observed is a decrease in the peak at 265 nm and a corresponding increase at ~252 and 285 nm respectively (Table 2). These changes correspond to a decrease in the Mg^{2+} form of the duplex, with an increase in the Na_{+} form.

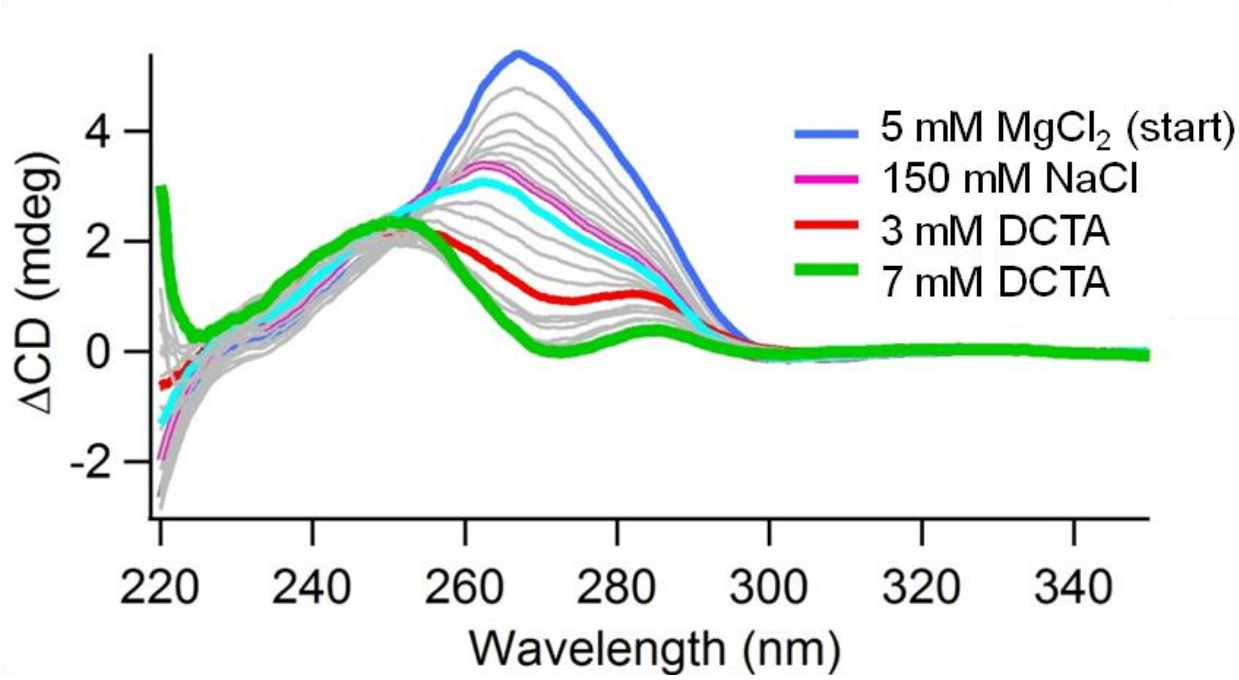

Figure 57. Transition from Mg^{2+}-form to Na^{+}-form of duplex D2

EDTA and magnesium and titrations

EDTA was titrated into duplex D1. Similar to P4-P6, a decrease in the peak magnitude at 263 nm is observed with increasing [EDTA]. The addition of Mg^{2+} leads to a reversal of the observed changes (Figure 59).

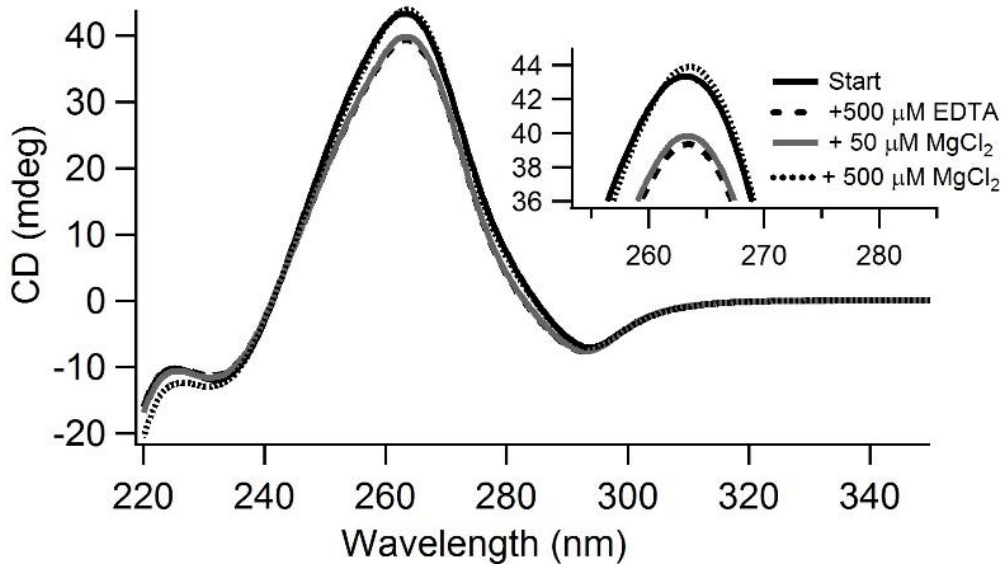

Figure 58. CD spectra of RNA duplex D1 over the course of titrations with EDTA and $MgCl_2$. Individual spectra shown are: before any additions (Start), after 500 μM EDTA had been added (+500 μM EDTA), after 50 μM $MgCl_2$ was added to the +500 μM EDTA sample (+50 μM $MgCl_2$), and after $MgCl_2$ was added to a total concentration of 500 μM (+500 μM $MgCl_2$).

Difference spectra of the EDTA titration into duplex RNA shows two peaks decreasing at 260 nm and 275 nm (Figure 59, top). Difference spectra of the Mg^{2+} titration show a peak increase at 264 nm (Figure 59, bottom).

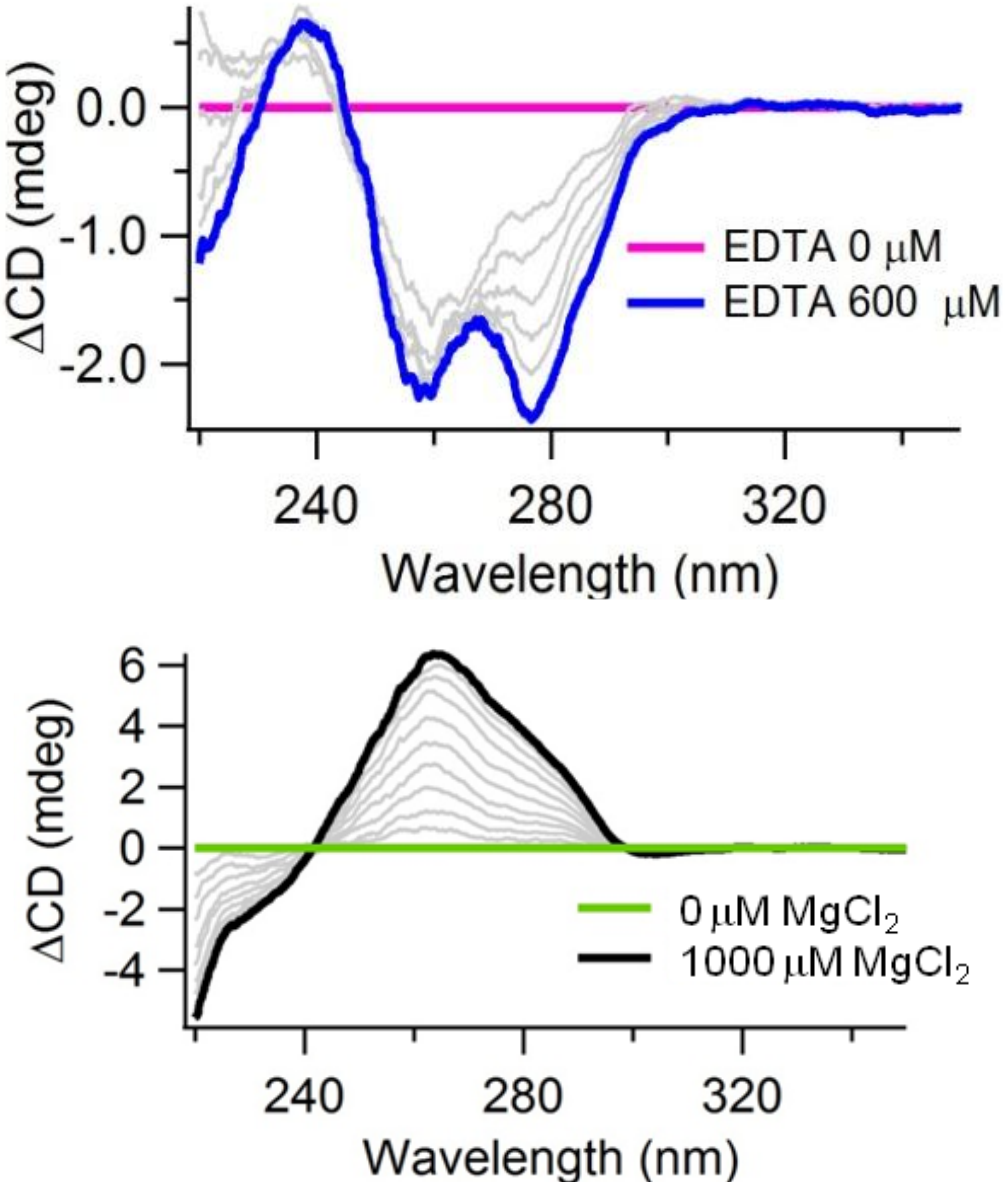

Figure 59. Difference spectra of EDTA (top) and Mg^{2+}(bottom) titrations into RNA duplex D1.

ESI-Mass spectrometry

The observation of a change in CD signal upon the addition of divalent cation chelators suggested that there were residual divalent cations in the purified RNA sample. ESI-MS was used to identify the residual divalent cations. ESI-MS on RNA samples containing EDTA indicated the presence of Mg^{2+} and Ca^{2+} in the purified P4-P6 RNA solutions (Figure 60). Three masses revealed were 291.1, 313.1 and 329 Daltons, corresponding to masses of free EDTA, EDTA-Mg^{2+} and EDTA-Ca^{2+}, respectively (all with -1 charge). Observed peaks corresponding only to Ca^{2+}-chelator and Mg^{2+}-chelator complexes allowed other possibilities such as Mn^{2+} or Zn^{2+} to be ruled out.

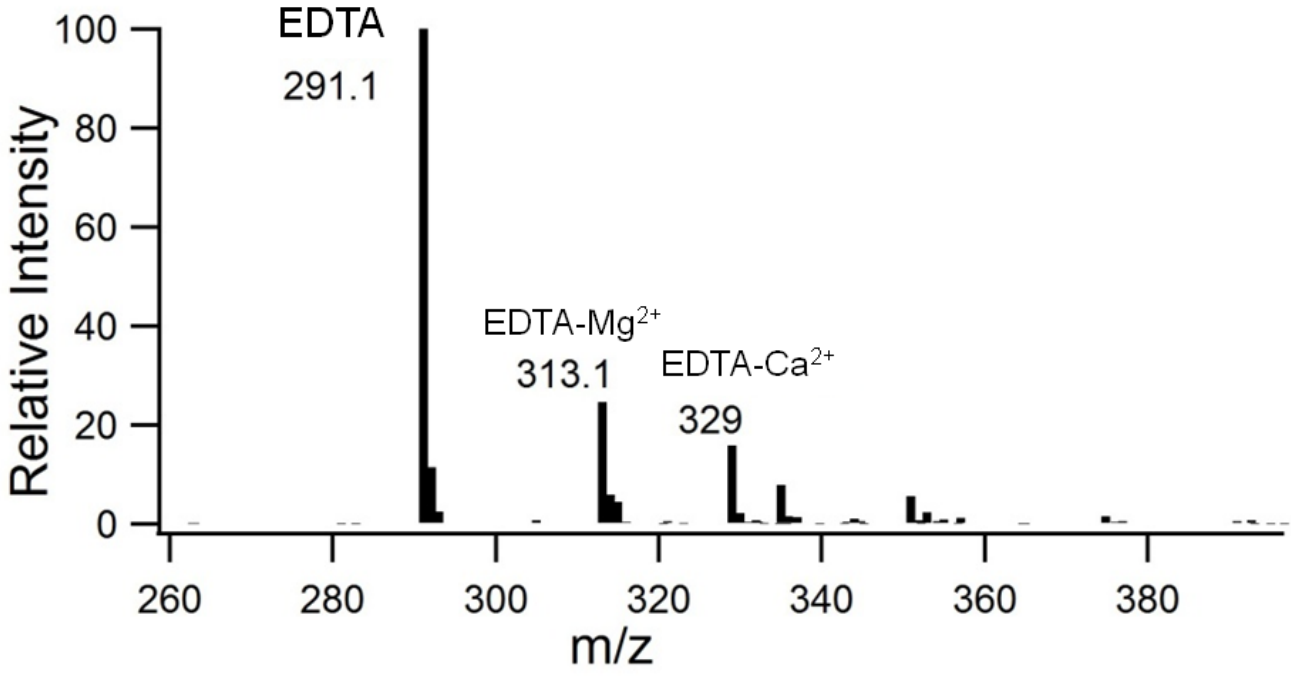

Figure 60. Mass spectrum of P4-P6 in buffer with added EDTA (600 μM), monitored in negative mode.

^{1}H NMR

Identification and quantification of residual divalent ions

^{1}H NMR was used to unambiguously resolve the identity and concentration of the dominant divalent cation associated with the RNA. The ^{1}H NMR spectra clearly differentiate free DCTA, Mg^{2+}-DCTA and Ca^{2+}-DCTA (Figure 61). Authentic samples reveal a resonance at 2.27 ppm for Mg^{2+}-DCTA, while Ca^{2+}-DCTA gives a resonance at 2.31 ppm. When DCTA is added to the purified P4-P6 RNA, the 2.27 ppm resonance of Mg^{2+}-DCTA is apparent. It is possible that a minor amount of Ca^{2+} is present in the sample, but the concentration of Ca^{2+} is less than 10% compared to Mg^{2+}. Thus, these results indicate that purified P4-P6 RNA contains residual Mg^{2+}.

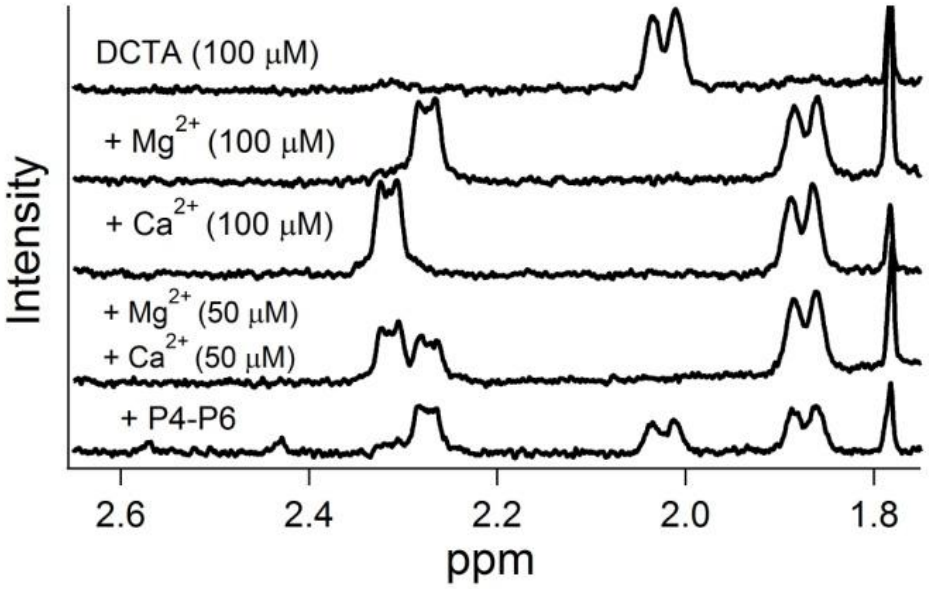

Figure 61. ^{1}H NMR spectra of free DCTA and DCTA with chelated metal ions. All samples contain 100 μM DCTA, with no added cations (top), with added $MgCl_2$ and/or $CaCl_2$, or with 1.1 μM of purified P4-P6 RNA.

^{1}H NMR was also used to quantitate the concentration of residual Mg^{2+} in the P4-P6 RNA samples. At saturating DCTA, [DCTA-Mg^{2+}] = [Mg^{2+}_{total}]. Therefore, by integrating the Mg^{2+}-DCTA resonance at 2.27 ppm obtained in various amounts of free and bound DCTA, a calibration curve was obtained that enabled a measurement of the total concentration of Mg^{2+} in the purified sample of P4-P6 RNA (Figure 62). This method revealed that our NMR sample of purified RNA at a concentration of 1.1 μM (in strand) contained ~80 μM Mg^{2+}.

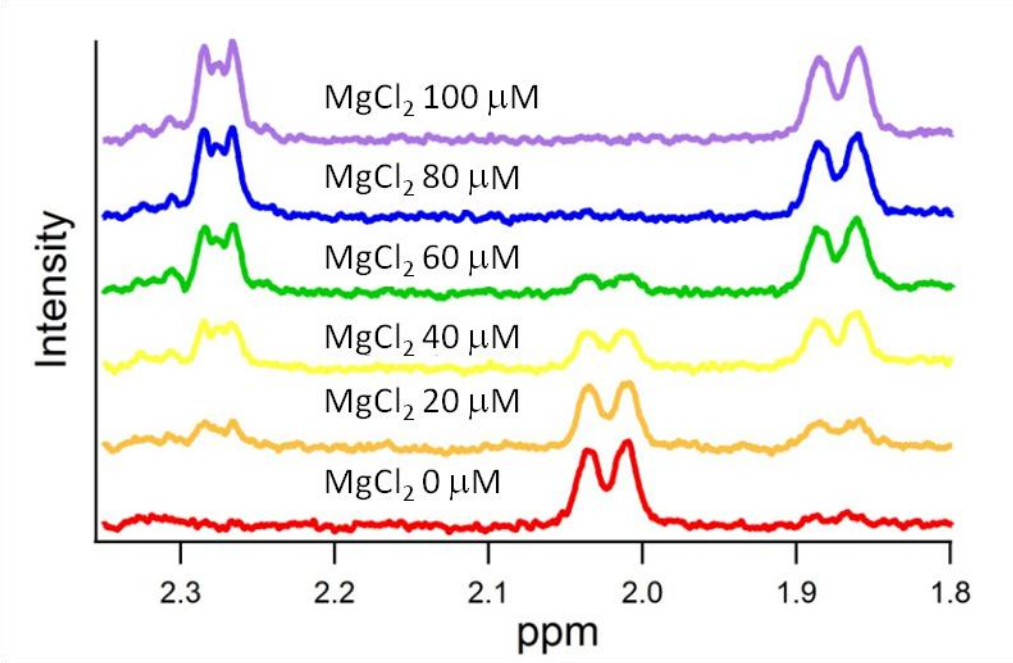

Figure 62. ^{1}H NMR spectra of DCTA with varying concentrations of chelated Mg^{2+}.

Discussion

Cation-dependent polymorphism in A-form RNA

Previous work investigating cation binding to A-form RNA in silico or in solution has focused on understanding cation distributions in the ionic cloud surrounding the RNA

(89). This work, computational and experimental, has been useful for identifying preferred binding sites for ions of different valences, and showing that polyvalent ions tend to be closer to the RNA than monovalent ions (89). Little work has been done to investigate the effect of monovalent and divalent cations on conformation of A-form RNA in solution.

Our CD data reveals subtle changes in RNA structure, as the identity and concentrations of the cations in solution are changed. Similar studies performed on DNA using circular dichroism have revealed the same effect (90-92). Ivanov speculated in his findings (91) that the differences observed in CD spectra reflect differences in DNA helical structure in solution. We believe that our results also reflect differences in helical structure of RNA under these different conformations. From our CD melting experiments, we see that higher concentrations of cation pushes the RNA towards a more stable form, with more double-stranded RNA present. Lower cation concentrations correlate with an RNA sample that possesses less double-stranded form.

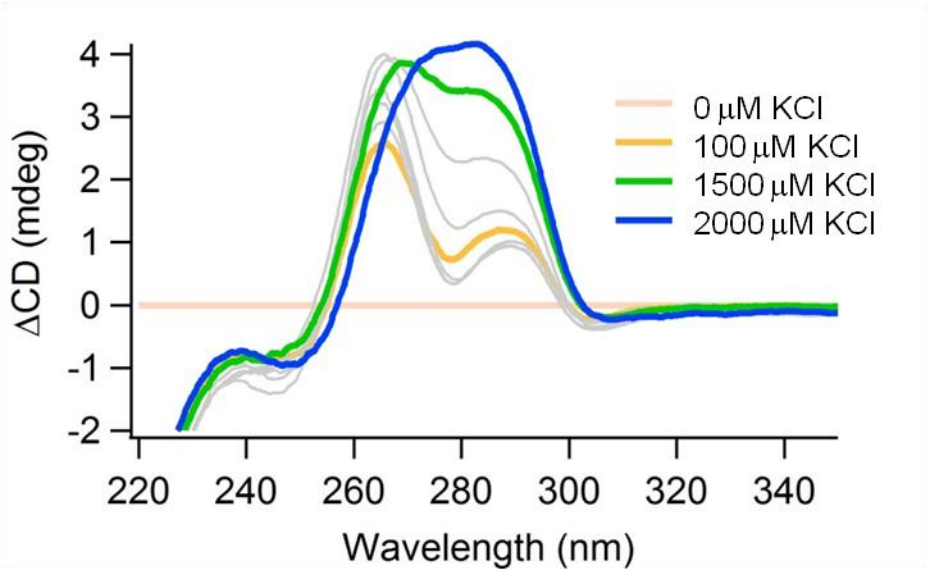

Figure 63. Potassium titration of A-form RNA duplex D1, 5'-GGUGAGGCGGUG-3'.

.

The dominant structure of A-form RNA in solution is different depending on the cationic species surrounding the RNA duplex. Indeed, a potassium titration in duplex D1 revealed *yet a different* conformation from the Na^+- and Mg^{2+}-forms (Figure 66). A-RNA appears to be able to adopt multiple forms with subtle helical differences between them. For instance, an A' conformation of RNA has been identified previously (93). A'-RNA differs from A-RNA in an increased number of nucleotides per turn. 12 base-pairs per turn in A'-RNA gives rise to a pitch height of 36 Å and an axial rise of 3.0 Å (93). Otherwise, nucleotide conformations are similar between A and A' RNA. It is possible that the polymorphism in our experiments could correspond to transitions between RNA conformations other than A-RNA. Further work will be needed to explore CD signatures of alternative RNA conformations.

We show that the effects are sequence-dependent, with different RNA duplexes showing unique changes. This result is consistent with previously observed preferences in Mg^{2+} for binding to guanine residues. The presence of more G residues in an RNA duplex could create more Mg^{2+} binding sites, impacting the observed conformation differently than a duplex with fewer G residues. We also observe that the Mg^{2+}- and Na^+-form of duplex D3 look similar to each other, more similar than was observed with the other duplexes (Figure 56, bottom row). This could imply that Mg^{2+} and Na^+ induce similar structures in this duplex and not in the others.

Sodium vs Magnesium form of unfolded, large RNA

In low salt conditions, P4-P6 is in an extended form with extensive helical regions. Titrating divalent chelators into P4-P6 RNA in low salt (5 mM sodium cacodylate buffer) removed all the trace divalent metals present in solution, revealing a

distinct structural form of the unfolded P4-P6 (Unfolded, helical Na^{+}-P4-P6). We observed that adding small concentrations of Mg^{2+} to this form returned it to a different conformation, i.e unfolded, helical Mg^{2+}-P4-P6.This finding is consistent with the results from our duplex experiments, showing a distinction between the Mg^{2+}-form and Na^{+}-form of A-RNA.

We observe that the folding pathway of P4-P6 is determined by the starting RNA conformation, which largely depends on the cationic composition, as observed in our studies. In low salt, transitions between helical forms of unfolded P4-P6 are observed that are not seen in the presence of higher salt. Previous folding studies on P4-P6 have focused largely on tertiary transitions (81,94,95) that induce large conformational changes in the RNA. We demonstrate the extraordinary sensitivity of CD by revealing subtle helical changes that result from ion binding.

These observations suggest a somewhat revised picture of cation binding to large RNAs in low salt conditions. Figure 64 illustrates a model for Mg^{2+}-mediated folding of P4-P6 in low salt conditions. This revised model shows that Mg^{2+} ions added to P4-P6 in a low-salt buffer up to a concentration of around 100 μM will interact strongly with double-stranded regions of P4-P6, converting the RNA to a distinct intermediate state with Mg^{2+} neutralizing phosphate charges along the RNA but not causing a collapse in the extended RNA or forming the native state. Further addition of Mg^{2+} will cause the RNA in an extended, helical form to collapse into a folded state that differs from the native state by not adopting the structural element that requires Mg^{2+} binding to the central core of the RNA. The addition of about 1 mM Mg^{2+} allows adoption of the native structure.

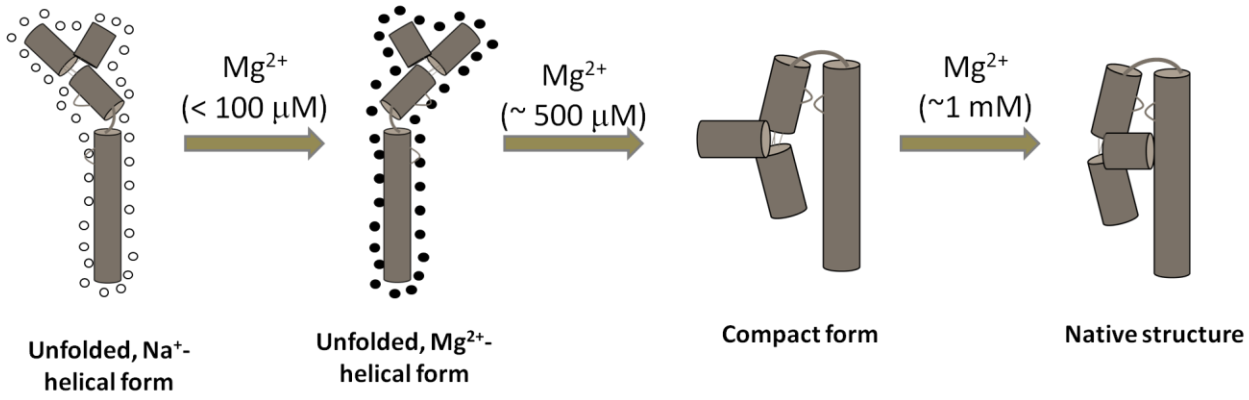

Figure 64. Revised models of P4-P6 association with monovalent and divalent cations during folding

Our revised model is informed by the observations from our CD experiments, and is consistent with results seen investigating RNA duplexes. One might ask why distinct Mg^{2+}- and Na^{+}-forms of unfolded P4-P6 were not detected in previous experiments conducted with P4-P6 RNA in low salt condition (46,95-97). We propose that previous investigative methods, including hydroxyl radical cleavage and gel mobility assays, monitor RNA folding processes that produce relatively large changes in the RNA conformation. The transitions observed in our work are very subtle, apparently corresponding to minor changes in helical structure, and would not be observed by the aforementioned methods.

The implications of our observations for folding P4-P6 RNA in low salt versus high salt conditions are illustrated in Figure 65. We propose that the association of the P4-P6 RNA helical regions with monovalent versus divalent cations induces a Na^{+}-form or Mg^{2+}-form of the helices that persists in the fully folded structure.

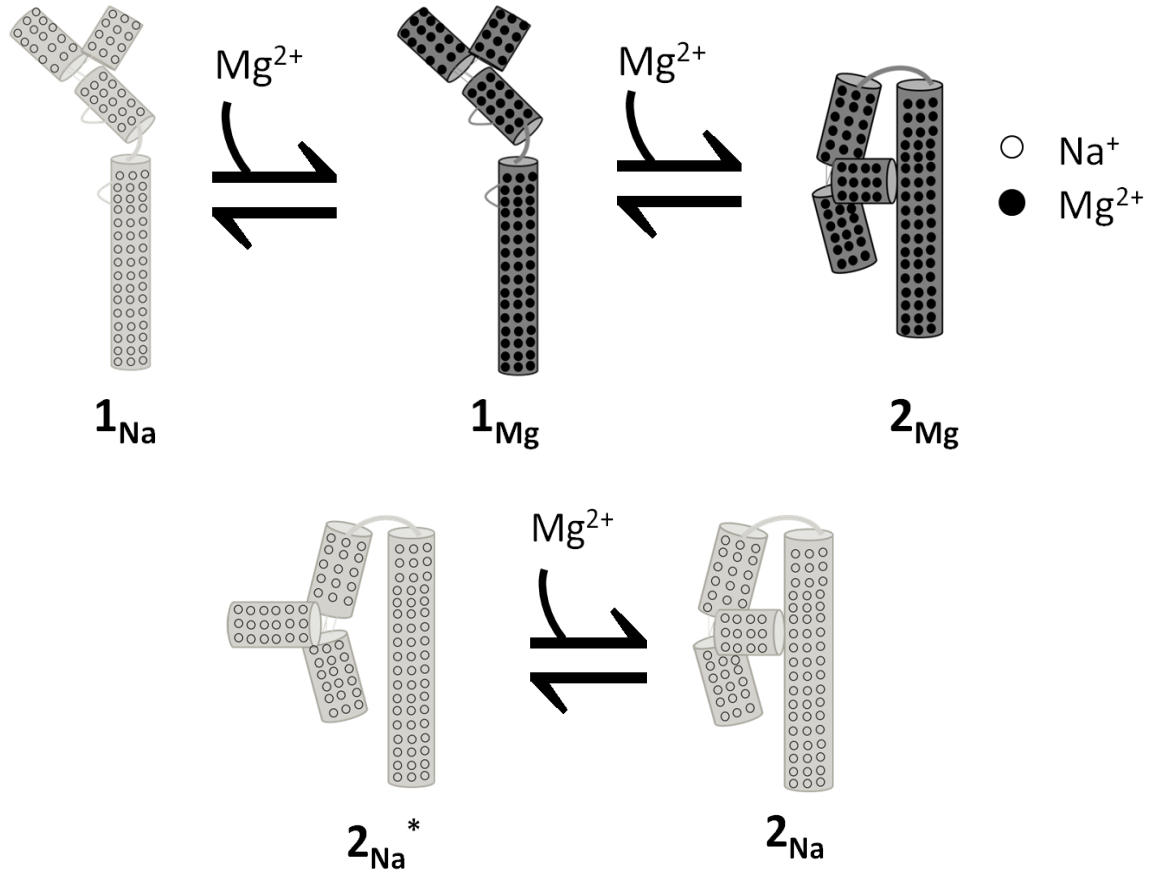

Figure 65. Comparison of P4-P6 association with cations during folding in low-salt and high-salt conditions. Top: In low-salt, extended P4-P6 with Na^+-form helices (1_{Na}) converts to an extended Mg^{2+} intermediate (1_{Mg}) before the RNA collapses to a compact structure. Bottom: 2 M NaCl (high salt) induces a compact conformation of P4-P6 (2_{Na}*) which requires Mg^{2+} to attain the native fold (2_{Na}). Helical regions are in Na^+-form.

Affinity of Mg^{2+} for A-form RNA

Our data suggests that unfolded P4-P6 with double-stranded and single-stranded regions have relatively high affinity for Mg^{2+}. In low-salt conditions, the affinity of Mg^{2+} for duplex regions of P4-P6 appears to be higher than the affinity for the specific coordination site in P4-P6. This finding is consistent with results from our electron transfer experiments (Chapter 2) showing that Fe^{2+}, at very low concentrations (e.g. 6 μM) associates with RNAs (including P4-P6) and catalyzes redox reactions (61). We

observed that Mg^{2+} can inhibit the redox activity of Fe^{2+}-RNA complexes indicating that Mg^{2+} is able to compete with Fe^{2+} for association with RNA under low salt conditions. Collectively, those data suggested that non-native RNA structures possess Mg^{2+} binding sites with micromolar or lower dissociation constants.

Micromolar binding to Mg^{2+} has been reported previously in tRNA under low salt conditions (5,98,99). In addition, it was observed that in low monovalent environments, Mg^{2+} binds to double-stranded DNA with high affinity (100), with a K_D of around 5×10^{-6} M. Combined, these results support the existence of extremely tight Mg^{2+} binding sites in partially unfolded RNA in general. Our data agrees with these observations. Further work will be beneficial for estimating the binding affinity of unfolded regions of P4-P6 under low salt conditions.

Concluding remarks

This work reveals many new details of RNA conformations in solution, but also opens the door for several paths for future exploration. The sequence dependence observed in our results can be further investigated in future experiments using RNA homoduplexes under different conditions. RNA structure might be influenced by cations that display preferential binding to certain residues.

It is not clear whether the peaks observed here correspond to distinct signatures of RNA conformations. Additional studies needed to determine the origins of the structural changes observed. For example, significant work on polynucleotides that form G-quadruplexes has allowed researchers to be able to use CD to distinguish between parallel and anti-parallel (and other) G-quadruplex conformations, based on positions of the peaks. Similar features of RNA duplexes could be potentially identified using CD and

other structural methods to study correlations between RNA structure and peaks in CD signal.

Finally, our results suggest that tightly-bound, residual Mg^{2+} ions that remain associated with RNA after purification and/or are scavenged from the environment after purification can obscure Mg^{2+}-dependent transitions in cation binding experiments. We observed in these studies that the lowest [Mg^{2+}]-dependent binding event, i.e. the structural change from the Na^{+}-form of unfolded P4-P6 to the Mg^{2+}-form, was only detected after divalent chelators (EDTA, DCTA or DTPA) were added to the RNA prior to Mg^{2+} titration. This suggests that if special precautions are not taken, purified RNAs can be associated with tightly-bound Mg^{2+} ions.

Additionally, we have shown that unfolded P4-P6 RNA, with secondary structure, has high affinity for Mg^{2+}. Previous discussions have tended to characterize this binding as a loose association of the ionic atmosphere with the RNA, but we show here that even though the Mg^{2+} ions may be mobile, they bind very tightly to duplex RNA. We also show that the A-form duplex appears to bind Mg^{2+} more tightly than coordination sites in RNA, under low-salt conditions. This demonstration may require a revision of models of RNA electrostatics and of hierarchical pathways of RNA folding. This work also reinforces the usefulness of a finer classification of metal-ion interactions, *viz* free, condensed, glassy and chelated ions (1). Our results reveal a group of tightly bound divalent ions that are not involved in chelation or tertiary structure formation. Therefore, a broad classification of ion interactions into ‘diffuse’ and ‘chelated’ would be a vague and slightly misleading description that would not accurately encompass the major classes of RNA-ion interactions.

CHAPTER FIVE

QM INVESTIGATIONS OF MG COMPLEXES

Introduction

Some of the data in this chapter was used in a research publication: adapted from previously published work: Petrov, A.S., Bernier, C.R., Hsiao, C.L., Okafor, C.D., Tannenbaum, E., Stern, J., Gaucher, E., Schneider, D., Hud, N.V., Harvey, S.C. *et al.* (2012) RNA-Magnesium-Protein Interactions in Large Ribosomal Subunit. *J. Phys. Chem. B,* **116**, 8113-8120. This data refers to geometry optimizations that I performed on the ribosomal magnesium microcluster complex, D2, using density functional theory.

Mg^{2+}-chelation complexes are found in many large RNAs, including the 23S rRNA and P4-P6 domain RNA. Magnesium has a special relationship with phosphate oxyanions, able to form bi-, tri- and tetradentate complexes with oxygen atoms attached to phosphorus (OP atoms) in nucleotides. Mg^{2+} can stabilize distinct conformational states of RNA. Computational methods provide a powerful way to investigate the driving force for Mg^{2+}-RNA interactions.

Continuum approaches have been successfully used to understand RNA association with diffuse ions (101-103). Molecular dynamics simulations have been used to investigate magnesium binding to phosphate oxyanions of RNA (104). Predicting the binding geometry and energies of coordinated cations presents a unique challenge. The energies involved in these first-shell interactions typically possess both electrostatic and non-electrostatic components. Non-electrostatic components include polarization, charge transfer and exchange correlation (105,106). These features are dependent on the specific nature of the cation and the geometry of the coordination complex. This ion-specificity

poses a disadvantage to continuum methods such as the Nonlinear Poisson-Boltzmann theory. Conventional molecular dynamics force fields are not accurately parameterized for predictions of geometries and energetic of directly coordinated magnesium ions (107,108). The energetic of cation association with nucleic acids can be however be accurately characterized using high-level theory with *ab initio* or density functional methods. (109-115).

ADP-Mg^{2+}

Adenosine diphosphate forms complexes with Mg^{2+} which are predictive of Mg^{2+} interactions with other multidentate OP ligands, including RNA. Mg^{2+} interacts with non-bridging OP atoms by monodentate or bidentate chelation (Figure 66). Monodentate chelation is observed to occur exclusively with OβP, while bidentate chelation involves both OαP and OβP (10). Bidentate chelation complexes Mg^{2+} with ADP are six-membered rings consisting of atoms Mg^{2+}-OαP-P-O-P-OβP-Mg^{2+}. Bidentate chelation is favored between OP atoms attached to neighboring P atoms, as chelation formed by two OP atoms bound to a common P atom would require a ring size of four.

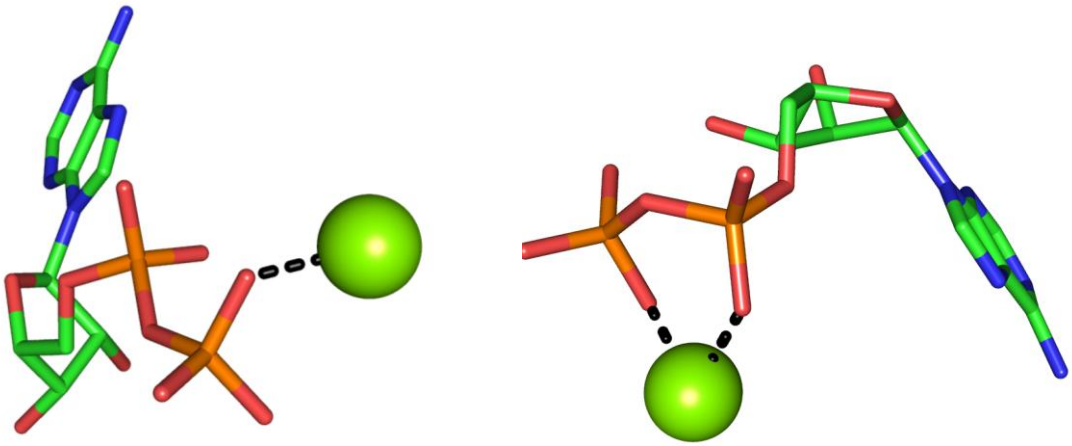

Figure 66. ADP-Mg^{2+} complexes. Left, monodentate chelation (from PDB 1G6H). Right, bidentate chelation (PDB 1BYQ)

D2 complex

A magnesium microcluster is a dinuclear Mg-RNA complexes that consists of two paired Mg^{2+} ions chelated by a common bridging phosphate in the form: Mg^{2+}_{a}-(O1P-P-O2P)–$Mg^{2+}_{b.}$ The bridging phosphate is part of a 10-membered chelation ring in the form: Mg^{2+}_{a} –(OP-P-O5'-C5'-C4'-C3'-O3'-P-OP)–Mg^{2+}_{b}. The two phosphate groups in this motif are contributed by adjacent residues along the RNA backbone (Figure 6). Four magnesium microclusters are found in the ribosomal LSU, three of these flanking the PTC (D1, D2, D4) (Figure 67).

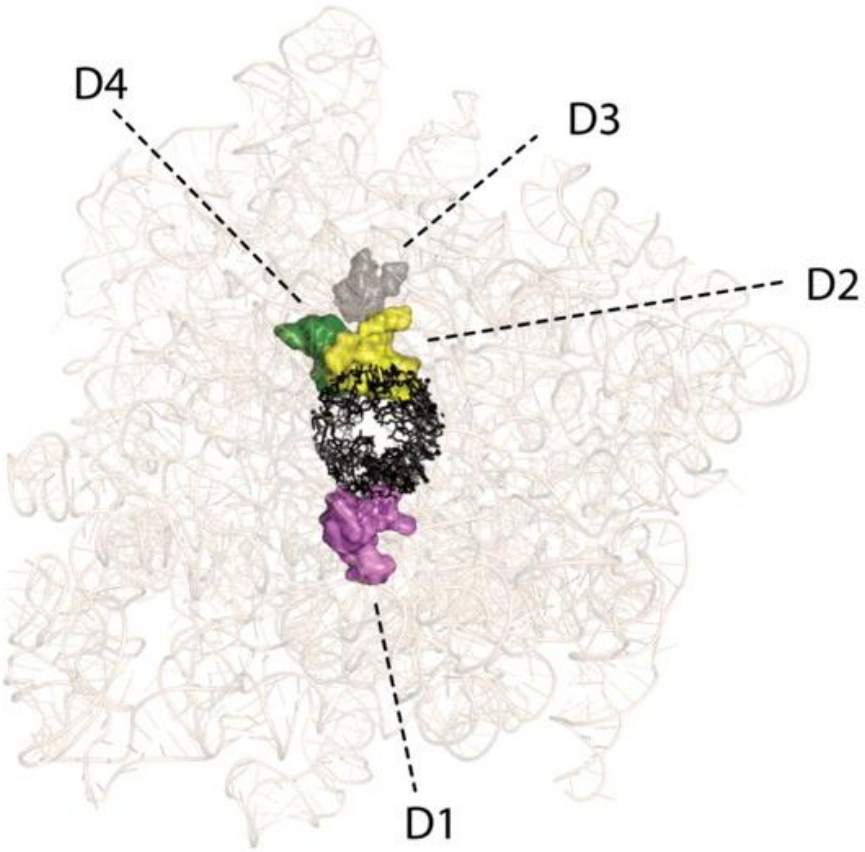

Figure 67. A view into the PTC. Four Mg^{2+}micrcolusters are observed in the LSU of *H. marismortui* (PDB entry 1JJ2). The RNA atoms lining the polypeptide exit tunnel are accented in black. Mg^{2+}microclusters D1, D2 and D4 encircle the PTC. Reprinted from (21) with permission.

In microcluster D2 of *Haloarcula marismortui*, the Mg^{2+}_{a}-(O1P-P-O2P)–Mg^{2+}_{b} is composed of the phosphate group of G877 along with Mg^{2+} ions 8003 and 8013 (Figure 68). The 10-membered ring system is composed of the phosphate group and ribose atoms of A876 along with the phosphate group of G877. Both Mg^{2+} ions incorporate phosphates of remote RNA segments (A2624, G2623) into first-shell coordination sites.

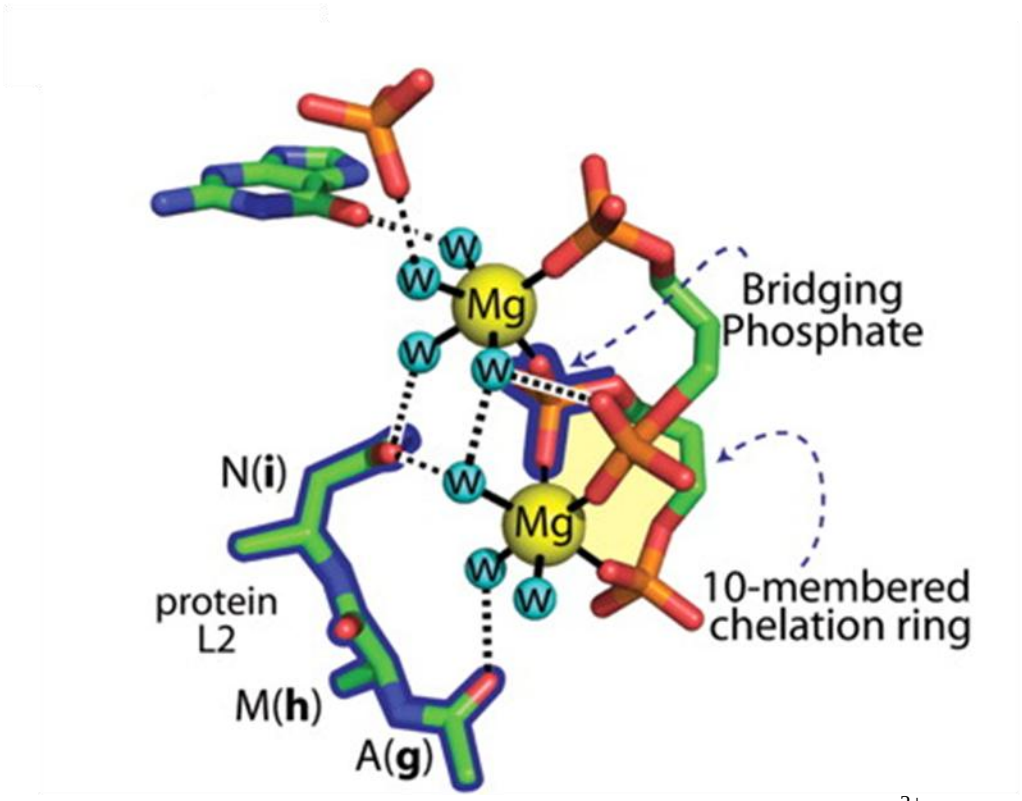

Figure 68. Magnesium microcluster D2 of *H. marimortui* showing Mg^{2+} atoms and RNA ligands. Reprinted from (21) with permission.

D2 is closely associated with ribosomal protein L2. An 18-amino acid loop of L2 (loop-L2/D2) forms a binding pocket for D2. The conformation of loop L2/D2 is highly conserved between *T. thermophilus* and *H. marismortui*, with a 0.6Å RMSD of atomic

positions between both structures. Ribosomal protein (rProtein) L2 interacts with D2 via water molecules. Four of the first-shell water molecules of the D2 magnesium ions interact directly with L2. Of all other rProteins, L2 makes the most extensive interactions with Mg^{2+} ions. Three amino acids of the D2/L2 loop in positions 7 – 9 (AMN in *T. thermophilus*), D2 and the water molecules form an assembly. While there is modest sequence variability in the identity of the amino acid triad in various organisms, a sequence alignment of L2 from 121 species (distributed over all three domains of life) reveals that AMN is observed most frequently (65%). The positions of the backbone atoms of the AMN segment of rprotein L2 are highly conserved (21).

Computational Methods

Geometry optimizations

A structure of the ADP molecule was obtained from a complex in the Protein DataBank to use as a template (2PYW, IBYQ). The adenosine atoms were removed, leaving only the C3' atom of the ribose. This was used for a methyl cap in lieu of the rest of the nucleotide.

The coordinates for the D2 complex were extracted from the crystal structure of the *T. thermophilus* ribosome (PDB 1D: 2J00, 2J01). The microcluster contains two magnesium ions, Mg 66 and Mg 70, first shell water molecules, and 23S rRNA fragments that interact with the magnesium ions (ADE 783, GUA 784, GUA 2588 and ADE 2589). While heavy atoms were fixed in the crystal structure positions, hydrogen atoms and first shell water molecules were optimized using b3lyp/6-31++G(d,p) level of theory in the Gaussian 03 suite of programs (116). The water molecule positions were initially

modeled using the water positions of the LSU of *H. marismortui* (PDB ID:1JJ2). The D2 complexes are virtually indistinguishable in both structures (21), but the *H. marismortui* ribosome is of higher resolution and contains more detail in the hydration layer than the *T. thermophilus* ribosome.

Interaction energies

The interaction energies for all complexes were calculated as a difference between the single point energies of a complex and its monomers. The b3lyp/6-311++G(d,p) level of theory was used, with energies reported with the 50% correction (117,118)for the Basis Set Superposition Error (BSSE) using the counterpoise procedure of Boys and Bernardi (119). All calculations are performed in the gas phase. Aqueous phase calculations were performed at the B3LYP/6-311g++(d,p)//B3LYP/6-311g++(d,p)[cpcm] level. As the D2 complex is buried within the LSU in an area with a low dielectric coefficient and not exposed to bulk water, the polarization effects of bulk solvent could be neglected in these calculations.

Stepwise building of Mg^{2+} complexes

ADP-Mg^{2+} complexes

The complexes are obtained by considering two possible reaction systems; A) one ADP molecule reacts with two Mg^{2+} ions in the presence of excess Mg^{2+}; and B) one Mg^{2+} ions reacts with two ADP molecules in excess ADP, as shown in figure 69.

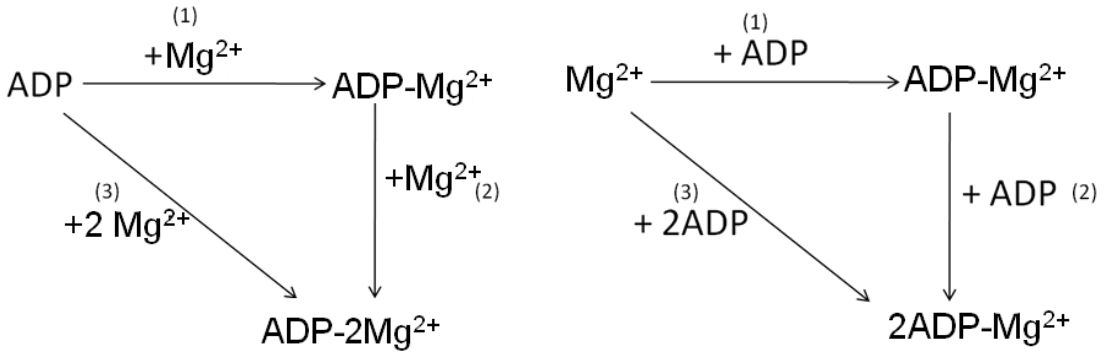

Figure 69. Thermodynamic cycles for two systems. Excess Mg^{2+} (left) and excess ADP (right).

In reaction (1) for both systems, as shown in Figure 69, ADP in a -3 charge state (ADP^{3-}) combines with hexahydrated Mg^{2+}, ($Mg^{2+}(H_2O)_6$) to form the ADP-Mg complex which partially dehydrates the Mg^{2+} ion.

$$ADP^{3-} + Mg^{2+}(H_2O)_6 \rightarrow ADP^{3-}\text{-}Mg^{2+}\bullet(H_2O)_4 \text{ complex} + 2H_2O \quad (1)$$

ADP-(Mg^{2+})$_2$

ADP-Mg^{2+} combines with Mg^{2+} to form the ADP-$(Mg^{2+})_2$ complex.

$$ADP^{3-}\text{-}Mg^{2+}\bullet(H_2O)_4 \text{ complex} + Mg^{2+}(H_2O)_6 \rightarrow ADP^{3-}\text{-}(Mg^{2+}\bullet(H_2O)_4)_2 \text{ complex} + 2H_2O \quad (2A)$$

Reaction (3A) is defined in the thermodynamic cycle as a combination of reactions (1) and (2A):

$$ADP^{3-} + 2Mg^{2+}(H_2O)_6 \rightarrow ADP^{3-}\text{-}(Mg^{2+}\bullet(H_2O)_4)_2 \text{ complex} + 4H_2O \quad (3A)$$

ADP_2-Mg^{2+}

ADP-Mg combines with ADP to form the ADP_2-Mg^{2+} complex. The Mg^{2+} undergoes further dehydration.

ADP^{3-}-$Mg^{2+}\bullet(H_2O)_4$ complex + ADP^{3-}

$\rightarrow$ $2ADP^{3-}$-$Mg^{2+}\bullet(H_2O)_2$ complex + $2H_2O$ (2B)

Reaction (3B) is defined in the thermodynamic cycle as a combination of reactions 1 and (2B).

$$2ADP^{3-} + Mg^{2+}(H_2O)_6 \rightarrow 2(ADP^{3-})\text{-}Mg^{2+}\bullet(H_2O)_2 \text{ complex} + 4H_2O \quad (3B)$$

D2 microcluster

A construction process, a series of partial complexes that are converted in a stepwise fashion to the D2 complex, was used. The approach is akin to the Auf Bau process but on a molecular scale. All starting coordinates for intermediate complexes were taken from the crystal structure. Unless otherwise specified, all heavy atoms were fixed while hydrogens and waters and other added atoms (e.g. capping methyl group atoms) were optimized. A series of interaction energies were calculated for each construction step. The series of complexes of increasing size and complexity are described below and shown in 2D in Figure 70.

1. R1: The smallest complex was an RNA moiety, R1, 5' methyl-phosphate ribose 3' methyl-phosphate. It is made of a ribose with 5' and 3' phosphate groups that are not in close proximity (Figure 70A). 5' and 3' phosphates were capped with methyl groups. This is RNA in an open conformation. R1 was fully optimized in all atoms.
2. C1: The second complex was created by closing the R1 complex RNA on a partially dehydrated magnesium ion, M1, to form a bidentate clamp, C1 (Figure

70B). The bidentate clamp is the mononuclear RNA-Mg^{2+} complex formed when OP atoms of adjacent residues chelate a common Mg^{2+} (Figure 4) forming a ten-membered ring containing the atoms Mg^{2+}-OP-P-O5'-C5'-C4'-C3'-O3'-P-O^2P-Mg^{2+}. $Mg^{2+}(H_2O)_6$ was optimized at the b3lyp/6-311++G(d,p) level of theory.

3. C2: The third complex was created by the addition of another RNA moiety, R2 (identical to R1) to coordinate to the magnesium ion, leading to further dehydration (Figure 70C). R2 clamps to the magnesium ion via its 3'phosphate. Phosphates were capped with methyl groups.
4. C3: The fourth complex was created by the binding of another partially-dehydrated magnesium ion, M2 (Figure 70D). The magnesium is bound by coordination to the 5' phosphate group of R2. R2 is still in an open conformation with the phosphate groups not within close proximity.
5. D2: The final complex, D2, emerges as the 3'phosphate of R1 RNA/C1 clamp binds to magnesium ion M2 by coordination. This phosphate becomes a bridging phosphate, coordinated to two magnesium ions. This induces an open-to-closed conformational change, leads to further dehydration of magnesium ion M2, and creates the microcluster motif, consisting of the bridging phosphate which is part of a ten-membered ring (Figure 70E). D2 is also shown in Figure 68.

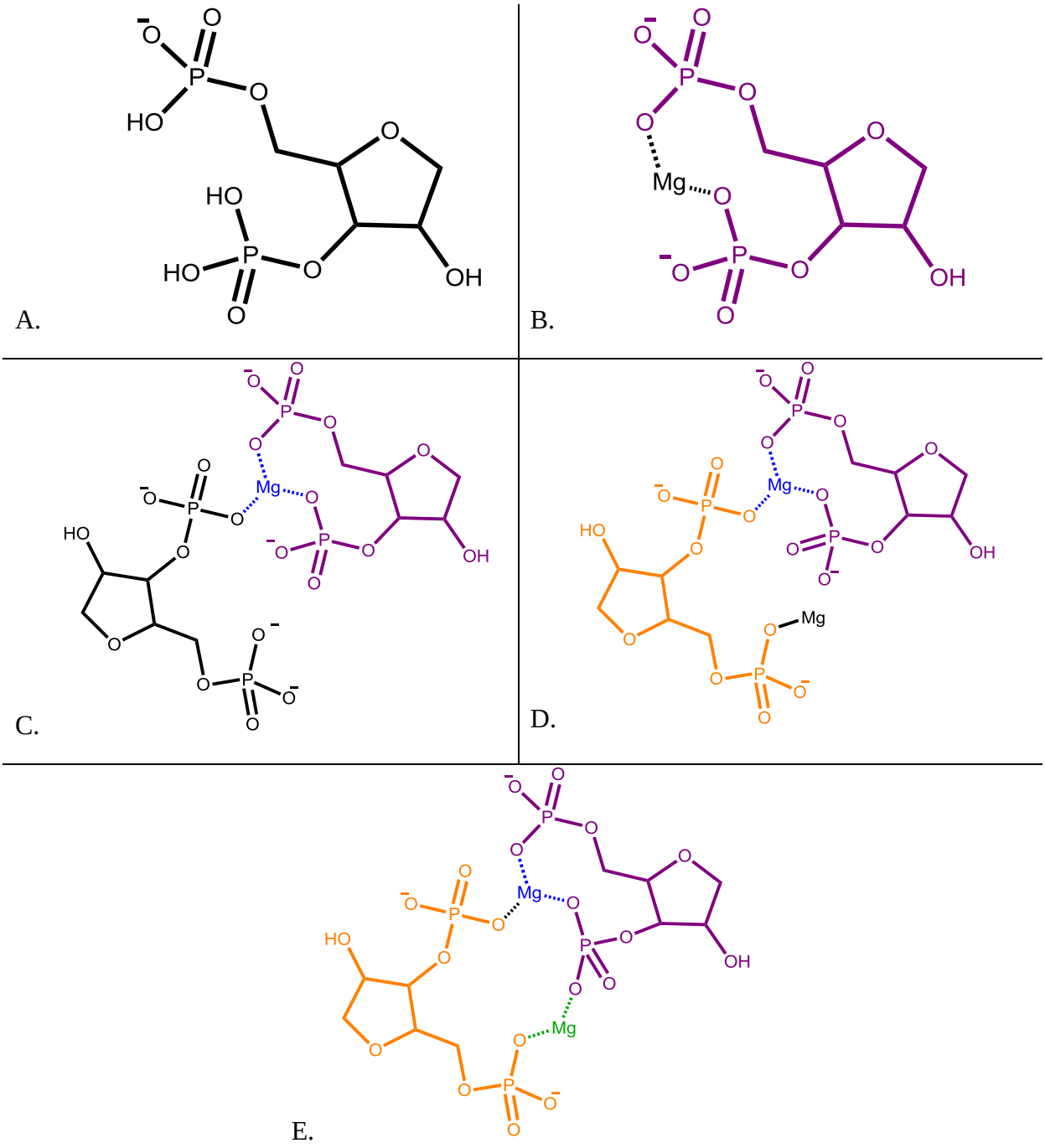

Figure 70. Intermediates of complexes in building of D2. In each addition, atoms of previously added components are changed to the same color. A) R1 RNA moiety, 5' methyl-phosphate ribose 3' methyl-phosphate. B) C1, Clamp formed upon addition of Mg^{2+}. C) C2, formed by addition of RNA moiety R2 to C1. D) C3, complex formed upon addition of Mg^{2+} to C2. E) D2 complex, formed upon chelation of Mg^{2+} to R2 moiety. All Mg ions are octahedrally coordinated, but H_2O ligands are not shown.

Results

ADP-Mg^{2+} complexes (2D and 3D representations) are shown in Figure 71.

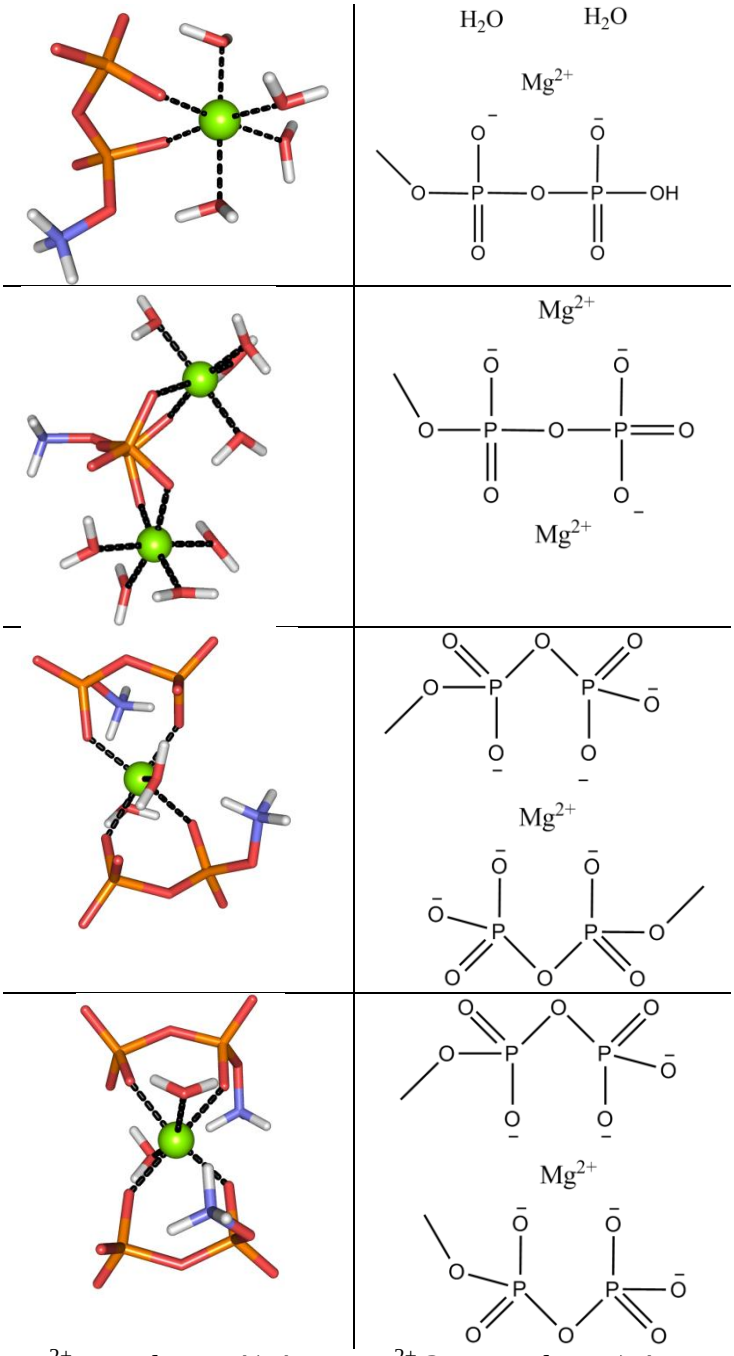

Figure 71. ADP-Mg^{2+} complexes. A) ADP-Mg^{2+} 3D complex. B) ADP-Mg^{2+} complex with axial waters omitted for clarity. C) ADP-$(Mg^{2+})_2$ 3D complex. D) ADP^{3-}-$(Mg^{2+})_2$ complex with waters omitted for clarity. E) ADP_2-Mg^{2+} complex, with anti-parallel coordination of ADP molecules. F) Anti-parallel ADP_2-Mg^{2+} complex with axial waters omitted. G) ADP_2-Mg^{2+} complex, with anti-parallel coordination of ADP molecules. H) parallel ADP_2-Mg^{2+} complex with axial waters omitted.

ADP-Mg^{2+} complexes

ADP^{3-}-$Mg^{2+}\bullet(H_2O)_4$ complex

$ADP^{3-} + Mg^{2+}(H_2O)_6 \rightarrow ADP^{3-}$-$Mg^{2+}\bullet(H_2O)_4$ complex + $2H_2O$ (1)

This reaction (1) proceeds in three steps.

Step 1: This begins with free ADP and $Mg^{2+}\bullet(H_2O)_4$, with the conformation of ADP changing from open to closed. (The conformation of open ADP was obtained by optimizing ADP in the absence of magnesium).

Step 2: The magnesium releases two water molecules in partial dehydration.

Step 3: The partially dehydrated magnesium coordinates two phosphate oxygen atoms of ADP (α and β) to complete the octahedral geometry (Figure 71A, B). This closed ADP conformation is obtained by optimizing the complex in an aqueous environment, while the magnesium retains its octahedral coordination. An interaction energy of -22.6 kcal/mol was calculated for the association of ADP and Mg^{2+} in gas phase.

ADP^{3-}-$(Mg^{2+}\bullet(H_2O)_4)_2$ complex

ADP^{3-}-$Mg^{2+}\bullet(H_2O)_4$ complex + $Mg^{2+}(H_2O)_6$

$\rightarrow ADP^{3-}$-$(Mg^{2+}\bullet(H_2O)_4)_2$ complex + $2H_2O$ (2A)

$ADP^{3-} + 2Mg^{2+}(H_2O)_6 \rightarrow ADP^{3-}$-$(Mg^{2+}\bullet(H_2O)_4)_2$ complex + $4H_2O$ (3A)

In the presence of excess magnesium, reaction (2A) takes place in two steps.

Step 1: Partial dehydration of a second magnesium ion

Step 2: Magnesium coordinates the second pair of α and β phosphate oxygens,

completing the octet (Figure 71C, D)

The interaction energy for ADP^{3-}-$(Mg^{2+}\bullet(H_2O)_4)_2$ was calculated from reaction (2A) and from reaction (3A). According to the thermodynamic cycle, the sum of reactions (1) and (2A) should equal (3A). These energies are given in Table 3.

Table 3. Interaction energies calculated for ADP-Mg^{2+} complexes. All energies include BSSE.

Reaction	Complex	E [kcal/mol]	
		gas phase	**aqueous phase**
1	ADP^{3-}-$Mg^{2+}\bullet(H_2O)_4$	-550.7	-22.6
2A	ADP^{3-}-$(Mg^{2+}\bullet(H_2O)_4)_2$	-180.9	-10.4
2B (P)	$2ADP^{3-}$-$Mg^{2+}\bullet(H_2O)_2$		-13.7
2B (AP)	$2ADP^{3-}$-$Mg^{2+}\bullet(H_2O)_2$		-11.4
3A	ADP^{3-}-$(Mg^{2+}\bullet(H_2O)_4)_2$	-731.6	-33.0
3B (P)	$2(ADP^{3-})$-$Mg^{2+}\bullet(H_2O)_2$		-36.3
3B (AP)	$2(ADP^{3-})$-$Mg^{2+}\bullet(H_2O)_2$		-34.0

<u>$2ADP^{3-}$-$Mg^{2+}\bullet(H_2O)_2$ complex</u>

ADP^{3-}-$Mg^{2+}\bullet(H_2O)_4$ complex + ADP^{3-}

$\rightarrow$ $2ADP^{3-}$-$Mg^{2+}\bullet(H_2O)_2$ complex + $2H_2O$ (2B)

$2ADP^{3-} + Mg^{2+}(H_2O)_6 \rightarrow 2(ADP^{3-})$-$Mg^{2+}\bullet(H_2O)_2$ complex + $4H_2O$ (3B)

With excess ADP present, reaction (2B) occurs following (1) in two steps.

Step 1: The magnesium in the ADP^{3-}-$Mg^{2+}\bullet(H_2O)_4$ loses two additional water molecule.

Step 2: Another ADP molecule binds to the existing complex by phosphate oxygen coordination.

Assuming that the first ADP molecule coordinates the magnesium ion by α and β phosphate oxygens, the second ADP molecule could conceivably bind to the ADP-Mg^{2+}

complex in one of two ways: parallel to the first ADP, or anti-parallel with respect to the first. Both complexes are shown (Figures 71E-H). The interaction energy is calculated for both of these complexes according to reactions (2B) and (3B) and shown in table 3.

Conversion from open to closed ADP

There is a penalty for converting ADP from the 'open' to 'closed' forms. We defined an 'open' conformation of ADP as free, uncomplexed ADP. The 'closed1' conformation refers to ADP in the ADP-Mg^{2+} complex. The closed2 conformation refers to ADP in the ADP-$(Mg^{2+})_2$ complex. In the process of reactions 1, 2A and 3A, ADP proceeds from an open, to closed1 and finally closed2 conformations. The energy difference between 'open' and 'closed1' forms of ADP is 4.5 kcal/mol in the aqueous phase and 19.7 kcal/mol in the gas phase. The difference between the closed1 and closed2 conformations of ADP is 5.7 kcal/mol and 12.3 kcal/mol in aqueous and gas phases respectively. These values are shown in Table 4.

Table 4. Energetic penalty of conformational changes in ADP

ADP-conformation	ADP-complex	$\Delta E_{open-closed}$ [kcal/mol]	
		[b]**gas**	[c]**aqueous**
Open-closed1		19.7	4.5
Closed1-closed2		12.3	5.7

Polymorphism of ADP-Mg^{2+} complexes

With five phosphate oxygen atoms ($\alpha1$, $\alpha2$, $\beta1$, $\beta2$, $\beta3$) available for Mg^{2+} coordination, an ADP^{3-}-$Mg^{2+}\bullet(H_2O)_4$ complex could be formed in several ways. In the results reported here, each Mg^{2+} ion coordinates one α and one β phosphate oxygen (Figures 71). Two other possible conformations (α,α or β,β) are shown in Figure 72.

Interaction energies calculated for these complexes (values in Table 5) show that the α,β complex is more likely to form than the other two possibilities.

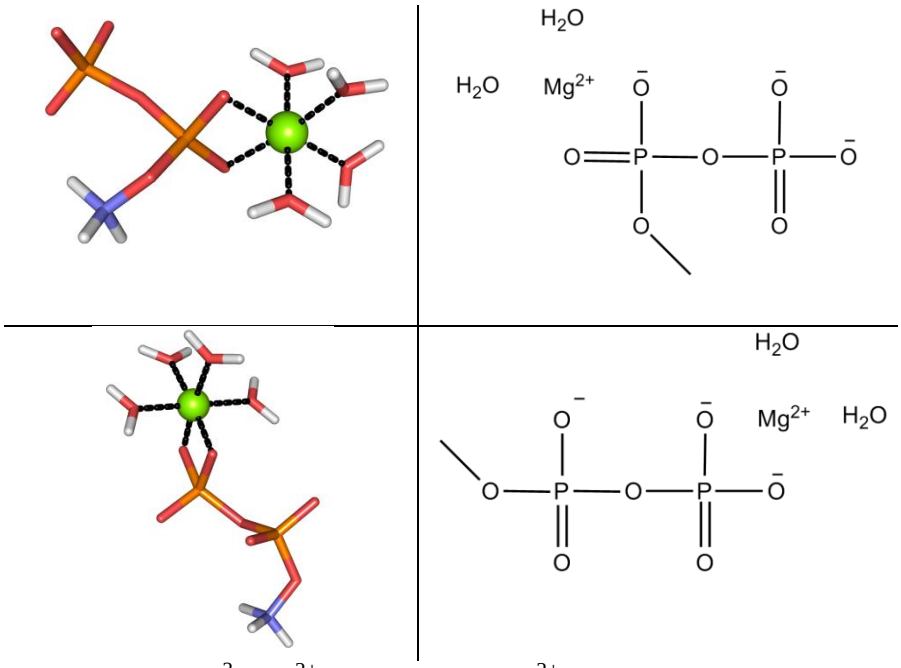

Figure 72. ADP^{3-}-Mg^{2+}•$(H_2O)_4$ with Mg^{2+} coordinating to α OP atoms (top) and β OP atoms (bottom).

Table 5. Interaction energies for various ADP^{3-}-Mg^{2+}•$(H_2O)_4$ complexes in aqueous phase

Coordinating OP atoms	[a]E [kcal/mol]
α, β	-22.6
α,α	-6.5
β,β	-19.4

D2 Complex and intermediates

Interaction energies of complex formation were calculated for the intermediate complexes of D2. All energies were obtained in gas phase. Optimized geometries are shown in Figure 73.

C1 complex

$R1 + Mg^{2+}(H_2O)_6 \rightarrow C1 + 2H_2O$

The energy of the C1 complex, calculated using the above reaction, was -354.7 kcal/mol.

C2 complex

$C1 + R2 \rightarrow C2 + H_2O$

Interaction energy: -112.1 kcal/mol.

D2 complex

An interaction energy could not be obtained for the C3 complex. However, D2 complex contains the exact elements of C3 complex, with the difference of a chelation interaction that is formed between the magnesium ion M2 and the R1 moiety (Figure 71D, E). Therefore the interaction energy calculated for D2 according to the reaction below accounts for two things: 1) the formation of C3, via the the addition of the second Mg ion,M2; and 2) the formation of the coordination bond between M2 and R1 that is present in D2, accompanied by a conformational change and the release of one water molecule.

$C2 + Mg^{2+}(H_2O)_6 \rightarrow D2 + 2H_2O$

Interaction energy: -301.9 kcal/mol

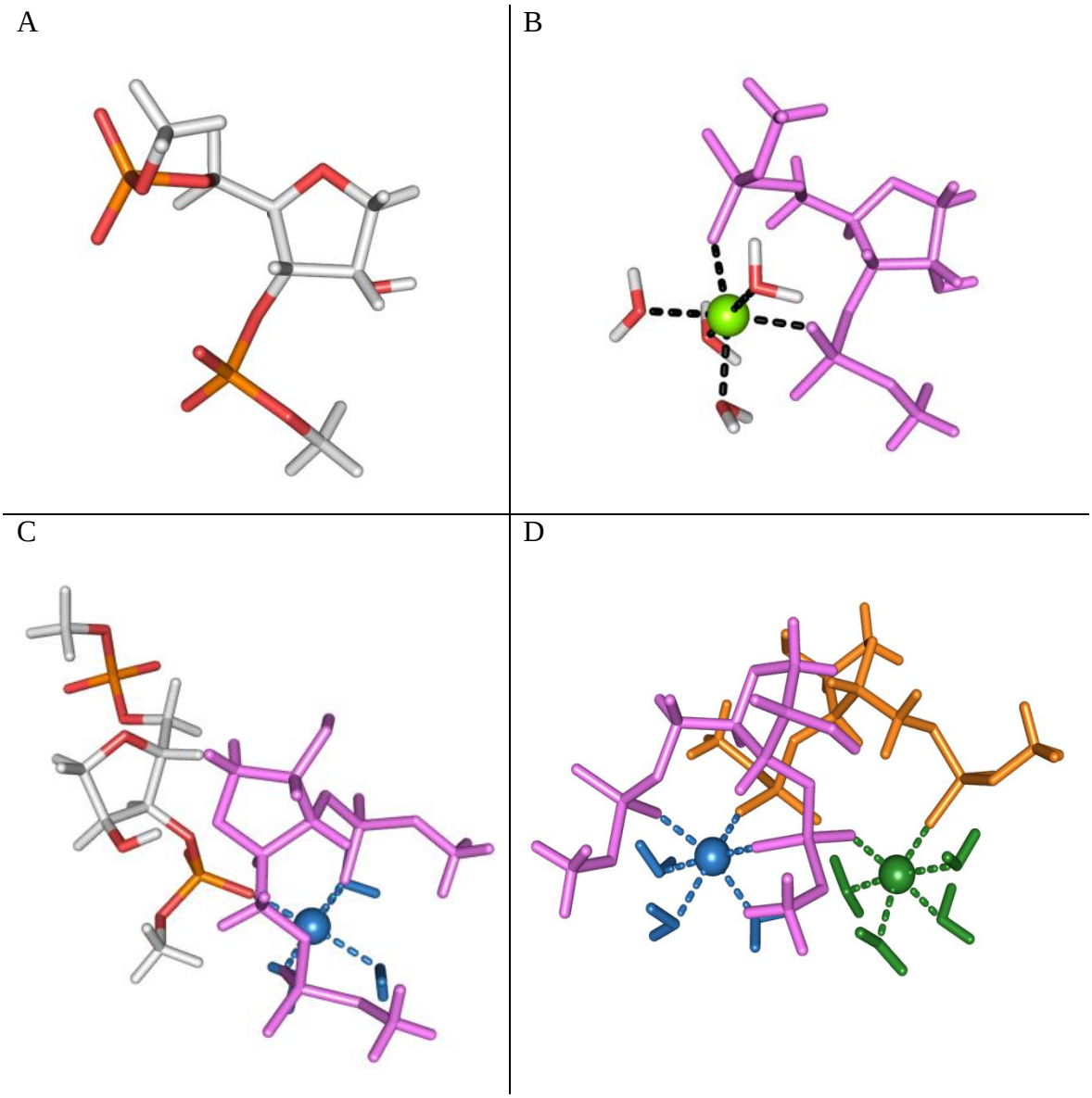

Figure 73. Optimized geometries of the intermediates of complexes in building of D2. The same coloring scheme is used in Figure 70. A) R1 B) C1 C) C2 D) D2. C3 is missing, as an optimized geometry was not obtained.

Alternative pathway for D2 formation

An alternative pathway for the formation of D2 from the bidentate clamp (C1) complex was briefly explored (Figure 74). The pathway is described below, along with interaction energies for each step.

C1 → C2*: C1 binds Mg^{2+}, M2, to form complex C3* with dehydration of Mg^{2+}. M1 coordinates the 3'-phosphate of the clamp, turning it into a bridging phosphate.

$$C1 + Mg^{2+}(H_2O)_6 \rightarrow C2^* + H_2O \quad (IE = -118.9 \text{ kcal/mol})$$

C2* → C3*: An RNA moiety (R2) binds to C2* by coordination to Mg^{2+} M2 via its 5'-phosphate group, and loss of an additional H_2O.

$$C2^* + R1 \rightarrow C3^* + H_2O \ (IE = -312.8 \text{ kcal/mol})$$

C3* → D2: the 3'-phosphate of the R2 moiety coordinates to the original clamp Mg^{2+}, forming the complex D2 with the loss of H_2O.

$$C3^* \rightarrow D2 + H_2O \ (IE = -6.7 \text{ kcal/mol})$$

Both pathways are compared in Figure 75. The total energy for formation of D2 is the same for both pathways, as enthalpy (interaction energy) is a state function.

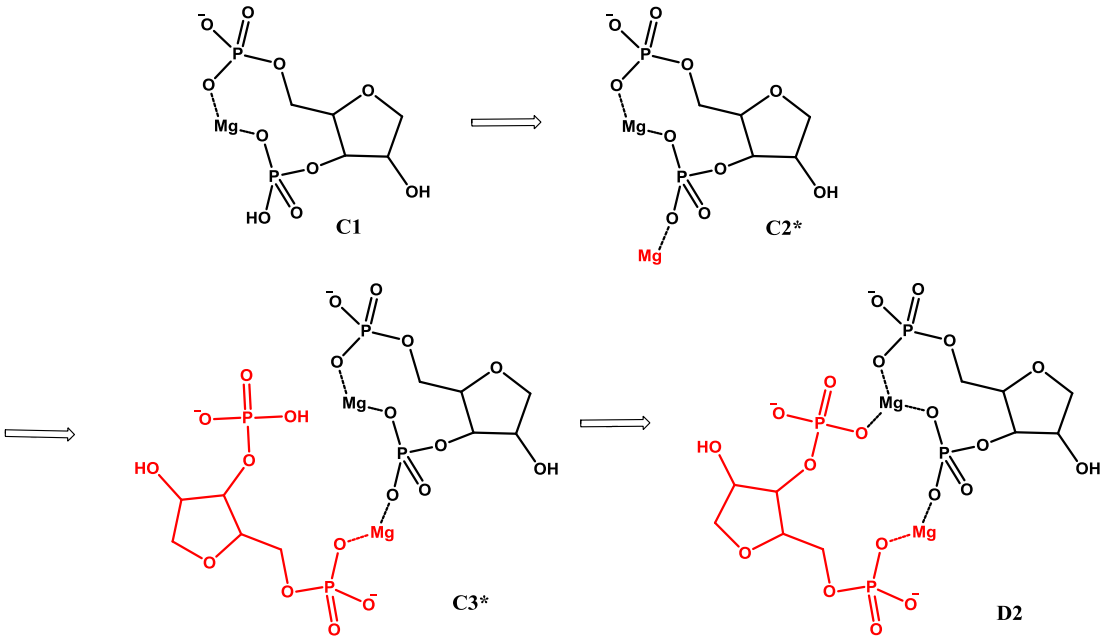

Figure 74. Alternative pathway for the formation of D2 complex (with intermediates).

Cl (bidentate clamp)

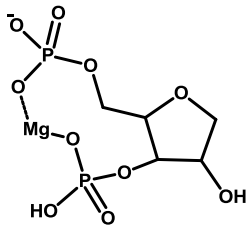

C1 →C2 -112.1 kcal/mol	C1 → C2* -101.2 kcal/mol
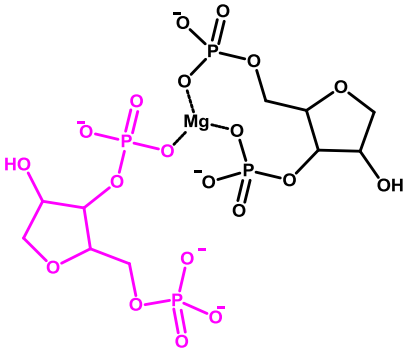	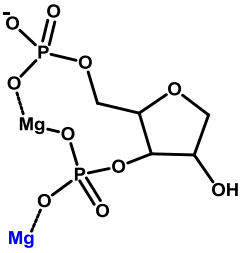
C2 → C3 **	C2* → C3* -306.1 kcal/mol
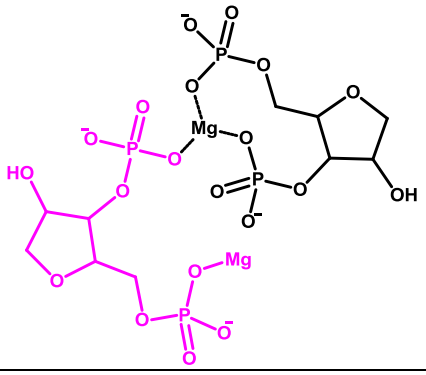	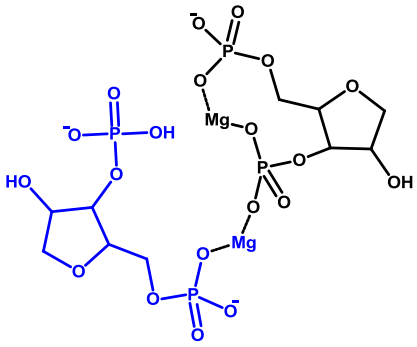
C2 – D2 -301.9 kcal/mol	C3* → D2 -6.7 kcal/mol
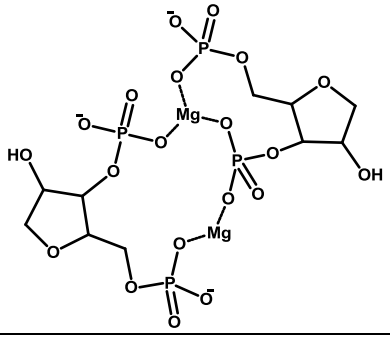	
C1 →D2 -414 kcal/mol	C1 →D2 -414 kcal/mol

Figure 75. Comparison of two pathways for the formation of D2 complex, showing gas phase interaction energies.

Discussion

ADP-Magnesium

The study of ADP-Mg^{2+} interactions using high level calculations allows for the observation of specific effects that are not able to be observed using continuum methods or molecular mechanics approaches. We observe anti-cooperativity in ADP-Mg^{2+} binding, after the ADP^{3-}-Mg^{2+}•$(H_2O)_4$ is first formed. The formation of this first complex (-22.6 kcal/mol) is more favored than is the addition of an extra ADP (-13.7 kcal/mol) or Mg^{2+} (-10.1 kcal/mol).

We investigate the possibility for polymorphism of ADP^{3-}-Mg^{2+}•$(H_2O)_4$. For a complex formed in which magnesium is (OβP, OαP)- or (OβP, OβP)-coordinated, four-membered chelation rings would be formed. While the interaction energies involved in the (OβP, OβP)-complex (-19.4 kcal/mol) is significantly more favorable than (OαP, OαP) (-6.5 kcal/mol) , both are less favored than the (OαP, OβP) complex (-22.6 kcal/mol). This result is consistent with the lack of observed α,α, or β,β coordination in Protein Data Bank structures. The more favorable interaction in α,β coordination could be the driving force behind the prevalence of this conformation in ADP-Mg^{2+} complexes.

D2 complex

Formation of microcluster D2 is explored. Beginning from the 5' methyl-phosphate ribose 3' methyl-phosphate, the bidentate clamp is formed, and additional components are added until D2 is constructed. Two pathways for formation of D2 are investigated. Intermediate complexes for both pathways were geometry-optimized, and interaction energies for each step obtained. In one pathway, the D2 formation proceeds

by addition of positively charged Mg^{2+} ion to the complex, while in the second pathway, D2 formation proceeds by addition of a negatively charged RNA moiety to the complex. For both pathways, we observe anti-cooperativity after the clamp formation. The energy of adding additional, charged fragments to the clamp is less than the overall energy of clamp formation. The anti-cooperativity could be associated with the charge repulsion in the newly added fragment. We observe that the anti-cooperativity is reversed in the third step of each pathway (Figure 74) when the next, oppositely charged fragment is added. In other words, Mg^{2+} added to the clamp forms the anticooperative clamp-Mg^{2+} complex, and the addition of RNA^{2-} to the above clamp-Mg^{2+} complex allows for charge neutralization, and is therefore a cooperative reaction.

Comparison of both pathways reveals certain preferences in RNA-Mg complex formation. Coordination of a new RNA ligand to a Mg^{2+} ion in a bidentate clamp is revealed to be more favorable than the coordination of a new Mg^{2+} ion to a common phosphate. This might imply that the effect of the Mg^{2+}-Mg^{2+} repulsion is slightly greater than the effect of repulsion between negatively charged phosphate groups. In addition, although the ring closure of C3* to D2 might be expected to be unfavorable, it is observed here to be favorable. This indicates that the favorable interaction energy gained with Mg^{2+} coordination of the phosphate oxygen atoms outweighs the negative penalty of ring closure.

The QM-optimized D2 geometry was used to gain insight into the role of Mg^{2+} in stabilizing rRNA-rProtein interactions (120). The magnesium ions in D2 link rRNA to rProtein L2 by orienting and polarizing water molecules within the first coordination shell of Mg^{2+} (Figure 76). The Mg^{2+} waters are then able to interact strongly with

protein. The inability of other biological cations (e.g. sodium, positively charged amino acids, or polyamines) to polarize and orient water molecules to the same extent is responsible for their inability to substitute for magnesium in RNA. D2-L2 interactions appear to play an important role in the architecture of the LSU. D2-L2 interactions are highly conserved between bacteria and archaea, indicating that it could be a critical component of one of the oldest biological assemblies.

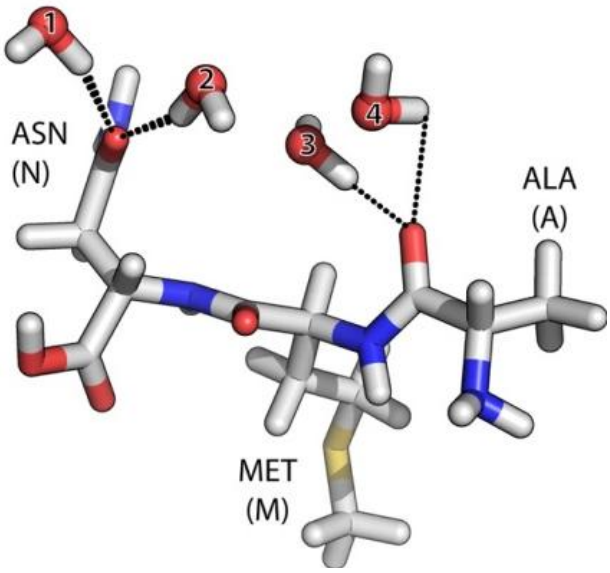

Figure 76. Interactions of four nonpolarized water molecules with ribosomal protein L2. The $(H_2O)_4$-L2 complex is formed by omitting the magnesium ions and the rRNA from D2-L2. Reprinted from (120) with permission.

Using a D2-L2 complex in which the rRNA and magnesium ions were omitted, a difference in the polarization (as calculated by the NEDA analysis, Table 6) was observed. The intact D2-L2 complex has a larger component of polarization (-39.1 kcal/mol) compared to that of the $(H_2O)_4$-AMN complex (-19.3 kcal/mol). This study reveals the significant role played by polarization of water molecules by magnesium. This result is also consistent with previous observations that first-shell incorporation of water molecules by magnesium decreases their pK_a.

Table 6. NEDA energies and components. Electrostatic (EL), polarization (POL), charge-transfer (CT), exchange (EX), deformational (DEF) components and the total interaction energy (TOT) are calculated in the NEDA framework. Reprinted from (120) with permission.

Complex	**EL**	**POL**	**CT**	**EX**	**DEF**	**TOT**
D2-L2	-55.4	-39.1	-94.2	-15.5	165.6	-38.6
$(H_2O)_4$-L2	-34.6	-19.3	-72.2	-12.9	130.6	-8.4

Concluding Remarks

Quantum mechanical methods provide valuable insights into nucleic acid-Mg^{2+} interactions. An investigation has been performed on the factors that affect the stability of the D2-L2 complex. Deconstruction and computational results show that magnesium ions in D2 enhance the interactions of water molecules with L2 rProtein. The importance of the non-electrostatic effects, charge transfer and polarization, for these interactions is shown. Such non-electrostatic effects cannot be captured by MD simulations or continuum methods, therefore these methods will not provide an accurate description of the systems described here. In addition, the insight provided by the energy decomposition (NEDA) is invaluable for understanding the physical factors responsible for observed effects in Mg^{2+} binding. We demonstrate a useful application for QM theory for studying RNA-Mg^{2+} interactions. These studies provide insight that cannot be observed in experiments.

CHAPTER SIX

IDENTIFICATION OF MG^{2+} AND FE^{2+} BINDING SITES IN RNA

Introduction

It is hypothesized that RNA might have used Fe^{2+} as a biological cofactor, on an anoxic early earth. In these conditions, Fe^{2+} was benign and not harmful for RNA. During the GOE, Fe^{2+} would have been replaced by Mg^{2+} in RNA folding and function. The similarities of Mg^{2+} and Fe^{2+} in size and coordination preferences support this hypothesis. Experiments were performed to test the ability of Fe^{2+} to substitute for Mg^{2+} in facilitating RNA folding (30). QM calculations showed that when Mg^{2+} is replaced by Fe^{2+} in a first-shell RNA-metal interaction, the coordination geometry is conserved between both complexes, with nearly identical features for the two. This observation supports the ability of Mg^{2+} to substitute for Fe^{2+} in RNA folding. Additionally, RNA footprinting studies in the presence of Mg^{2+} or Fe^{2+} revealed nearly identical profiles, indicating that all Mg^{2+}-dependent interactions in P4-P6, including the tertiary interactions, were conserved and recapitulated by Fe^{2+}.These findings, along with others in the literature (31), strongly suggest that Mg^{2+} and Fe^{2+} interact at the same binding sites in RNA. Explicit evidence for this hypothesis has not yet been reported.

Metal-induced cleavage of RNA

Metal ion-induced cleavage of RNA has been widely studied (121-125). The mechanism of metal-ion catalyzed cleavage of RNA is not completely understood, and several have been proposed. Regardless, this method has been found to be useful for potentially revealing regions of the RNA molecule in close proximity to metal ions (126).

In-line cleavage

A proposed mechanism for RNA cleavage by metals (127) is that hydrated metal ions cleave RNA by acting as Brønsted bases. The oxygen atom of a bound water molecule abstracts a proton from the 2'-OH group of the ribose, generating a 2-O^- group which attacks the phosphorous atom, with departure of the 5'OH group (Figure 77). This attack is facilitated by a conformation in which the attacking nucleophile and the leaving group are positioned about 180° from one another, known as the in-line geometry (126).

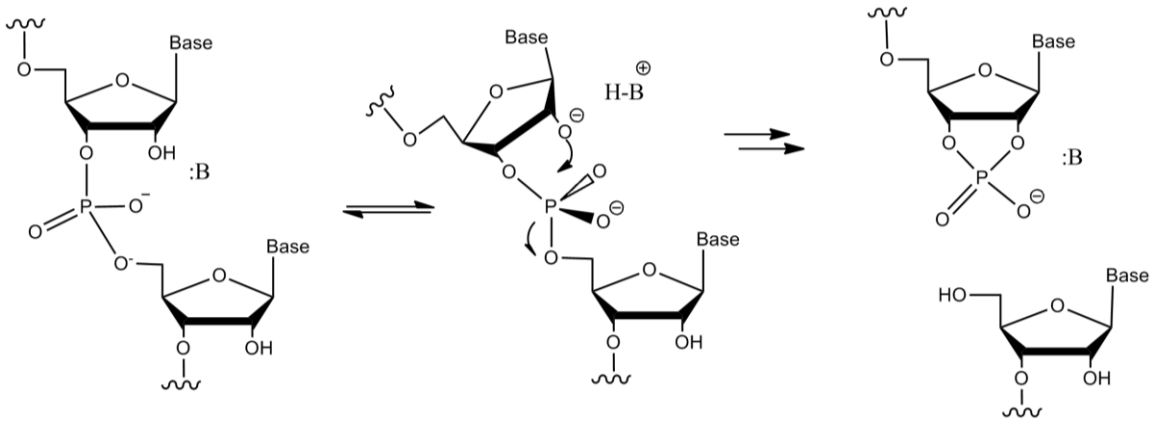

Figure 77. Possible mechanism of base-induced cleavage of RNA. Figure adapted from (126).

Cations with a low pK_a of their hydrates are known to cleave RNA better than cations with higher pK_as (128). Single-stranded regions in RNA are more spontaneously cleaved by this mechanism (100-fold more effectively than double-stranded regions), because they can more frequently sample the in-line conformation that is required for this cleavage (129). While it is not clear that metal-induced in-line cleavage of RNA can be used as a probe for atoms involved in metal ion coordination or importance of certain metals in RNA folding and function, it is believed that in-line cleavage may be able to provide clues about the location of some metal ions. Mg^{2+}-induced cleavage sites in

P5abc, a subdomain of P4-P6 RNA, were not all found to correspond to metal-binding sites in P4-P6 RNA as determined by the X-ray crystal structure (129). It was proposed that metal ions might associate with RNA and alter tertiary structure in a manner that generates linkage conformations favoring in-line attack, allowing for the observation of cleavage sites that are not in close proximity to the metal-binding sites (129). So while in-line cleavage may be useful for determining whether two metals (Mg^{2+} and $Fe^{2+)}$ can induce similar changes in a large RNA, indicating that they possibly interact at the same sites, there is no conclusive evidence that all spontaneous RNA cleavage sites actually reside near metal-ion binding pockets (130,131).

Experimental Methods

Materials

Nuclease free water (IDT) was used in all experiments involving RNA. Fe^{2+} solutions were prepared using $FeSO_4$-7 H_2O (J.T. Baker). Mg^{2+} solutions were prepared using $MgSO_4$ (Fisher Scientific). DCTA stock solutions were prepared by titrating a solution of DCTA (Sigma-Aldrich, CAS# 13291-61-7) with sodium hydroxide to pH 7. HEPES-TRIS stock buffer solutions were prepared by mixing solutions of HEPES free acid and TRIS free base in H_2O to achieve pH 7.2. Metals were removed from RNA using divalent cation chelation beads (Hampton Research). a-rRNA was synthesized and purified as previously described. 5'-[6[Carboxyfluorescein]-labeled DNA oligonucleotide primers were obtained from Eurofins MWG Operon. Hi-Di Formamide and Performance Optimized Polymer-4 used for Capillary Electrophoresis were obtained from Applied

Biosystems. SuperScript III Reverse Transcriptase for RT reactions was purchased from Invitrogen.

Reaction Conditions

All cleavage reactions were performed within a Coy anaerobic chamber in an atmosphere of 95% argon and 5% hydrogen. Reactions were performed in 20 mM Tris-Hepes buffer, pH 7.2.

Sample preparation

RNA samples were lyophilized in buffer, transferred to the Coy chamber as powders, resuspended in degassed H_2O inside the chamber. Fe^{2+} and Mg^{2+} solutions were prepared by dissolving a known mass of $FeSO_4$-$7H_2O$ or $MgSO_4$ salt in degassed H_2O inside the Coy chamber. Mg^{2+} or Fe^{2+} was added to the RNA in a 37 °C heating block to initiate the reaction. DCTA (chelator) was added to the control samples with no divalent metals. Samples were removed at various timepoints, and divalent chelation beads were added to quench the reactions. Chelation beads were removed using spin columns, prior to running RNA cleavage products on gels or reverse transcription reactions. The final reaction conditions, unless otherwise specified, were: Mg^{2+} or Fe^{2+}, 1 mM; DCTA, 1 mM; HEPES-TRIS, 20 mM, 37 °C. The nucleic acid (a-rRNA) concentration used was 0.13 μM (80 μM in nucleotides).

<u>Reverse transcription reactions</u>

Reverse transcription (RT) reactions were used to obtain labeled cDNA fragments from the RNA cleavage products. Four different 5'-[6-FAM]-labeled DNA

oligonucleotides (Eurofins MWG Operon) were used. Each helix in parenthesis either contains or succeeds the primer binding site on a-rRNA.

5'-TGCCCGTGGCGGATAGAGAC-3' (helix 73),

5'-ACATCGAGGTGCCAAACCGCC-3' (helix 89),

5'-GTTCAATTTCACCGGGTCCCTCG-3' (helix 61)

5'-CGTTACTCATGCCGGCATTCGC-3' (helix 26).

Cleaved RNA (20 μL) was added to 8 pmol of each primer in 10 mL of TE buffer. Samples were heated at 95 °C for 1 min, held at 65 °C for 3 min and then placed on ice. SuperScript III Reverse Transcriptase was used in RT reactions. RT buffer (19 mL) was added at 30 °C to yield final concentrations (in 50 μL) of 50 mM Tris-HCl pH 8.3, 75 mM KCl, 3 mM MgCl2, 2mM DTT and 250 mM of each dNTP. RT mixtures were heated at 55 °C for 1 min before addition of 1 μL SuperScript III RT enzyme mix (200 U). Reactions were incubated at 55 °C for 2 h and terminated by heating at 70 °C for 15 min. A sequencing control reaction of unmodified in vitro-transcribed RNA was dissolved in TE buffer. Aliquots of RNA solution were annealed to the DNA primers and RNA was sequenced by RT/chain termination using all four dideoxynucleotidetriphosphates (ddNTPs) at a ratio of 8:1 ddNTP to dNTP.

Instrumental Methods

Gel Electrophoresis

Polyacrylamide gel electrophoresis (PAGE) is used to examine the products of the cleavage reactions. 6%, 8M urea denaturing gels are stained with Sybr Green II to visualize bands.

Capillary Electrophoresis

1 μL of RT reaction mixture was mixed with 0.3 μL of ROX-labeled DNA sizing ladder (for alignment of disparate traces) and 8.7 μL of Hi-Di Formamide (Applied Biosystems) in a 96-well plate. Plates were heated at 95 °C for 5 min and the products were resolved by capillary electrophoresis using a 3130 Genetic Analyzer (Applied Biosystems) at 65 °C with a custom fluorescence calibration. The capillary array was loaded with Performance Optimized Polymer-4 (Applied Biosystems).

Data Processing

The output of a CE experiment is a series of "data traces," or electropherograms, which report fluorescence intensity values as a function of migration time. CE traces were converted into final cleavage measurements with in-house Matlab code, developed for analysis of SHAPE experiments. Seven key steps were required: (i) alignment, (ii) baseline correction, (iii) sequence assignment, (iv) peak quantification, (v) signal decay correction, (vi) background subtraction, and (vii) normalization. The procedure is fully described elsewhere (50). In all cases, RNA control cleavage reactions that had DCTA chelator added and no divalent metal, was used as the background signal.

Results

Mg^{2+} and Fe^{2+}-induced in-line cleavage of a-rRNA

PAGE analysis of cleavage products

RNA was cleaved by 1 mM Fe^{2+} over a range of time points up to 7 hours (Figure 78). Cleavage was performed in the anaerobic chamber to prevent Fe^{2+} from oxidizing to

Fe^{3+} and cleaving a-rRNA. Products were run on a gel to observe fragments. The extent of cleavage was observed to increase with time. Based on the gel, 3 hours was selected as the maximum length of time to be used for Fe-cleavage data.

Similarly, a-rRNA was cleaved by 1 mM Mg^{2+} in anaerobic conditions, to maintain consistency with Fe^{2+} results. Mg^{2+} cleavage was observed to proceed much slower than Fe^{2+}, so cleavage samples were taken over a range of days (Figure 79).

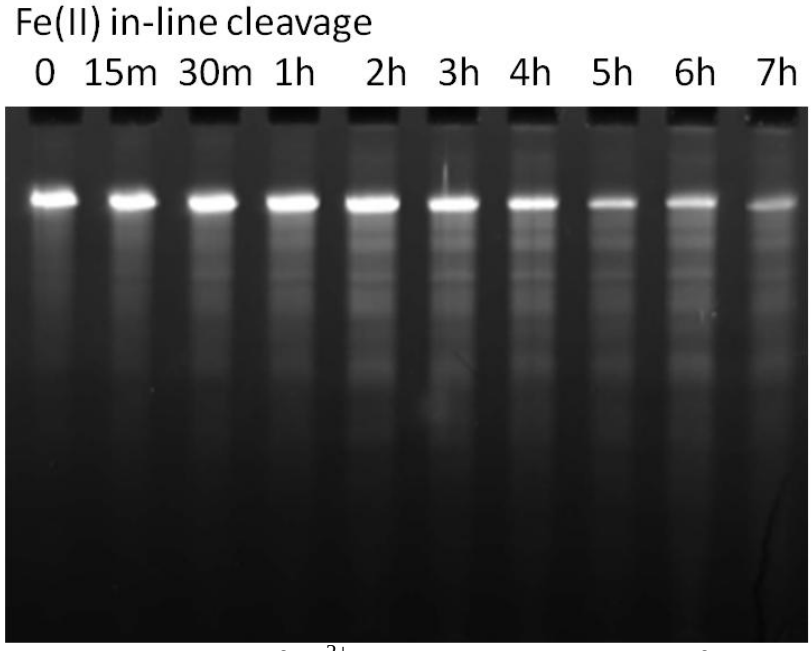

Figure 78. Products of Fe^{2+}-induced in-line cleavage of a-rRNA.

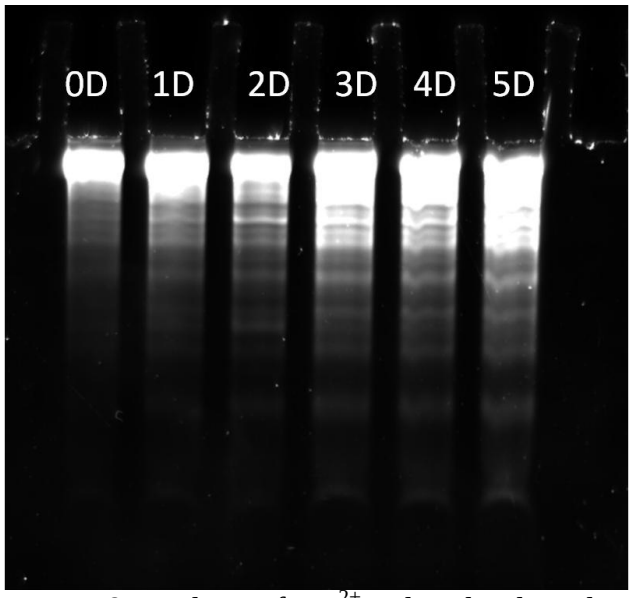

Figure 79. Products of Mg^{2+}-induced in-line cleavage of a-rRNA

Direct comparison of the PAGE-analyzed gel fragments from Mg^{2+} and Fe^{2+} cleavages revealed similarities (Figure 80).

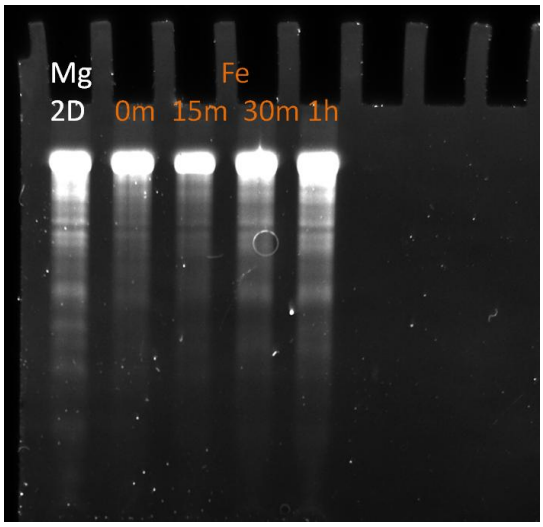

Figure 80. Mg^{2+} and Fe^{2+} in-line cleavage of a-rRNA.

Capillary electrophoresis

Three datasets were obtained for a-rRNA cleavage by each metal, corresponding to different time points of cleavage. Mg^{2+} samples were cleaved for 0 day, 1.5 day and 2 days (Figure 81). Fe^{2+}-cleaved samples were incubated for 0 min, 15 min, and 30 min (Figure 82). Cleavage products were analyzed by capillary electrophoresis. Positions of peaks indicate residue positions where cleavage occurred. No cleavage data was obtained for the last 15 residues of the 615-nucleotide a-rRNA. For all time points, controls containing DCTA and no divalent were obtained in parallel, and subtracted during the analysis. Positions of cleavage were designated as residues for which a peak was observed in at least two of the three datasets for each metal. Many sites had peaks with very low intensities, so high-intensity peaks were differentiated from low-intensity peaks, i.e. slightly above the average background signal. Twenty cleavage sites were identified for a-rRNA cleaved by each metal (Figures 80 and 81).Of these, 19 were common to both Mg^{2+} and Fe^{2+}, possibly indicating similar metal-induced in-line cleavage by the two cations (Figure 83). These sites are summarized in Table 7.

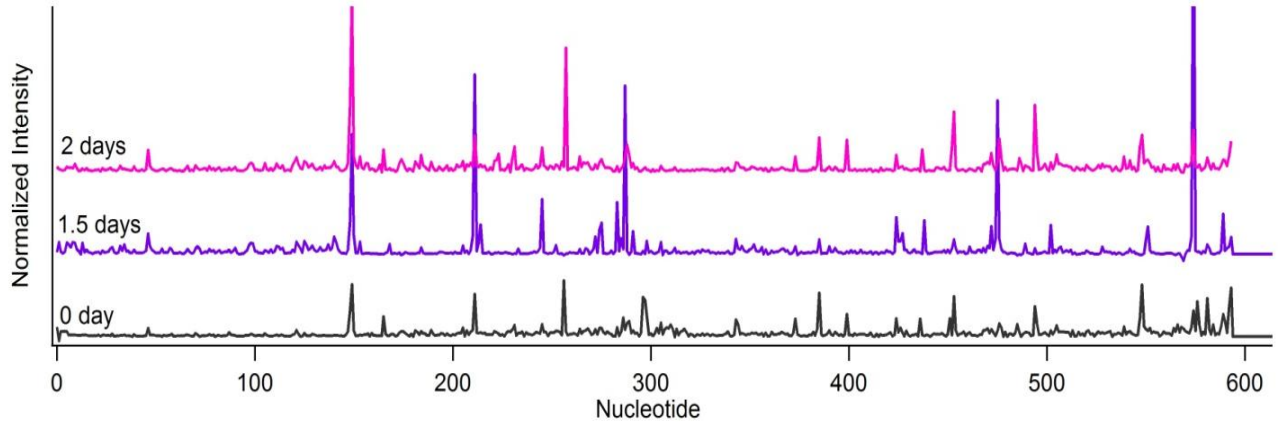

Figure 81. Analysis of Mg^{2+}-cleaved a-rRNA fragments.

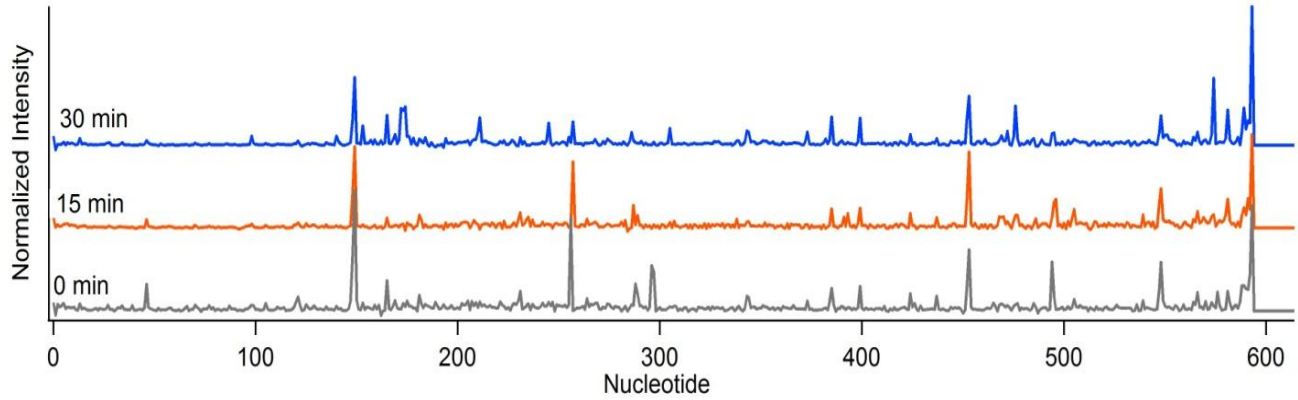

Figure 82. Analysis of Fe^{2+}-cleaved a-rRNA fragments.

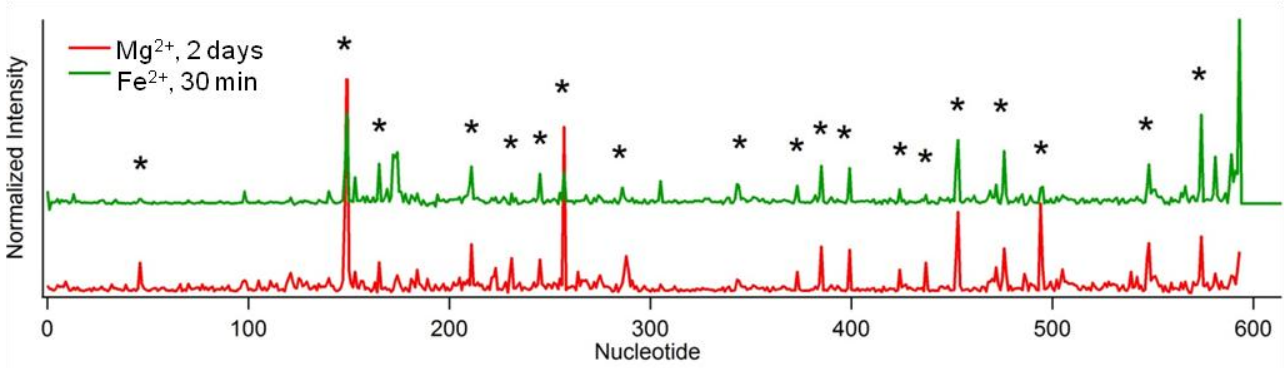

Figure 83. Comparison of Mg^{2+} and Fe^{2+} cleaved a-rRNA. Asterisks (*) indicate positions of cleavage that are common to both metals.

Table 7. Sites of Mg^{2+}- and Fe^{2+}- induced in-line cleavage of a-rRNA. Uppercase X is used to indicate sites with prominent peaks, while lowercase x is used to indicate sites where low peaks (slightly above background) are observed.

Residues	**Mg^{2+}**			**Fe^{2+}**		
	0D	**1.5D**	**2D**	**0 min**	**15min**	**30min**
46	x	X	X	X	x	x
149	X	X	X	X	X	X
165	X		X	X	x	X
181	x	x				
211	X	X	X			X
231			X	x	x	x
245	x	X	X			X
257	X		X	X	X	X
287	x	X	X	X	X	x
343	x	x	X	x	x	X
373	x	x	X	x		x
385	X	x	X	X	X	X
399	X		X	X	X	X
424	x	X	X	x	x	x
437	x	X	X	x	x	
453	X	x	X	X	X	X
476	x	X	X			X
494	X		X	X	X	X
505				x	x	
548	X	X	X	X	X	X
574	X	X	X	x	x	X

Discussion

Mg^{2+} and Fe^{2+} cleave at similar sites

In-line cleavage has been used extensively to probe RNA structure (126), but in a more limited capacity to probe metal ion binding sites. Such experiments are motivated by the idea that strong metal ion-induced cleavage suggests the presence of specific metal ion-binding sites, with residues involved in metal coordination in close proximity to the

site of cleavage. Because it is not always the case that i) RNA cleavage events correspond to the abstraction of a proton from a 2'-OH group near the metal ion; ii) RNA groups will act as ligands for a metal ion they are coordinated to, and iii) metal ions are even able to coordinate a water molecule correctly, precisely positioning it for cleavage, it is important to interpret results from in-line cleavage experiments with caution.

We observe specific positions of cleavage with both Mg^{2+} and Fe^{2+}. PAGE analysis of the cleavage products shows that Fe^{2+} is more reactive in the cleavage reaction than Mg^{2+}. This result is consistent with computational data that shows that Fe^{2+} is better than Mg^{2+} at activating the phosphorous atoms of RNA to nucleophilic attack, an increase in activation that is attributed to the accessibility of the d-orbitals of Fe^{2+} (30). It is also consistent with predictions from the mechanism of in-line cleavage, that Fe^{2+} which has a lower pK_a of its hydrate compared to Mg^{2+} (Fe^{2+} 6.0 – 6.7, Mg^{2+} 11.4) cations with lower pK_a of their hydrates will cleave RNA better than Mg^{2+}.

Cleavage fragments visualized by PAGE reveal nearly identical banding patterns with smaller bands that increase as a function of time, indicating the appearance of more cleavage product with time. This is a confirmation that there is more product appearing, useful knowledge because the CE analysis data does not provide reliable quantitative information.

A comparison of observed cleavage sites in Mg^{2+} and Fe^{2+} reveal many similarities. Both metals show 19 out of 20 cleavage sites in common (Figure 83). Similarities are observed when low-magnitude peaks are taken into account. The analysis method does not allow for reliable quantification of cleavage products, so a qualitative approach is applied to this data. The differences in peak magnitude is not taken into

account, as much as the position of the peak, which indicates a site of cleavage. The observation of a high fraction of peaks at the same positions indicates similar cleavage patterns for Fe^{2+} and Mg^{2+}.

A cautious interpretation of this data is that Mg^{2+} and Fe^{2+} might be potentially interacting at some similar sites in a-rRNA, inducing cleavage around those sites. These findings are consistent with SHAPE experiments probing the structure of a-rRNA in the presence of Mg^{2+} or Fe^{2+}. The SHAPE experiments reveal similar secondary structure in the presence of both metals (unpublished data). Unfortunately the lack of three-dimensional structural information for a-rRNA poses a limitation in drawing further conclusions from these experiments.

A known structure of a-rRNA with identified Mg^{2+} binding sites would be useful for confirming whether the cleavage sites identified in these experiments are meaningful with regards to actual Mg^{2+}-binding sites. Figure 84 shows the Mg^{2+} ions as observed in the *T. thermophilus* crystal structure overlaid on the a-rRNA secondary structure (pink circles). While these positions only provide, at best, an approximation for the metal-ion binding sites in a-rRNA, we see that only ~55% of the cleavage sites (Figure 84, blue circles) are seen to be within at least 3 nucleotides of a Mg^{2+} ion. Therefore it appears unlikely that these in-line cleavage experiments are reporting on metal ion binding sites in a-rRNA.

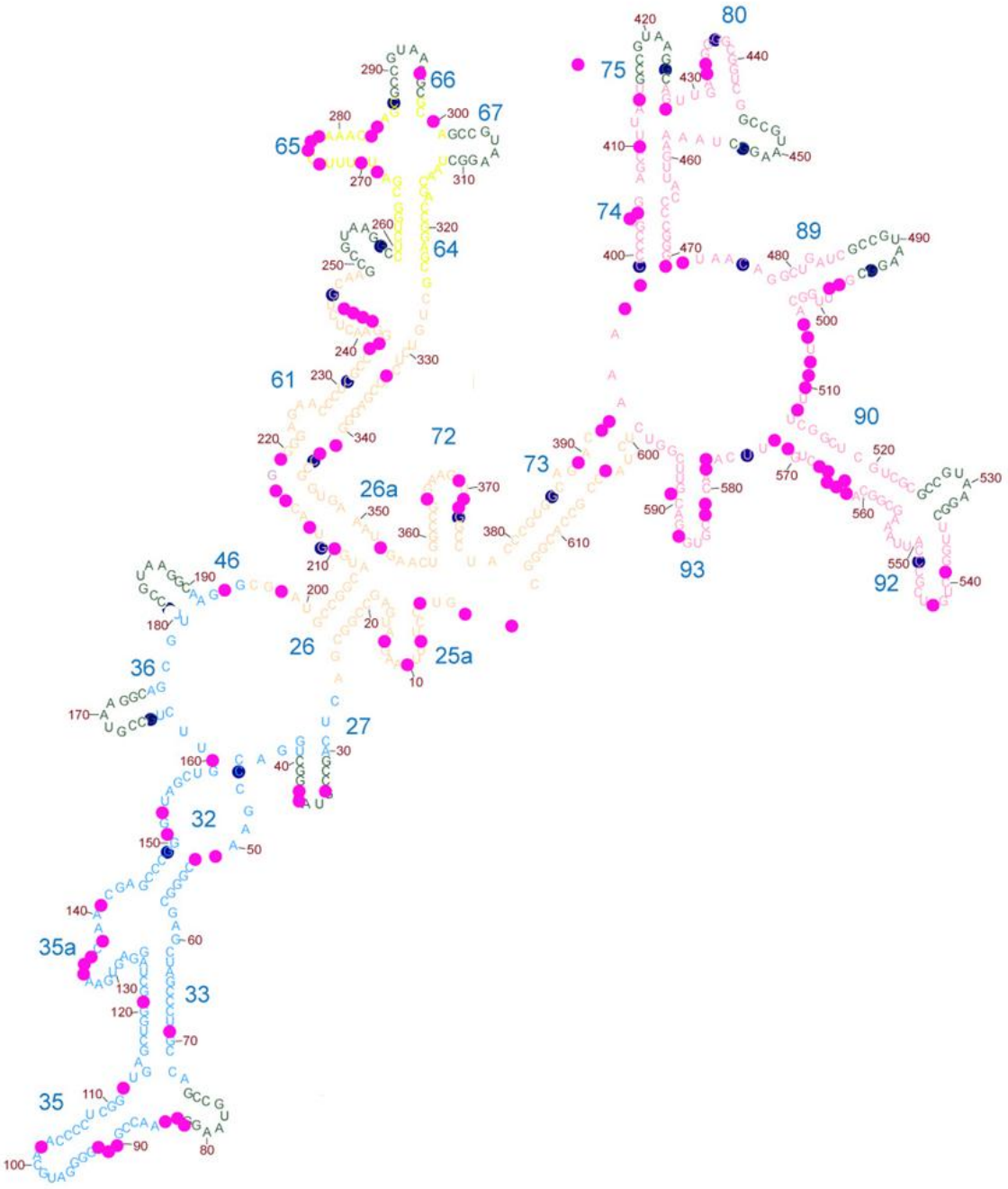

Figure 84. Secondary structure of a-rRNA showing cleavage sites and predicted Mg^{2+} binding sites. Residues within 2.4Å of Mg^{2+} in *T. thermophilus* are colored pink, cleavage sites obtained in Mg^{2+} and Fe^{2+} cleavage are colored blue.

Concluding Remarks

This work provides evidence of similar Mg^{2+} and Fe^{2+} binding sites in a-rRNA, resulting in the observation of similar cleavage sites. Future work will be required to obtain reliable identification of metal-ion binding sites in a-rRNA. This would confirm the findings of these experiments, and show the accuracy and usefulness of metal-induced cleavage as a probe for metal ion binding sties.

Additionally, the use of other metals such as Pb^{2+} and Tb^{3+}, both of which have been used extensively in in-line cleavage assays, could be useful as a control reaction. The underlying hypothesis of this work is that Mg^{2+} and Fe^{2+} compete for the same binding sites because they perform similar functions with RNA and have similar ionic properties. By this line of reasoning, Pb^{2+} and Tb^{3+} which have vastly different properties than Mg^{2+} or Fe^{2+}, may not compete in the same way for binding to RNA.

Another beneficial experiment would be to analyze the cleavage fragments from the gel. Corresponding bands between Mg^{2+} and Fe^{2+}-cleavage experiments could be excised from the gel, reverse transcribed (using poly(A) tails and poly(T) primer), and sequenced to confirm that they are the actually the same product. This would be a useful control for confirming that the products of in-line cleavage using both metals are the same.

Finally, cleavage experiments have been previously performed by folding the RNA in the presence of Mg^{2+}, and adding a cleavage-inducing metal ion to displace Mg^{2+} from high-affinity binding sites (126). This method may be useful in future experiments for confirming that Fe^{2+} and Mg^{2+} compete for the same binding sites in RNA, and identification of these sites.

CHAPTER SEVEN

CONCLUSION AND FUTURE OUTLOOK

RNA and Mg^{2+}

In this work, I have used circular dichroism to show that RNA helical regions have what appear to be slightly different structures in the presence of sodium or magnesium. Distinct CD signatures were observed for the different forms. I have also showed that helical regions of larger RNAs with complex tertiary interactions also display differences between sodium and magnesium forms. Future work will be useful for investigating the CD signatures obtained for RNA duplexes in the presence of different cations. In addition, detailed studies on the CD signatures associated with various sub-classes of A-form RNA (e.g. A'-RNA) will be beneficial. If these features of different A-form RNA conformations could be identified and assigned, it could become possible to identify the specific conformations present in duplex RNA in the presence of different cations. My work illustrates the importance of looking at *difference* CD spectra in addition to the actual CD data. The difference spectra have revealed distinct features of RNA and differences between sodium and magnesium forms that would not have been observed in the regular spectra.

This work also highlights the need for further structural investigations of RNA duplexes with different cations. Crystallography (64,65), NMR studies (77), anomalous small angle x-ray scattering (132,133)and molecular dynamics simulations (134,135) have revealed binding preferences for different cations in RNA duplexes. More detailed work could potentially reveal the helical changes that occur in RNA duplexes in the

presence of different counterions. This is important for understanding what the observed CD changes in this work correspond to.

RNA and Fe^{2+}

Certain RNAs gain oxidoreductase ability when in combination with Fe^{2+}. These results, obtained under early earth conditions, have important implications for the RNA world hypothesis. They also provided a number of unanswered questions that could be promising for future investigations. For example, the specific requirements in RNAs that make them catalytic are not completely known or understood. Future work will need to be performed to understand the mechanism by which RNA-Fe^{2+} complexes catalyze oxidoreduction.

Kinetic investigations of catalytic RNAs revealed that not all the RNAs follow Michaelis-Menten kinetics. Further work will be useful for understanding why some RNAs possess activity that saturates with increasing substrate concentration while others do not display any correlation between initial velocity and substrate concentration. The investigation of a large number of diverse RNAs in this assay could be useful for this purpose. In addition, different K_m values in the different RNAs suggest a difference in 'substrate-binding' by the enzymatic complex. It is not clear whether the substrates (TMB and/or H_2O_2) are actually binding to the RNA during catalysis. Investigation of the nature of the interaction between the enzymatic complex and substrates could reveal important mechanistic information about this reaction, as well as potentially allow for *a* priori identification of catalytic RNAs.

This work emphasizes the importance of performing experiments aimed understanding the origin of life under early earth conditions. It is possible that close

association of biological macromolecules with Fe^{2+} may have been a critical determinant in the establishment and development of the current system of RNA, DNA and protein, possibly during the RNA world (24,136-141). This work hints at the need for further investigations of RNA-Fe^{2+} complexes. Oxidoreduction using the peroxidase assay has been investigated, but there are many other types of redox reactions that could be investigated. Catalytic activity other than oxidoreduction should also be investigated as these could provide important hints about the types of reactions that were present on early earth.

Several protein enzymes that process nucleic acids use Mg^{2+} or other divalent metals as cofactors. Metals are known to be mobile and intererchangeable within enzymes. For these reasons, it could be highly beneficial to perform a reverse Mg^{2+} to Fe^{2+} substitution in nucleic acid processing enzymes and test for enzymatic activity under early earth conditions. This could lend support to the hypothesis that the GOE drove Fe^{2+} replacement by Mg^{2+}, Mn^{2+} and other metals in protein enzymes as the primary divalent cation for facilitating folding, catalysis and processing of nucleic acids.

REFERENCES

1. Bowman, J.C., Lenz, T.K., Hud, N.V. and Williams, L.D. (2012) Cations in charge: magnesium ions in RNA folding and catalysis. *Current Opinion in Structural Biology*, **22**, 262-272.
2. Draper, D.E. (2004) A guide to ions and RNA structure. *RNA*, **10**, 335-343.
3. Lipfert, J., Doniach, S., Das, R. and Herschlag, D. (2014) Understanding nucleic acid–ion interactions. *Annual Review of Biochemistry*, **83**, 813-841.
4. Cole, P.E. and Crothers, D.M. (1972) Conformational changes of transfer ribonucleic acid. Relaxation kinetics of the early melting transition of methionine transfer ribonucleic acid (*Escherichia coli*). *Biochemistry*, **11**, 4368-4374.
5. Romer, R. and Hach, R. (1975) tRNA conformation and magnesium binding. A study of a yeast phenylalanine-specific tRNA by a fluorescent indicator and differential melting curves. *European Journal of Biochemistry*, **55**, 271-284.
6. Stein, A. and Crothers, D.M. (1976) Conformational changes of transfer RNA. The role of magnesium(II). *Biochemistry*, **15**, 160-168.
7. Cech, T.R. and Bass, B.L. (1986) Biological Catalysis by RNA. *Annual Review of Biochemistry*, **55**, 599-629.
8. Dahm, S.C. and Uhlenbeck, O.C. (1991) Role of divalent metal ions in the hammerhead RNA cleavage reaction. *Biochemistry*, **30**, 9464-9469.
9. Westheimer, F.H. (1987) Why nature chose phosphates. *Science*, **235**, 1173-1178.
10. Hsiao, C., Tannenbaum, M., VanDeusen, H., Hershkovitz, E., Perng, G., Tannenbaum, A. and Williams, L.D. (2008) In Hud, N. (ed.), *Nucleic Acid Metal Ion Interactions*. The Royal Society of Chemistry, London, pp. 1-35.
11. Brown, I.D. (1988) What Factors Determine Cation Coordination Numbers. *Acta Crystallographica Section B.*, **44**, 545-553.
12. Brown, I.D. (1992) Chemical and steric constraints in inorganic solids. *Acta Crystallographica Section B.*, **48**, 553-572.
13. Bock, C.W., Katz, A.K., Markham, G.D. and Glusker, J.P. (1999) Manganese as a replacement for magnesium and zinc: Functional comparison of the divalent ions. *Journal of the American Chemical Society*, **121**, 7360-7372.
14. Rashin, A.A. and Honig, B. (1985) Reevaluation of the Born model of ion hydration. *Journal of Physical Chemistry*, **89**, 5588-5593.
15. Cate, J.H., Hanna, R.L. and Doudna, J.A. (1997) A magnesium ion core at the heart of a ribozyme domain. *Nature Structural Biology*, **4**, 553-558.
16. Ban, N., Nissen, P., Hansen, J., Moore, P.B. and Steitz, T.A. (2000) The complete atomic structure of the large ribosomal subunit at 2.4 Å resolution. *Science*, **289**, 905-920.

17. Klein, D.J., Moore, P.B. and Steitz, T.A. (2004) The contribution of metal ions to the structural stability of the large ribosomal subunit. *RNA*, **10**, 1366-1379.

18. Juneau, K., Podell, E., Harrington, D.J. and Cech, T.R. (2001) Structural basis of the enhanced stability of a mutant ribozyme domain and a detailed view of RNA--solvent interactions. *Structure.*, **9**, 221-231.

19. Toor, N., Keating, K.S., Taylor, S.D. and Pyle, A.M. (2008) Crystal structure of a self-spliced group II intron. *Science*, **320**, 77-82.

20. Robertson, M.P. and Scott, W.G. (2007) The structural basis of ribozyme-catalyzed RNA assembly. *Science*, **315**, 1549-1553.

21. Hsiao, C. and Williams, L.D. (2009) A recurrent magnesium-binding motif provides a framework for the ribosomal peptidyl transferase center. *Nucleic Acids Res*, **37**, 3134-3142.

22. Selmer, M., Dunham, C.M., Murphy, F.V., Weixlbaumer, A., Petry, S., Kelley, A.C., Weir, J.R. and Ramakrishnan, V. (2006) Structure of the 70S ribosome complexed with mRNA and tRNA. *Science*, **313**, 1935-1942.

23. Petrov, A.S., Bowman, J.C., Harvey, S.C. and Williams, L.D. (2011) Bidentate RNA-magnesium clamps: on the origin of the special role of magnesium in RNA folding. *RNA*, **17**, 291-297.

24. Crick, F.H. (1968) The origin of the genetic code. *Journal of Molecular Biology*, **38**, 367-379.

25. Orgel, L.E. (1968) Evolution of the genetic apparatus. *Journal of Molecular Biology*, **38**, 381-393.

26. Anbar, A.D. (2008) Oceans. Elements and Evolution. *Science*, **322**, 1481-1483.

27. Hazen, R.M. and Ferry, J.M. (2010) Mineral evolution: Mineralogy in the fourth dimension. *Elements*, **6**, 9-12.

28. Klein, C. (2005) Some Precambrian banded iron-formations (BIFs) from around the world: Their age, geologic setting, mineralogy, metamorphism, geochemistry, and origin. *American Mineralogist*, **90**, 1473-1499.

29. Johnson, C.M., Beard, B.L. and Roden, E.E. (2008) The iron isotope fingerprints of redox and biogeochemical cycling in modern and ancient earth. *Annual Review of Earth and Planetary Sciences*, **36**, 457-493.

30. Athavale, S.S., Petrov, A.S., Hsiao, C., Watkins, D., Prickett, C.D., Gossett, J.J., Lie, L., Bowman, J.C., O'Neill, E., Bernier, C.R. *et al.* (2012) RNA folding and catalysis mediated by iron (II). *PLoS ONE*, **7**, e38024.

31. Berens, C., Streicher, B., Schroeder, R. and Hillen, W. (1998) Visualizing metal-ion-binding sites in group I introns by iron(II)-mediated Fenton reactions. *Chem Biol*, **5**, 163-175.

32. Vicens, Q., Gooding, A.R., Laederach, A. and Cech, T.R. (2007) Local RNA structural changes induced by crystallization are revealed by SHAPE. *RNA-Publ. RNA Soc.*, **13**, 536-548.

33. Scott, W.G. (2007) Ribozymes. *Current Opinion in Structural Biology*, **17**, 280-286.

34. Solomon, E.I., Decker, A. and Lehnert, N. (2003) Non-heme iron enzymes: Contrasts to heme catalysis. *Proceedings of the National Academy of Sciences*, **100**, 3589-3594.

35. Poulos, T.L. (2014) Heme enzyme structure and function. *Chemical Reviews*, **114**, 3919-3962.

36. Sen, D. and Poon, L.C. (2011) RNA and DNA complexes with hemin [Fe(III) heme] are efficient peroxidases and peroxygenases: how do they do it and what does it mean? *Critical reviews in biochemistry and molecular biology*, **46**, 478-492.

37. Sydor, P.K. and Challis, G.L. (2012) In David, A. H. (ed.), *Methods in Enzymology*. Academic Press, Vol. Volume 516, pp. 195-218.

38. Abu-Omar, M.M., Loaiza, A. and Hontzeas, N. (2005) Reaction mechanisms of mononuclear non-heme iron oxygenases. *Chemical Reviews*, **105**, 2227-2252.

39. Sanvisens, N., Bañó, M.C., Huang, M. and Puig, S. Regulation of ribonucleotide reductase in response to iron deficiency. *Molecular Cell*, **44**, 759-769.

40. Ellington, A.D. and Szostak, J.W. (1990) In vitro selection of RNA molecules that bind specific ligands. *Nature*, **346**, 818-822.

41. Li, Y., Geyer, R. and Sen, D. (1996) Recognition of anionic porphyrins by DNA aptamers. *Biochemistry*, **35**, 6911-6922.

42. Conn, M.M., Prudent, J.R. and Schultz, P.G. (1996) Porphyrin metalation catalyzed by a small rna molecule. *Journal of the American Chemical Society*, **118**, 7012-7013.

43. Travascio, P., Bennet, A.J., Wang, D.Y. and Sen, D. A ribozyme and a catalytic DNA with peroxidase activity: active sites versus cofactor-binding sites. *Chemistry & Biology*, **6**, 779-787.

44. Poon, L.C.H., Methot, S.P., Morabi-Pazooki, W., Pio, F., Bennet, A.J. and Sen, D. (2011) Guanine-Rich RNAs and DNAs that bind heme robustly catalyze oxygen transfer reactions. *Journal of the American Chemical Society*, **133**, 1877-1884.

45. Yarus, M. (2002) PRIMORDIAL GENETICS: Phenotype of the Ribocyte. *Annual Review of Genetics*, **36**, 125-151.

46. Murphy, F.L. and Cech, T.R. (1993) An independently folding domain of RNA tertiary structure within the Tetrahymena ribozyme. *Biochemistry*, **32**, 5291-5300.

47. Murphy, F.L. and Cech, T.R. (1994) GAAA Tetraloop and Conserved Bulge Stabilize Tertiary Structure of a Group I Intron Domain. *Journal of Molecular Biology*, **236**, 49-63.

48. Harms, J., Schluenzen, F., Zarivach, R., Bashan, A., Gat, S., Agmon, I., Bartels, H., Franceschi, F. and Yonath, A. (2001) High resolution structure of the large ribosomal subunit from a mesophilic eubacterium. *Cell*, **107**, 679-688.

49. Hsiao, C., Lenz, T.K., Peters, J.K., Fang, P.Y., Schneider, D.M., Anderson, E.J., Preeprem, T., Bowman, J.C., O'Neill, E.B., Lie, L. *et al.* (2013) Molecular paleontology: a biochemical model of the ancestral ribosome. *Nucleic Acids Research*, **41**, 3373-3385.

50. Athavale, S.S., Gossett, J.J., Hsiao, C., Bowman, J.C., O'Neill, E., Hershkovitz, E., Preeprem, T., Hud, N.V., Wartell, R.M., Harvey, S.C. *et al.* (2012) Domain III of the *T. thermophilus* 23S rRNA folds independently to a near-native state. *RNA*, **18**, 752-758.

51. Petrov, A.S., Bernier, C.R., Hershkovitz, E., Xue, Y., Waterbury, C.C., Grover, M.A., C., H.S., Hud, N.V., Wartell, R.M. and Williams, L.D. (2013) Secondary structure and domain architecture of the 23S rRNA. *Nucleic Acids Research*, **41**, 7522-7535.

52. Lanier, K.A., Athavale, S.S., Anderson, E., Roy, P., Schneider, D.M., Hsiao, C., Petrov, A.S., Bowman, J.C., O'Neill, E.B., Abdurahiman, N. *et al.* (2015) Interactions of rRNA with an ancient protein fragment. *submitted*.

53. Holbrook, S.R., Sussman, J.L., Warrant, R.W., Church, G.M. and Kim, S.H. (1977) RNA-ligant interactions. (I) Magnesium binding sites in yeast tRNAPhe. *Nucleic Acids Research*, **4**, 2811-2820.

54. Athavale, S.S., Gossett, J.J., Bowman, J.C., Hud, N.V., Williams, L.D. and Harvey, S.C. (2013) In vitro secondary structure of the genomic RNA of satellite tobacco mosaic virus. *PLoS One*, **8**, e54384.

55. Stiborová, M., Mikšanová, M., Havlíček, V.r., Schmeiser, H.H. and Frei, E. (2002) Mechanism of peroxidase-mediated oxidation of carcinogenic o-anisidine and its binding to DNA. *Mutation Research/Fundamental and Molecular Mechanisms of Mutagenesis*, **500**, 49-66.

56. Josephy, P.D., Eling, T. and Mason, R.P. (1982) The horseradish peroxidase-catalyzed oxidation of 3,5,3',5'-tetramethylbenzidine. Free radical and charge-transfer complex intermediates. *Journal of Biological Chemistry*, **257**, 3669-3675.

57. Fornera, S. and Walde, P. (2010) Spectrophotometric quantification of horseradish peroxidase with o-phenylenediamine. *Analytical Biochemistry*, **407**, 293-295.

58. Kadnikova, E.N. and Kostić, N.M. (2002) Oxidation of ABTS by hydrogen peroxide catalyzed by horseradish peroxidase encapsulated into sol–gel glass.: Effects of glass matrix on reactivity. *Journal of Molecular Catalysis B: Enzymatic*, **18**, 39-48.

59. Pütter, J. and Becker, R. Methods of enzymatic analysis. 3rd edn.. Bergmeyer, HU., editor. *Vol. III. Chemie*, 286-293.

60. Bowman, J.C., Azizi, B., Lenz, T.K., Roy, P. and Williams, L.D. (2012) In Conn, G. L. (ed.), *Recombinant and In Vitro RNA Synthesis: Methods and Protocols, Methods in Molecular Biology*. Springer Science, LLC, Vol. 941, pp. 19-41.

61. Hsiao, C., Chou, I.-C., Okafor, C.D., Bowman, J.C., O'Neill, E.B., Athavale, S.S., Petrov, A.S., Hud, N.V., Wartell, R.M., Harvey, S.C. *et al.* (2013) Iron(II) plus RNA can catalyze electron transfer. *Nature Chemistry*, **5**, 525-528.

62. Lynch, D.C. and Schimmel, P.R. (1974) Cooperative binding of magnesium to transfer ribonucleic acid studied by a fluorescent probe. *Biochemistry*, **13**, 1841-1852.

63. Lindahl, T., Adams, A. and Fresco, J.R. (1966) Renaturation of transfer ribonucleic acids through site binding of magnesium. *Proceedings of the National Academy of Sciences. U. S. A.*, **55**, 941-948.

64. Robinson, H., Gao, Y.-G., Sanishvili, R., Joachimiak, A. and Wang, A.H.J. (2000) Hexahydrated magnesium ions bind in the deep major groove and at the outer mouth of A-form nucleic acid duplexes. *Nucleic Acids Research*, **28**, 1760-1766.

65. Ennifar, E., Walter, P. and Dumas, P. (2003) A crystallographic study of the binding of 13 metal ions to two related RNA duplexes. *Nucleic Acids Research*, **31**, 2671-2682.

66. Tsukiji, S., Pattnaik, S.B. and Suga, H. (2004) Reduction of an aldehyde by a NADH/Zn2+ -dependent redox active ribozyme. *Journal of American Chemical Society*, **126**, 5044-5045.

67. Sen, D. and Poon, L.C.H. (2011) RNA and DNA complexes with hemin [Fe(III) heme] are efficient peroxidases and peroxygenases: how do they do it and what does it mean? *Critical reviews in biochemistry and molecular biology*, **46**, 478-492.

68. Aguirre, J.D. and Culotta, V.C. (2012) Battles with iron: manganese in oxidative stress protection. *Journal of Biological Chemistry*, **287**, 13541-13548.

69. Ushizaka, S., Kuma, K. and Suzuki, K. (2011) Effects of Mn and Fe on growth of a coastal marine diatom Talassiosira weissflogii in the presence of precipitated Fe(III) hydroxide and EDTA-Fe(III) complex. *Fish. Sci.*, **77**, 411-424.

70. Martin, J.E. and Imlay, J.A. (2011) The alternative aerobic ribonucleotide reductase of Escherichia coli, NrdEF, is a manganese-dependent enzyme that enables cell replication during periods of iron starvation. *Molecular Microbiology*, **80**, 319-334.

71. Cotruvo, J.A. and Stubbe, J. (2011) Class I ribonucleotide reductases: metallocofactor assembly and repair in vitro and in vivo. *Annual Review of Biochemistry*, **80**, 733-767.

72. Anjem, A., Varghese, S. and Imlay, J.A. (2009) Manganese import is a key element of the OxyR response to hydrogen peroxide in Escherichia coli. *Molecular Microbiology*, **72**, 844-858.

73. Wolfe-Simon, F., Starovoytov, V., Reinfelder, J.R., Schofield, O. and Falkowski, P.G. (2006) Localization and role of manganese superoxide dismutase in a marine diatom. *Plant physiology*, **142**, 1701-1709.

74. Jordan, A. and Reichard, P. (1998) Ribonucleotide reductases. *Annual Review of Biochemistry*, **67**, 71-98.

75. Zivarts, M., Liu, Y. and Breaker, R.R. (2005) Engineered allosteric ribozymes that respond to specific divalent metal ions. *Nucleic Acids Res*, **33**, 622-631.

76. Lavery, R. and Pullman, B. (1981) The molecular electrostatic potential and steric accessibility of A-DNA. *Nucleic Acids Res*, **9**, 4677-4688.

77. Robinson, H. and Wang, A.H. (1996) Neomycin, spermine and hexaamminecobalt (III) share common structural motifs in converting B- to A-DNA. *Nucleic Acids Research*, **24**, 676-682.

78. Takamoto, K., Das, R., He, Q., Doniach, S., Brenowitz, M., Herschlag, D. and Chance, M.R. (2004) Principles of RNA compaction: insights from the equilibrium folding pathway of the P4-P6 RNA domain in monovalent cations. *Journal of Molecular Biology*, **343**, 1195-1206.

79. Koculi, E., Cho, S.S., Desai, R., Thirumalai, D. and Woodson, S.A. (2012) Folding path of P5abc RNA involves direct coupling of secondary and tertiary structures. *Nucleic Acids Research*, **40**, 8011-8020.

80. Zheng, M., Wu, M. and Tinoco, I. (2001) Formation of a GNRA tetraloop in P5abc can disrupt an interdomain interaction in the Tetrahymena group I ribozyme. *Proceedings of the National Academy of Sciences*, **98**, 3695-3700.

81. Silverman, S.K. and Cech, T.R. (1999) RNA tertiary folding monitored by fluorescence of covalently attached pyrene. *Biochemistry*, **38**, 14224-14237.

82. Pabit, S.A., Sutton, J.L., Chen, H. and Pollack, L. (2013) The role of ion valence in the submillisecond collapse and folding of a small RNA domain. *Biochemistry*, **52**, 1539-1546.

83. Wu, M. and Tinoco, I. (1998) RNA folding causes secondary structure rearrangement. *Proceedings of the National Academy of Sciences of the United States of America*, **95**, 11555-11560.

84. Treiber, D.K., Rook, M.S., Zarrinkar, P.P. and Williamson, J.R. (1998) Kinetic Intermediates Trapped by Native Interactions in RNA Folding. *Science*, **279**, 1943-1946.

85. Den Boef, G. and Poeder, B.C. (1964) Spectrophotometric determination of chromium(iii) with complexans. *Analytica Chimica Acta*, **30**, 261-268.

86. Glentworth, P., Wiseall, B., Wright, C.L. and Mahmood, A.J. (1968) A kinetic study of isotopic exchange reactions between lanthanide ions and lanthanide polyaminopolycarboxylic acid complex ions—I isotopic exchange reactions of Ce(III) with Ce(HEDTA), Ce(EDTA)−, Ce(DCTA)− and Ce(DTPA)2−. *Journal of Inorganic and Nuclear Chemistry*, **30**, 967-986.

87. Huang, C.-H. (2011) *Rare earth coordination chemistry: Fundamentals and applications*. John Wiley & Sons.

88. Choppin, G.R. (1993) A half-century of lanthanide aminopolycarboxylates. *Journal of alloys and compounds*, **192**, 256-261.

89. Kirmizialtin, S., Pabit, Suzette A., Meisburger, Steve P., Pollack, L. and Elber, R. RNA and its ionic cloud: Solution scattering experiments and atomically detailed simulations. *Biophysical Journal*, **102**, 819-828.

90. Kypr, J., Kejnovská, I., Renčiuk, D. and Vorlíčková, M. (2009) Circular dichroism and conformational polymorphism of DNA. *Nucleic Acids Research*, **37**, 1713-1725.

91. Ivanov, V.I., Minchenkova, L.E., Schyolkina, A.K. and Poletayev, A.I. (1973) Different conformations of double-stranded nucleic acid in solution as revealed by circular dichroism. *Biopolymers*, **12**, 89-110.

92. Savelyev, A. and MacKerell, A.D. (2015) Differential impact of the monovalent ions Li+, Na+, K+, and Rb+ on DNA conformational properties. *The Journal of Physical Chemistry Letters*, **6**, 212-216.

93. Saenger, W. (1984) *Principles of nucleic acid structure*. Springer-Verlag, New York.

94. Silverman, S.K., Deras, M.L., Woodson, S.A., Scaringe, S.A. and Cech, T.R. (2000) Multiple folding pathways for the P4-P6 RNA domain. *Biochemistry*, **39**, 12465-12475.

95. Frederiksen, J.K., Li, N.S., Das, R., Herschlag, D. and Piccirilli, J.A. (2012) Metal-ion rescue revisited: biochemical detection of site-bound metal ions important for RNA folding. *RNA*, **18**, 1123-1141.

96. Deras, M.L., Brenowitz, M., Ralston, C.Y., Chance, M.R. and Woodson, S.A. (2000) Folding mechanism of the Tetrahymena ribozyme P4-P6 domain. *Biochemistry*, **39**, 10975-10985.

97. Uchida, T., He, Q., Ralston, C.Y., Brenowitz, M. and Chance, M.R. (2002) Linkage of monovalent and divalent ion binding in the folding of the P4-P6 domain of the Tetrahymena ribozyme. *Biochemistry*, **41**, 5799-5806.

98. Cohn, M., Danchin, A. and Grunberg-Manago, M. (1969) Proton magnetic relaxation studies of manganous complexes of transfer RNA and related compounds. *Journal of Molecular Biology*, **39**, 199-217.

99. Sander, C. and Ts'o, P.O. (1971) Interaction of nucleic acids: VIII. Binding of magnesium ions by nucleic acids. *Journal of Molecular Biology*, **55**, 1-21.

100. Shack, J. and Bynum, B.S. (1959) Determination of the interaction of deoxyribonucleate and magnesium ions by means of a metal ion indicator. *Nature*, **184**, 635-636.

101. Misra, V.K. and Draper, D.E. (2001) A thermodynamic framework for Mg^{2+} binding to RNA. *Proc. Natl. Acad. Sci. U. S. A.*, **98**, 12456-12461.

102. Grilley, D., Misra, V., Caliskan, G. and Draper, D.E. (2007) Importance of partially unfolded conformations for Mg^{2+}-lnduced folding of RNA tertiary

structure: Structural models and free energies of Mg^{2+} interactions. *Biochemistry*, **46**, 10266-10278.

103. Draper, D.E. (2008) RNA Folding: Thermodynamic and molecular descriptions of the roles of ions. *Biophysical Journal*, **95**, 5489-5495.

104. Auffinger, P., Bielecki, L. and Westhof, E. (2003) The Mg^{2+} binding sites of the 5S rRNA loop E motif as investigated by molecular dynamics simulations. *Chemistry & Biology*, **10**, 551-561.

105. Glendening, E.D. (1996) Natural energy decomposition analysis: Explicit evaluation of electrostatic and polarization effects with application to aqueous clusters of alkali metal cations and neutrals. *Journal of the American Chemical Society*, **118**, 2473-2482.

106. Glendening, E.D. and Feller, D. (1996) Dication-water interactions: $M^{2+}(H2O)_n$ clusters for alkaline earth metals M=Mg,Ca,Sr,Ba, and Ra. *Journal of Physical Chemistry*, **100**, 4790-4797.

107. Petrov, A.S., Funseth-Smotzer, J. and Pack, G.R. (2005) Computational study of dimethyl phosphate anion and its complexes with water, magnesium, and calcium. *International Journal of Quantum Chemistry*, **102**, 645-655.

108. Ditzler, M.A., Otyepka, M., Sponer, J. and Walter, N.G. (2010) Molecular dynamics and quantum mechanics of RNA: conformational and chemical change we can believe in. *Accounts of Chemical Research*, **43**, 40-47.

109. Trachtman, M., Markham, G.D., Glusker, J.P., George, P. and Bock, C.W. (1998) Interactions of Metal Ions with Water: Ab Initio Molecular Orbital Studies of Structure, Bonding Enthalpies, Vibrational Frequencies and Charge Distributions. 1. Monohydrates. *Inorganic Chemistry*, **37**, 4421-4431.

110. Munoz, J., Sponer, J., Hobza, P., Orozco, M. and Luque, F.J. (2001) Interactions of hydrated Mg^{2+} cation with bases, base pairs, and nucleotides. electron topology, natural bond orbital, electrostatic, and vibrational study. *Journal of Physical Chemistry B*, **105**, 6051-6060.

111. Gresh, N., Sponer, J.E., Spackova, N., Leszczynski, J. and Sponer, J. (2003) Theoretical study of binding of hydrated Zn(II) and Mg(II) cations to 5'-guanosine monophosphate. Toward polarizable molecular mechanics for DNA and RNA. *Journal of Physical Chemistry B*, **107**, 8669-8681.

112. Rulisek, L. and Sponer, J. (2003) Outer-shell and inner-shell coordination of phosphate group to hydrated metal ions (Mg^{2+}, Cu^{2+}, Zn^{2+}, Cd^{2+}) in the presence and absence of nucleobase. The role of nonelectrostatic effects. *Journal of Physical Chemistry B*, **107**, 1913-1923.

113. Murashov, V.V. and Leszczynski, J. (1999) Theoretical study of complexation of phosphodiester linkage with alkali and alkaline-earth cations. *Journal of Physical Chemistry B*, **103**, 8391-8397.

114. Petrov, A.S., Pack, G.R. and Lamm, G. (2004) Calculations of magnesium-nucleic acid site binding in solution. *J. Phys. Chem. B*, **108**, 6072-6081.

115. Petrov, A.S., Lamm, G. and Pack, G.R. (2005) Calculation of the binding free energy for magnesium-RNA interactions. *Biopolymers*, **77**, 137-154.

116. Frisch, M.J., Trucks, G.W., Schlegel, H.B., Scuseria, G.E., Robb, M.A., Cheeseman, J.R., Scalmani, G., Barone, V., Mennucci, B., Petersson, G.A. *et al.* (2009). Gaussian, Inc., Wallingford, CT.

117. Kim, K.S., Tarakeshwar, P. and Lee, J.Y. (2000) Molecular clusters of pi-systems: Theoretical studies of structures, spectra, and origin of interaction energies. *Chemical Reviews*, **100**, 4145-4185.

118. Barrientos, C. and Sordo, J. (2007) On the application of the counterpoise correction for the basis set superposition error in geometry optimization calculations of molecular systems: some inconsistent results. *Theoretical Chemistry Accounts,***118**, 733-738.

119. Boys, S.F. and Bernardi, F. (1970) Calculation of small molecular interactions by differences of separate total energies - some procedures with reduced errors. *Molecular Physics*, **19**, 553-566.

120. Petrov, A.S., Bernier, C.R., Hsiao, C.L., Okafor, C.D., Tannenbaum, E., Stern, J., Gaucher, E., Schneider, D., Hud, N.V., Harvey, S.C. *et al.* (2012) RNA-magnesium-protein interactions in large ribosomal subunit. *J. Phys. Chem. B*, **116**, 8113-8120.

121. Mikkola, S., Stenman, E., Nurmi, K., Yousefi-Salakdeh, E., Stromberg, R. and Lonnberg, H. (1999) The mechanism of the metal ion promoted cleavage of RNA phosphodiester bonds involves a general acid catalysis by the metal aquo ion on the departure of the leaving group. *Journal of the Chemical Society, Perkin Transactions 2*, 1619-1626.

122. Kuusela, S. and Lönnberg, H. (1996) Effect of metal ions on the hydrolytic reactions of nucleosides and their phosphoesters. *Metal ions in biological systems*, **32**, 271-271.

123. Kuusela, S. and Lönnberg, H. (1997) Metal ion dependent hydrolysis of RNA. *Current Topics in Solution Chemistry*, **2**, 29-47.

124. Morrow, J. (1996) Hydrolytic cleavage of RNA catalyzed by metal ion complexes. *Metal ions in biological systems*, **33**, 561.

125. Trawick, B.N., Daniher, A.T. and Bashkin, J.K. (1998) Inorganic mimics of ribonucleases and ribozymes: from random cleavage to sequence-specific chemistry to catalytic antisense drugs. *Chemical Reviews*, **98**, 939-960.

126. Forconi, M. and Herschlag, D. (2009) Metal ion-based RNA cleavage as a structural probe. *Methods in Enzymology*, **468**, 91-106.

127. Brown, R.S., Dewan, J.C. and Klug, A. (1985) Crystallographic and biochemical investigation of the lead(II)-catalyzed hydrolysis of yeast phenylalanine tRNA. *Biochemistry*, **24**, 4785-4801.

128. Feig, A.L. and Uhlenbeck, O.C. (1999) The role of metal ions in RNA biochemistry. *Cold Spring Harbor Monograph Archive*, **37**, 287-319.

129. Soukup, G.A. and Breaker, R.R. (1999) Relationship between internucleotide linkage geometry and the stability of RNA. *RNA-Publ. RNA Soc.*, **5**, 1308-1325.

130. Polacek, N. and Barta, A. (1998) Metal ion probing of rRNAs: evidence for evolutionarily conserved divalent cation binding pockets. *RNA (New York, N.Y.)*, **4**, 1282-1294.

131. Kazakov, S. and Altman, S. (1991) Site-specific cleavage by metal ion cofactors and inhibitors of M1 RNA, the catalytic subunit of RNase P from Escherichia coli. *Proceedings of the National Academy of Sciences of the United States of America*, **88**, 9193-9197.

132. Pabit, S.A., Qiu, X., Lamb, J.S., Li, L., Meisburger, S.P. and Pollack, L. (2009) Both helix topology and counterion distribution contribute to the more effective charge screening in dsRNA compared with dsDNA. *Nucleic Acids Res*, **37**, 3887-3896.

133. Pollack, L. (2011) SAXS studies of ion-nucleic acid interactions [Review]. *Annual review of biophysics*, **40**, 225-242.

134. Kirmizialtin, S. and Elber, R. (2010) Computational exploration of mobile ion distributions around RNA duplex. *The Journal of Physical Chemistry B*, **114**, 8207-8220.

135. Kirmizialtin, S., Silalahi, Alexander R., Elber, R. and Fenley, Marcia O. (2012) The Ionic Atmosphere around A-RNA: Poisson-Boltzmann and Molecular Dynamics Simulations. *Biophysical Journal*, **102**, 829-838.

136. Rich, A. (1962) In Kasha, M. and Pullman, B. (eds.), *Horizons in Biochemistry*. New York: Academic, pp. 103–126.

137. Woese, C.R. (1967) *The genetic code: the molecular basis for genetic expression*. Harper & Row, N.Y.

138. Addess, K.J., Sinsheimer, J.S. and Feigon, J. (1993) Solution structure of a complex between [N-MeCys3,N-MeCys7]TANDEM and [d(GATATC)]2. *Biochemistry*, **32**, 2498-2508.

139. Ferris, J.P., Sanchez, R.A. and Orgel, L.E. (1968) Studies in prebiotic synthesis .3. synthesis of pyrimidines from cyanoacetylene and cyanate. *Journal of Molecular Biology*, **33**, 693-695.

140. Joyce, G.F. (2002) The antiquity of RNA-based evolution. *Nature*, **418**, 214-221.

141. Bowman, J.C., Hud, N.V. and Williams, L.D. (2015) The ribosome challenge to the RNA world. *Journal of Molecular Evolution*.

VITA

CHIAMAKA DENISE OKAFOR

Denise Okafor (Enekwa) was born in Nashville, Tennessee. She attended schools in Nashville and in Lagos, Nigeria. She received a B.S. in Biomedical chemistry from Oral Roberts University, before coming to Georgia Tech to pursue a doctorate in Chemistry. In her spare time when she is not working on research, Denise enjoys spending time with her family, reading good fiction, and exploring new creative outlets.